# Analysis of the Vacuum Ultraviolet Spectra of $Br_2$, IBr and ICl

By

Derek Ian Austin

A thesis presented for the degree of

Doctor of Philosophy in the

Faculty of Science at the

University of Edinburgh, 1987

For mum and dad,

thanks for everything.

**Acknowledgements**

First and foremost I would like to thank my two supervisors, Professor Robert J. Donovan and Dr Kenneth P. Lawley, for their continued support and encouragement throughout the past three years. Without their advice and overall guidance, both in matters experimental and theoretical, much of the work presented in this thesis would not have been possible.

For the work with $Br_2$ involving the $F_2$ laser at the SERC Rutherford Appleton Laboratories I am indebted to: Dr Michael MacDonald, then of Edinburgh University, for his invaluable help; Professor Joel B. Tellinghuisen of Vanderbilt University, Tennessee for loaning the pure isotope $^{81,81}Br_2$ sample and donating some useful FORTRAN programmes used at various stages throughout this thesis; and the staff of the R.A.L.'s ultraviolet radiation facility, in particular Dr Malcolm Gower.

All the work performed at the SERC Daresbury Laboratory would not have been carried out without the efforts of the ever vigilant staff. Dr Andrew Hopkirk and Dr David Shaw were of notable resiliance, providing a first class user support service at all hours of the night and day. Miss Elinor Kerr of Edinburgh University performed the ICl work analysed in chapter 5, and Professor Andrew Yencha of the State University of New York was responsible for the IBr work analysed in chapter 4, helped latterly by Dr Paul Greenhill from the University of Edinburgh. In addition I would like to thank Miss Elinor Kerr and Professor Andrew Yencha for their company and patience during the long arduous shifts needed to make optimum use of the precious synchrotron resources.

Latterly, laser OODR experiments on ICl were performed at Edinburgh University. Involving Miss Elinor Kerr and Dr Trevor Ridley, both of Edinburgh University, this work gave access to very high quality data for which I am most grateful.

For financial support I am indebted to Edinburgh University for awarding a part-time demonstratorship for the first twelve months, and to the SERC for sponsorship as a Research Associate at the University of Edinburgh for the last two years.

I would like to take this opportunity to thank all members of the Physical

Chemistry Research Group at the University of Edinburgh, the Department of Chemistry, for a most enjoyable working ( and recreational ) enviroment which, on more than one occasion, made the inevitable difficult times easily tolerable.

Finally I must once again thank Dr Michael MacDonald for proof reading, and Mrs Rosie Filipiak for her typing services.

## Abstract

Vacuum ultraviolet absorption and fluorescence excitation spectra between 125 and 200 nm were obtained for $Br_2$, IBr and ICl. Abundant evidence of ion-pair/Rydberg interactions was manifest between resonant levels of the appropriate symmetry, whilst non-resonant ion-pair levels were seen to fluoresce strongly in the far and near ultraviolet. Analysis was confined almost exclusively to the latter.

An empirical law has emerged in recent years suggesting that the $\Delta\Omega=0$ selection rule dominates absorption from the ground state to the ion-pair manifold. All the molecules studied in this thesis were concordant with this observation. The upper states responsible for the reddest feature of this type observed in single photon VUV absorption from the ground state were identified as $D(0_u^+)$ in $Br_2$, $E(0^+)$ in ICl and $E(0^+)$ in IBr (Hund's case (c) notation). These states all belong to the first ion-pair cluster correlating with the $X^+(^3P_2)$ + $X^-(^1S_0)$ dissociation products.

Partially resolved ion-pair vibrational structure was observed with $Br_2$ and ICl. Close fitting of the more reliable $Br_2$ data needed a point of inflection in the D state potential at roughly $T_e(D)$ + 15000 $cm^{-1}$, presumably due to an avoided crossing with a Rydberg state of the appropriate symmetry. ICl required no such inflection, even though the $E(0^+)$ state almost certainly intersects a Rydberg state of the same symmetry, the $b_6'(\Pi_{0+})$, within the observed range. This indicates that the former molecule is best represented in the adiabatic approximation and the latter in the diabatic approximation.

Fluorescence was dispersed from all molecules excited across the ion-pair absorption, involving typically $v'>120$, where their wide vibrational amplitude gave extensive oscillatory continua emission. Several systems were observed for each species, however, the ion-pair → ground state transitions spanned the greatest internuclear separations and yielded most information. Recent studies have shown that if one state is well defined over the range of internuclear separations responsible for the emission, a unique fit can be acheived. This was exploited mostly to extend the ion-pair potentials and, with IBr, the ground state potential.

In addition, OODR work with ICl gave high resolution rovibrational term

values for the $E(0^+)$ state and also the $f(0^+)$ state, the next highest ion-pair state of $0^+$ symmetry, which arises from the second cluster correlating with the $^3P_0$ cation. For the E state the synchrotron vibrational levels were shown to belong to the same vibrational progression as these OODR rovibrational term values. With OODR, complete dispersed fluorescence spectra were also observed. The fitting of the blue bound-bound origin proved very sensitive to the position of the upper state inner wall, and is probably accurate to within 0.005 A.

Finally, single isotope studies involving $^{81,81}Br_2$ established without doubt the importance of isotope 'washing-in' in spectra of this type and futher confirmed the need for single isotope high resolution studies.

# TABLE OF CONTENTS

# CHAPTER 1
# INTRODUCTION

## 1.1 The Excited States of the Halogen Diatomics

The electronic states of the halogen diatomics may be broadly classified into four distinct groups: (i) Valence states; (ii) Ion-pair states; (iii) Rydberg states; (iv) Core excited states. Examples of types (i)-(iii) for $I_2$ are illustrated in figure 1.1 (see discussion in ref [1]). The accompanying figure 1.2 shows a simple linear combination of atomic orbitals (LCAO) representation of the homonuclear molecular orbitals; only the valence electrons are included. In this thesis electronic configurations of the type $\sigma_g^w\pi_u^x\ \pi_g^y\sigma_u^z$ : w+x+y+z = 10, will be abbreviated to (wxyz).

In the heteronuclear case, the atomic orbitals combined in the g/u MO pairs are no longer degenerate; this implies that the resultant molecular orbitals will be dominated by one or other of the original atomic orbitals i.e. $\sigma_g$ will become mainly $p_z^A$ in character and $\sigma_u$ mainly $p_z^B$, (the g/u symmetry label is no longer applicable). Heteronuclear electron configurations are abbreviated as before. But, it must always be borne in mind that some configuration mixing occurs in all states.

The valence states, type (i), are defined as electronic states that dissociate to neutral atoms, either in their ground $^2P_{3/2}$ or spin-orbit excited $^2P_{1/2}$ states. The best known examples are the $X(^1\Sigma_g^+)$: (2440) ground states; with long range potentials that may be expressed as the asymptotic series [2]:

$$V(R) = D_e - C5/R^5 - C6/R^6 - C8/R^8 \ ; \ R>2R_e \qquad (1.1)$$

(Typically, the ground state dissociation energy , $D_e$, lies between 12000 $cm^{-1}$ and 18000 $cm^{-1}$). The remaining valence states are either weakly bound ($D_e$ < 5000 $cm^{-1}$) e.g. $A(^3\Pi_{1u})$:(2431) and $B(^3\Pi_{0u}^+)$:(1441) , or repulsive (see tables 3.1, 4.1 and 5.1).

As the name suggests, the ion-pair states, type (ii), dissociate to the anion $X^-$:$ns^2np^6(^1S)$ and the cation $X^+$:$ns^2np^4(^3P,\ ^1D,\ ^1S)$ e.g. the $D(0_u^+)$ :(1441) state of $Br_2$ dissociating to the ion pair $Br^+(^3P_2)$ and $Br^-(^1S_0)$. As the ions approach from large R, the dominant force will be the long range Coulomb attraction $-e^2/4\pi\varepsilon_0R$, (c.f. equation 1.1 for the ground states). The resulting state is deeply bound with a very long range attractive branch giving the higher vibrational levels a very wide amplitude well below dissociation, see figure 1.1. Typically,in the diabatic aproximation , $D_e$ of the ion-pair states lies between

Figure 1.1 Some known states of $I_2$

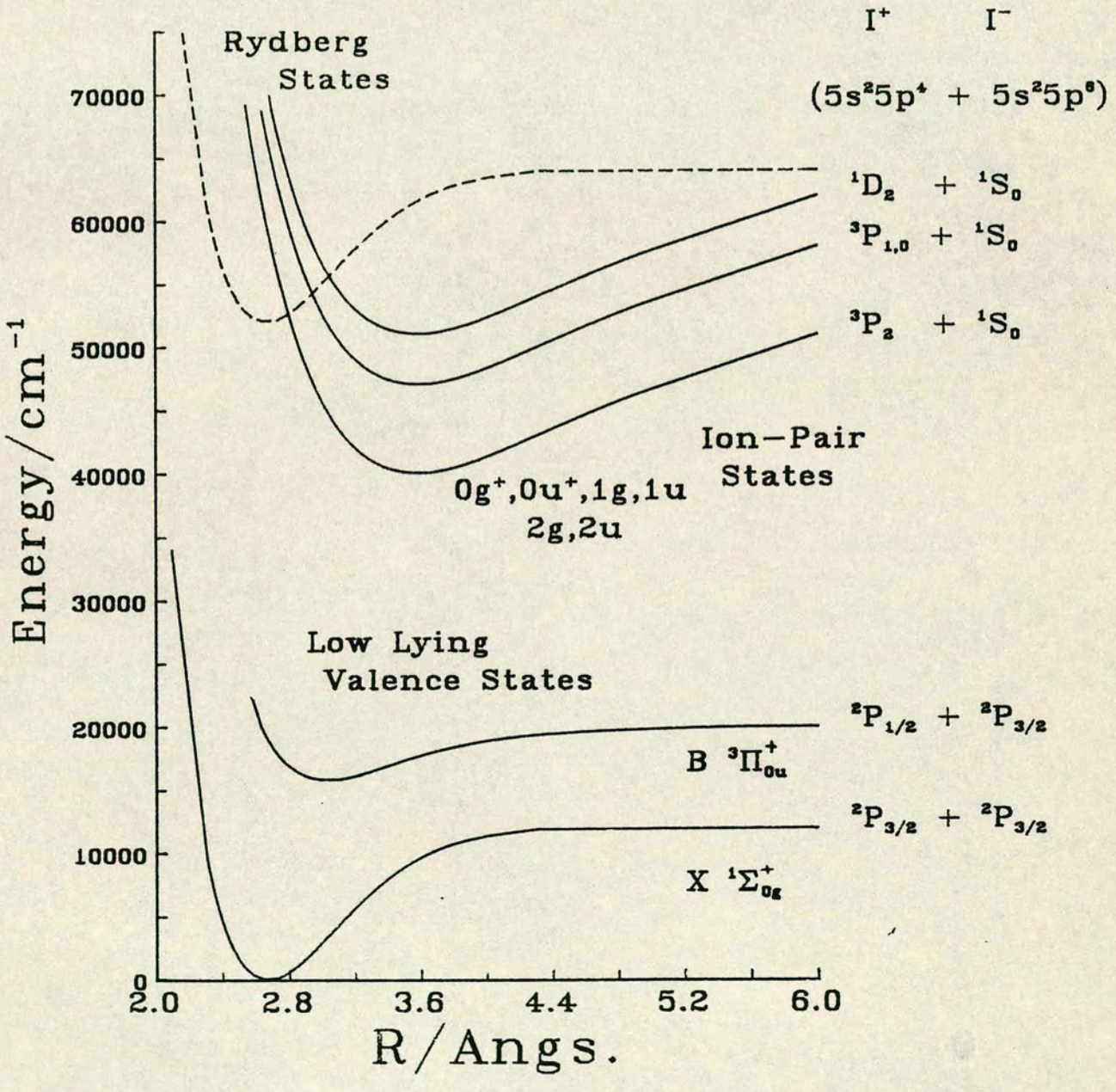

Figure 1.2

A simple LCAO representation of the halogen diatomics

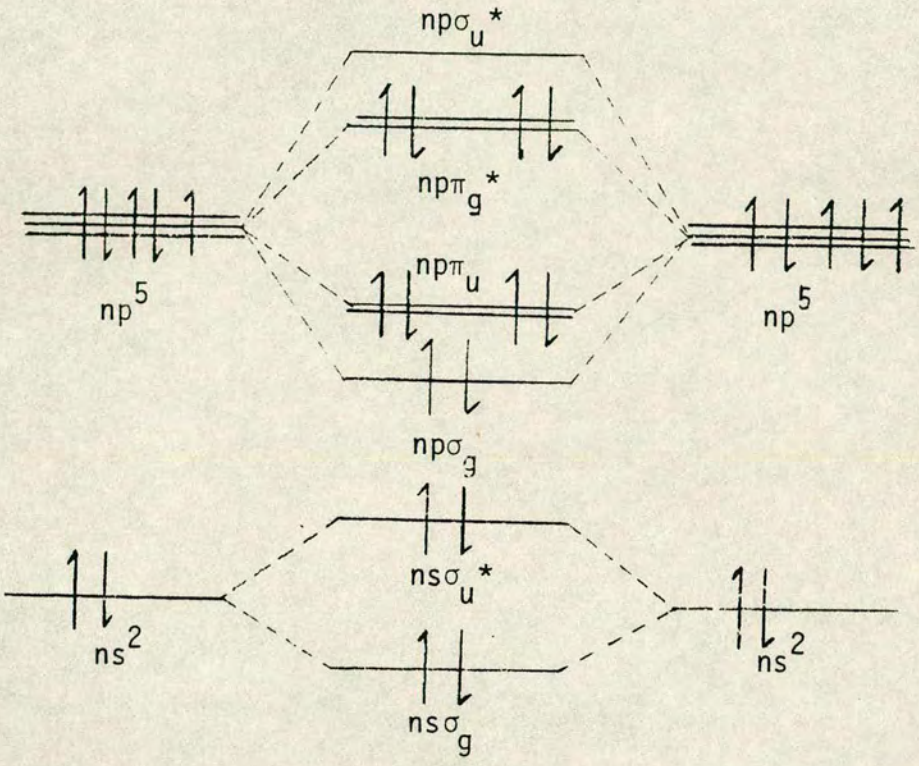


X = F : n = 2

X = Cl : n = 3

X = Br : n = 4

X = I : n = 5

30000 and 35000 $cm^{-1}$, whilst $R_e$ between 3.15 and 3.60 Å, see Tables 3.1, 4.1 and 5.1. Because of the relatively low ionisation potential and relatively high electron affinity of the halogens, the ion-pair states are of lower energies compared with the other lighter diatomics e.g. $H_2$, HCl etc. In general, the lowest halogen ion-pair states, dissociating to the $^3P$ cation, lie below the first Rydberg state. However, the unusually deep nature of the ion-pair potentials implies that their diabatic dissociation limits are normally higher than the diabatic dissociation limits of the lowest Rydberg states; this will inevitably lead to some avoided crossings at large internuclear separations (R>6 Å) between ion-pair and Rydberg states of the same symmetry.

The ion-pair states exhibit high reactivity [3-5]; they are known to react with noble gas atoms [6] and have been shown to be capable of breaking strong chemical bonds e.g. C-F. Because of their wide vibrational amplitude they are also the source of extensive oscillatory continuum emission [7-11]. The ease of interstate quenching within the ion-pair manifold allows a population inversion with respect to the valence states to be relatively easily established in v'=0 of the lowest ion-pair state , often the $D'(2_g)$. An excimer laser has been developed based on the subsequent $D'(2_g) \rightarrow A'(^3\Pi_{2u})$ strong transition in $F_2$ [12] (see section 3.2.2).

Rydberg states, type (iii), involve the promotion of a non-bonding or weakly antibonding/bonding electron to orbitals of higher principle quantum number eg. $Br_2$ $d_5[(2430):^2\Pi_{3/2g}]5p\sigma_u$, $\Pi_{1u}$. Rydberg states differing only in the principle quantum number of the promoted electron belong to the same series. If observed in absorption from v"=0 of the ground state, the (0,0) bands of any series can be represented by the following expression [13-15]:

$$\nu = E - R/(n-S)^2 \qquad (1.2)$$

where R is the Rydberg constant; S the screening constant characteristic of the series and n the principle quantum number of the promoted electron. As $n \rightarrow \infty$, $\nu \rightarrow E$, the molecular ionisation energy.

To a first approximation the molecular bond remains unchanged for any member of a Rydberg series and the potential curve is expected to be very similar to the ground state except lying at much higher energies. More accurately, the promotion of say an $np\pi^*$ electron usually produces a slightly tighter bond i.e. the dissociation energy is marginally increased, and $R_e$, the

equilibrium internuclear separation, is slightly reduced compared with the ground state. This is confirmed by the vacuum ultraviolet (VUV) absorption studies of Venkateswarlu ($Br_2$ [13], $I_2$ [14] and ICl [15]) in which all low lying Rydberg states have violet degraded vibrational resonances following absorption from the ground state.

Core excited states, type (iv), involve exciting an electron from very low lying molecular orbitals i.e. below the valence orbitals. The energies required to achieve this are considerable and do not concern the VUV experiments described in this thesis.

All the observations discussed in the following chapters involved absorptions probing these excited states between roughly 50000 and 80000 $cm^{-1}$. This window typically spanned regions involving pure ion-pair states, pure Rydberg states, ion-pair inner wall/Rydberg interactions and steeply rising repulsive states that may predissociate all the higher bound states. Extensive oscillatory emission was also abundant from levels within this excitation range. However, the previously mentioned Rydberg/ion-pair avoided crossings predicted at large R always lay outwith the spectral range excited and need not concern us further.

## 1.2 Potential Curves.

The eigenfunctions and energies of a molecule are found from the Schrödinger equation

$$\hat{H}.\Psi(R,\theta,\phi;r) = E.\Psi(R,\theta,\phi;r) \qquad (1.3)$$

$\hat{H}$ is the total Hamiltonian and E the total energy. The total wavefunction is a function of both the nuclear coordinates $(R,\theta,\phi)$ and the electronic coordinates (r). Fortunately the disparate masses of the electrons and nuclei implies that the electrons are moving much more rapidly than the nuclei, and to a good approximation we can regard the nuclei as fixed while the electrons execute their motions. This is known as the Born-Oppenheimer (BO) approximation. Their rigorous mathematical treatment showed that the true total molecular wavefunction is adequately described as

$$\Psi^{BO}(R,\theta,\phi;r) = \psi^{e}(R;r).\psi^{N}(R,\theta,\phi) \qquad (1.4)$$

when $(m_e/m_N)^{\frac{1}{4}} \ll 1$. $\psi^e$ is the electronic wavefunction and $\psi^N$ the nuclear

wavefunction. By substituting 1.4 into 1.3 and ignoring small terms involving $\partial\psi^e/\partial R$, $\partial\psi^N/\partial R$ and $\partial\psi^{e^2}/\partial R^2$, it is easily shown that [16]:

$$[\hat{T}^N(R,\theta,\phi) + V(R)].\psi^N(R,\theta,\phi) = E.\psi^N(R,\theta,\phi) \qquad (1.5)$$

where

$$V(R) = \langle \psi^e(R;r) \,|\, \hat{H}^e + V^{NN} \,|\, \psi^e(R;r) \rangle \qquad (1.6)$$

equation 1.5 is the nuclear Schrödinger equation. $\hat{T}^N$ is the nuclear kinetic energy operator which by separation of variables can be divided into vibrational and rotational terms (see equation 1.12). Equation 1.6 defines the potential energy curve in which the nuclei move. $\hat{H}^e$ is the electronic Hamiltonian (including kinetic and potential terms) and $V^{NN}$ is the nuclear repulsive term. The electronic wavefunctions and energies thus depend parametrically on the nuclear configuration. It must be emphasised that the potential energy curves as defined by equation 1.6, do not correspond to any physical observables, they are a concept defined by a particular type of approximate wave functions (equation 1.4). Furthermore, the potential energy curves are those that would be followed only if the two atoms were brought together infinitesimally slowly. The problem of defining a single potential energy curve for an electronic state is not usually encountered in ground state potentials, except perhaps at very long ranges if two or more molecular states of the same symmetry become degenerate at infinity. It is however, frequently encountered among the higher electronic states.

## 1.3 The Adiabatic and Diabatic Approximations

Homogeneous perturbations between two states of the same symmetry are commonplace in the halogen diatomics [17-19]. Two types of off-diagonal matrix elements determine how these states will interact [20]:

$$\langle \psi_1^e \,|\, \hat{H}^e \,|\, \psi_2^e \rangle_r \qquad (1.7)$$

and

$$\langle \psi_1^e \,|\, \hat{T}^N \,|\, \psi_2^e \rangle_r \qquad (1.8)$$

It is not possible to find solutions of the electronic Hamiltonian for which both 1.7 and 1.8 are simultaneously zero. However two limits, the adiabatic and diabatic approximations, may be defined.

Figure 1.3

The diabatic curves (solid) cross at $R_c$. The adiabatic curves (dotted) avoid crossing by $2H^e_{12}$ at $R_c$.

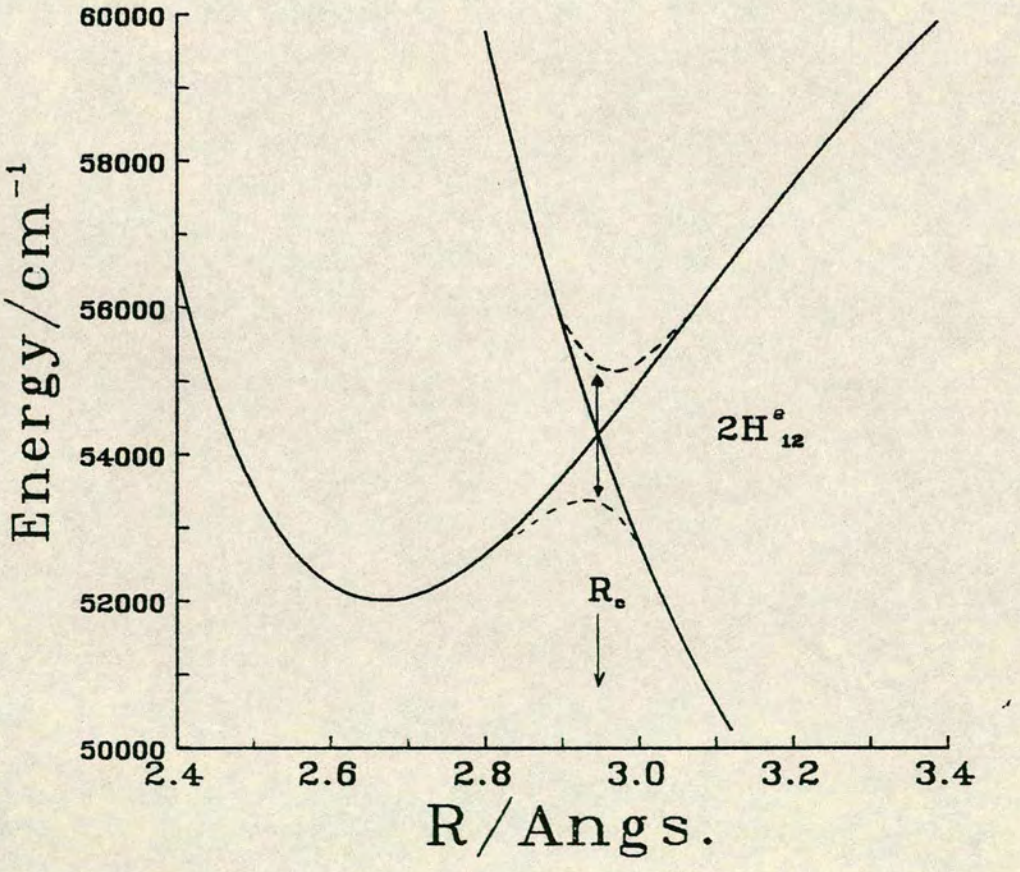

The diabatic potentials arise from electronic wave functions $\psi^e_d$, for which expressions 1.8 is zero and expression 1.7 is necessarily non-zero. These potentials consequently cross (see figure 1.3). Alternatively, the adiabatic potentials arise from electronic wavefunctions $\psi^e_{ad}$, for which expression 1.7 is zero i.e. they are exact solutions of the electronic Hamiltonian, and expression 1.8 is necessarily non-zero. These potentials consequently obey the non-crossing rule [21] (figure 1.3).

For the case of two interacting electronic states, the adiabatic potentials may be expressed in terms of the diabatic potentials [22].

$$V^{ad}_{\pm}(R) = \tfrac{1}{2}[V^d_1(R) + V^d_2(R)] \pm \tfrac{1}{2}\{[V^d_1(R) - V^d_2(R)]^2 + 4(H^e_{12})^2\}^{\frac{1}{2}} \quad (1.9)$$

where

$$H^e_{12} = \langle \psi^e_{d,1} \,|\, \hat{H}^e \,|\, \psi^e_{d,2} \rangle_r \quad (1.10)$$

Equation 1.10 represents the electronic interaction integral calculated for the diabatic wavefunctions. Neither limit, the adiabatic nor diabatic, will exactly reproduce the observed vibrational levels. To do this, the matrix of the complete Hamiltonian (equation 1.3), including $\hat{H}_{so}$ and $\hat{T}^N$, must be set up in the diabatic or adiabatic vibronic basis and the resultant matrix diagonalised. For further reading see reference [20].

There is abundant evidence of interacting electronic states in the VUV absorption and fluorescence excitation spectra of the halogens and interhalides (figures 3-5.1). Strong coupling exists between most of the Rydberg states and near-resonant ion-pair vibrational levels of appropriate symmetry. The non-resonant ion-pair levels fluoresce strongly, and it is with these relatively unperturbed regions of the spectra that we will be concerned in this thesis.

## 1.4 The Franck-Condon Principle

The nuclear Schrödinger equation, equation 1.5, can be divide into vibrational and rotational terms by the separation of variables [23]:

$$\psi^N_n(R,\theta,\phi) = \psi^{vJ}_n(R).\psi^J_n(\theta,\phi) \quad (1.11)$$

$\psi^J_n$ are the eigenfunctions of the angular contributions to the total nuclear

Hamiltonian and $\psi_n^{vJ}$ are the solutions to the radial nuclear Schrödinger equation:

$$[\hat{T}^N(R) + \hbar^2/2\mu R^2.(J(J+1)) + V(R)].\psi_n^{vJ} = E_n.\psi_n^{vJ} \qquad (1.12)$$

J is the rotational quantum number of a particular rotational state of the vibrational level with quantum number v.

The line strength, S, of an electronic transition from v';J' in state 1 to v";J" in state 2 is governed by [24,25]:

$$S_{2v"J"|1v'J'} = |\langle \psi_2^{v"J"}(R) | \mu_{21}(R) | \psi_1^{v'J'}(R) \rangle_R|^2 = M_{21}^2 \qquad (1.13)$$

when $\mu_{21}(R)$ is the transition dipole moment operator.

As mentioned in section 1.1, rich fluorescence structure is often observed following excitation of the halogen ion-pair states. These fluorescence systems all exhibit complex oscillatory continuum emission [7-11] in which the intensity dependence on fluorescence frequency, $h\nu_f=E_{1v'}-E_{2v"}+T_e$, is governed by $M_{21}^2$. In such transitions, $\psi_2^{v"J"}$often corresponds to continuum wave functions of the lower state, in this case the label $\psi_2^{E"}$ is more appropriate. Although numerical solution of equation 1.12 and numerical evaluation of expression 1.13 are now commonplace [26-28], what information regarding the states involved can practically be derived by inspection of the general features of such spectra. By substituting the primitive WKB approximation [29]:

$$\begin{aligned}\psi_n^{vJ} \simeq \psi_{WKB} &= (k_n^{vJ}(R))^{-\frac{1}{2}}.\cos\{\textstyle\int_{R_n^o}^{R} k_n^{vJ}(R')dR' + \pi/4\} \\ &= k_n(R)^{-\frac{1}{2}}.\cos(\phi_n)\end{aligned} \qquad (1.14)$$

into equation 1.13 we get:

$$\begin{aligned}M_{21} &= \textstyle\int_{-\infty}^{\infty}(k_2k_1)^{-\frac{1}{2}}.\mu_{21}(R).\cos\phi_1.\cos\phi_2\ dR \\ &= \tfrac{1}{2}\textstyle\int_{-\infty}^{\infty}(k_2k_1)^{-\frac{1}{2}}.\mu_{21}(R).(\cos\phi_+ + \cos\phi_-)dR\end{aligned} \qquad (1.15)$$

where

$$k_n(R) = (2\mu/\hbar^2.(E_n-V_n(R)))^{\frac{1}{2}}$$

$$\phi_\pm = \phi_2 \pm \phi_1$$

and $R_n^0$ are the classical inner turning points of each vibronic wavefunction (see also discussion in ref [25]).

At this junction the stationary phase method is introduced: The integral of

the product of two sinusoidal functions can only accumulate appreciably in regions where the two functions have the same periodicity. Equivalently:

$$\partial\phi_{\pm}/\partial R = k_2 \pm k_1 = 0 \qquad (1.16)$$

$\phi_+$ has no meaningful solution. However ,

$$\partial\phi_-/\partial R = 0$$
$$\Rightarrow \quad k_2 = k_1 \qquad (1.17)$$

i.e. the local wavelength of the upper and lower state configurations, and hence the nuclear momentum ($p=\hbar k$) is conserved during a vibronic transition. This is precisely the Franck-Condon Principle:

> " The nuclear conformation readjusts after the electronic transition, and not during it."

This establishes a one-to-one correspondence between all points in the common upper vibronic level and a locus of points within the lower state following a vertical fluorescent transition. This locus of points is known as the Mulliken difference potential [30,31]:

$$W(R) = E_1 - V_1(R) + V_2(R) \qquad (1.18)$$

Examples of Mulliken difference potentials are shown in figure 1.4.

Abandoning the $\phi_+$ contribution to equation 1.15 and making a linear approximation to $V_{12}(R)=V_1(R)-V_2(R)$ the difference potential, (n.b. this is not quite the same as the Mulliken difference potential in equation 1.18), it can be shown that [24,25]:

$$M_{21} = \mu_{21}(R^*).[k(R^*)V_{12}'(R^*)]^{-\frac{1}{2}}.\cos(\eta_{21}(R^*)+\pi/4) \qquad (1.19)$$

where $R^*$ is the coordinate where the local wavelengths of upper and lower states are equal; $k(R^*)$ is the conserved wavenumber common to both wavefunctions;

$$\eta_{21} = \int_{R_2^\circ}^{R^*} k_2(R)dR - \int_{R_1^\circ}^{R^*} k_1(R)dR \qquad (1.20)$$

and

$$V_{12}' = d(V_1(R)-V_2(R))/dR\,|_{R^*}$$
$$= dV_1/dR\,|_{R^*} - dV_2/dR\,|_{R^*}$$
$$= -W'(R^*) \qquad (1.21)$$

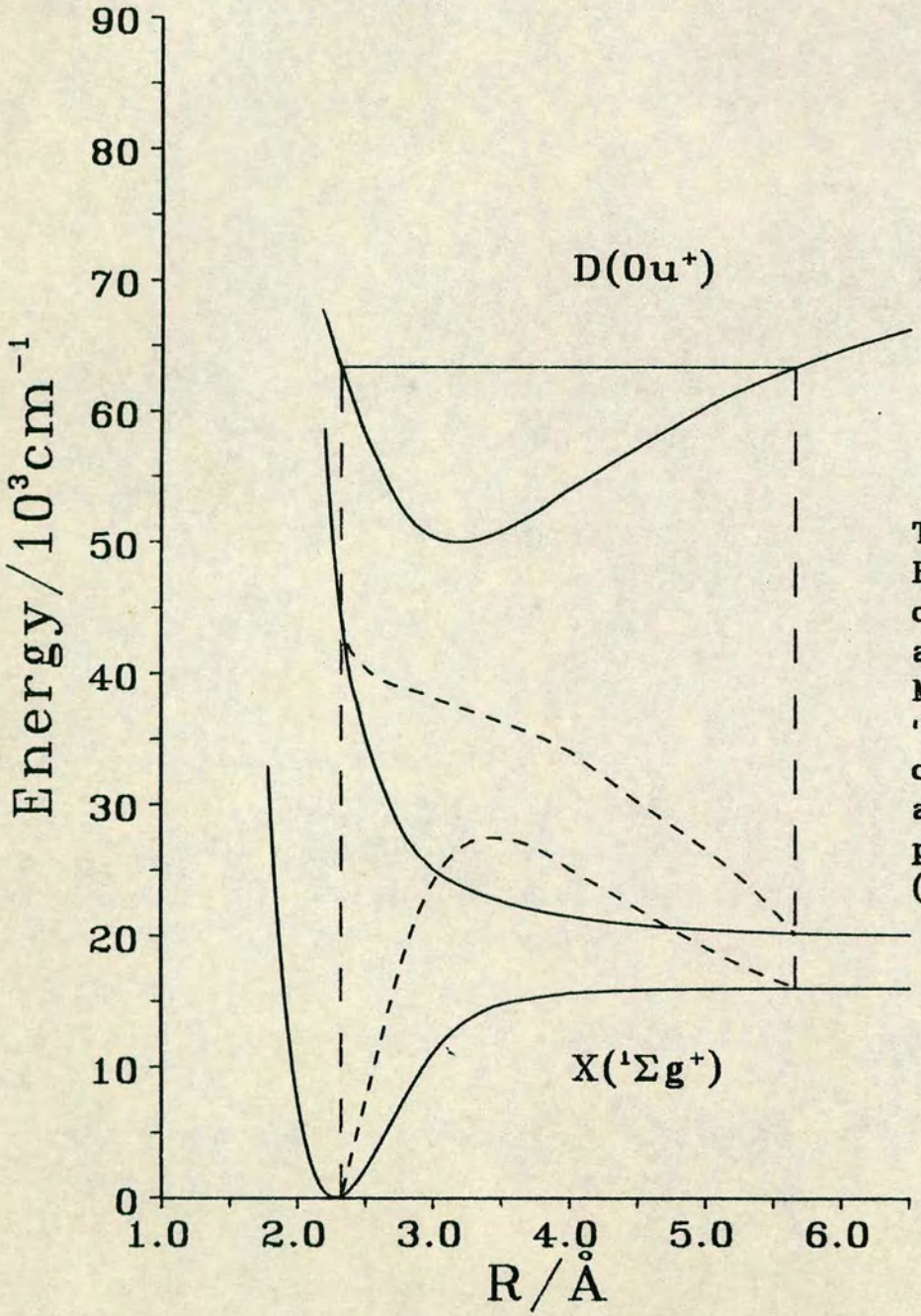


Figure 1.4

Three known potentials of $Br_2$. 'Single' frequency oscillatory continua are associated with a monotonic Mulliken difference potential. 'Double' frequency oscillatory continua are associated with a Mulliken difference potential with a maximum. (See figures 3.13 & 3.10)

If $\mu_{21}(R)$ is assumed to be a slowly varying function of R, it may be considered constant over the small range of R ($=R^{*}\pm dR$) over which the integral 1.15 accumulates. The approximation of performing the integral, then multiplying by $\mu_{21}(R^{*})$ is known as the r-centroid approximation.

Equation 1.19 is adequate for discussions involving a monotonic Mulliken difference potential (see figure 1.4), all the contributing terms to $M_{21}$ having been accounted for. The resulting spectra will have a peak at the red wavelength origin corresponding to transitions from the inner turning point of the upper state to inner turning points of the highest continuum vibronic levels of the lower state. On moving to the blue, or equivalently, along the Mulliken difference potential to larger R, $\eta_{21}$ (equation 1.20) will gradually change and the cosine term in equation 1.19 will modulate the intensity ($I(\nu_f)\alpha M_{21}^{2}$) producing maxima and minima in the spectra corresponding to regions of equal local wavelengths in upper and lower states coming in and out of phase. These oscillations will in turn be modified by the $M_{21}^{2}$ being inversely proportional to the gradient of the difference potential, $V_{12}'(R^{*})$ (equation 1.21), and also inversely dependant on the conserved nuclear momentum, $\hbar k(R^{*})$. On theoretical grounds, $\mu_{21}(R^{*})$ is expected to monotonically decay to large R , this will attenuate the spectra to the blue. The spectrum corresponding to the monotonic Mulliken difference potential shown in fig 1.4 exhibits all the features discussed so far and may be found in figure 3.13. Included is a simulation based on the numerical solution of equation 1.12 and numerical evaluation of the integral within equation 1.13. In this thesis, these types of spectra will be known as 'single' frequency oscillatory continua, elsewhere they are sometimes referred to as exhibiting reflection structure [32], but this name is not satisfactory because it is, in fact, interference structure.

There is a second type of transition shown in figure 1.4. Here the Mulliken difference potential has a maximum i.e. there exists two $R^{*}$ in the continuum region of the lower state. In this instance two contributions must be combined prior to squaring $M_{21}$:

$$M_{21} = A^{(i)}\cos(\eta_{21}(R^{*}_{(i)})+\pi/4) + A^{(ii)}\cos(\eta_{21}(R^{*}_{(ii)})+\pi/4) \qquad (1.22)$$

These two terms, depending on the relative signs, may reinforce or cancel each other. The resulting line strength, $S_{21} = M_{21}^{2}$, will be modulated by a low frequency phase difference:

$$\Delta\eta_{21} = \int_{R_i^*}^{R_{ii}^*} [k_2(R) - k_1(R)]\, dR \qquad (1.23)$$

The spectrum corresponding to the 'polytonic' Mulliken difference potential shown in figure 1.4 may be found in figure 3.10. Again a simulation is included based on the numerical solution of equation 1.12 and numerical evaluation of the integral within equation 1.13. The low frequency modulating envelope produces supernumerary maxima quite distinct from the higher frequency structure. In this thesis, I will refer to these as 'double frequency' oscillatory continua; elsewhere they are sometimes known as interference structure [32].

The existence of a maximum in the Mulliken, or minima in the normal, difference potential causes a discontinuity in expression 1.19 for $M_{21}$ (since $V_{12}'=0$). This is because $V_{12}(R)$ was replaced by a linear approximation in the region of stationary phase. If a quadratic approximation were made, the Airy function envelope would emerge but still within the semi-classical approximation. The spectral region corresponding to $V_{12}'=0$ is referred to as the red extremum, or alternatively the rainbow in analogy with scattering theory when this type of classical catastrophe is common. Whereas in classical molecular collision theory a 'rainbow' angle corresponds to a point at which the density of classical trajectories rises to infinity [33], in 'double' frequency oscillatory continua the rainbow wavelength corresponds to a point where the density of fluorescent bond lengths rises to infinity. Much further to the blue the bound-bound/bound-free boundary is encountered, and beyond this is a single frequency modulation of the characteristic line spectrum of a bound-bound transition, see e.g. figure 5.7.

## References.


1. R.S. Mulliken, J. Chem. Phys., 55, 288, (1971).
2. T.Y. Chang, Rev. Mod. Phys., 39, 911, (1967).
3. L.C. Glasgow and J.E. Willard, J. Phys. Chem., 77, 1585, (1973).
4. R.J. Donovan, B.V. O'Grady, L. Lain and C. Fotakis, J. Chem. Phys., 78, 3727, (1983).
5. Z. Yun-wu, W. Fuss and K.L. Kompa, J. Photochem., 23, 311, (1983).
6. J.P.T. Wilkinson, M. MacDonald and R.J. Donovan, Chem. Phys. Lttrs., 101, 284, (1983).
7. J. Tellinghuisen, Chem. Phys. Lttrs., 29, 359, (1974).
8. M. MacDonald, J.P.T. Wilkinson, C. Fotakis, M. Martin and R.J. Donovan, Chem.Phys. Lttrs., 99, 250, (1983).
9. M. MacDonald, R.J. Donovan and M.C. Gower, Chem. Phys. Lttrs., 97, 72, (1983).
10. K.P. Lawley, M. MacDonald, R.J. Donovan and A. Kvaran, Chem. Phys. Lttrs., 92, 322 (1982).
11. M. Martin, C. Fotakis, R.J. Donovan and M.J. Shaw, Nuovo Cimento Soc. Ital. Phys. B, 63, 300, (1981).
12. H. Pummer, K. Hohla, M. Diegalmann and J.P. Reilly, Opt. Commun., 28, 104, (1974).
13. P. Venkateswarlu, Can. J. Phys., 47, 2525, (1969).
14. P. Venkateswarlu, Can. J. Phys., 48, 1055, (1970).
15. P. Venkateswarlu, Can. J. Phys., 53, 812, (1973).
16. J.N. Murrell, J.M. Tedder and S.F.A. Kettle, 'Valence Theory', 2nd Edition, Wiley, pp84-85, (1978).
17. A.R. Hoy and J.C.D. Brand, Chem. Phys., 109, 109, (1986).
18. A.R. Hoy, S.M. Jaywant and J.C.D. Brand, Mol. Phys., 60, 749, (1987).
19. D.I. Austin, R.J. Donovan, A. Hopkirk, K.P. Lawley, D. shaw and A.J. Yencha, Chem. Phys., accepted for publication (1987).
20. H. Lefebvre-Brion and R.W. Field, "Perturbations in the Spectra of Diatomic Molecules", Academic Press, pp70-86 (1986).
21. J. Von Neumann and E. Wigner, Physik Z., 30, 467, (1929).
22. M.S. Child and R.B. Bernstein, J. Chem. Phys., 59, 5916, (1973).
23. L. Pauling and E.B. Wilson, "Introduction to Quantum Mechanics", McGraw-Hill (1935).
24. K.P. Lawley, private communication.
25. J.B. Tellinghuisen, Adv. in Chem. Phys., XV, 299 (1985)
26. J.W. Cooley, Math. Comp., 15, 363, (1961).
27. J. Tellinghuisen, J. Quant. Spectrosc. Radiat. Transfer, 19, 149, (1978).
28. K.P. Lawley and R. Wheeler, J. Chem. Soc. Faraday Trans., 2, 77, 1133, (1981).
29. E.C. Kemble, 'The fundamental principles of Quantum Mechanics with elementary Applications', pp 90-93.
30. K. Tamagake and D.W. Setser, J. Chem. Phys., 67, 4370, (1977).
31. R.S. Mulliken, J. Chem. Phys., 55, 309, (1971).
32. J.B. Tellinghuisen, J. Mol. Spectrosc., 103, 455, (1984).
33. M.S. Child, 'Molecular Collision Theory', Academic Press, London, p19, (1973).

# CHAPTER 2
# SIMULATION TECHNIQUES

## 2.1 Numerical Solution of the Radial Schrödinger Equation.

The radial Schrödinger equation can be expressed in reduced units as (c.f. equation 1.12):

$$\{-d/d\rho^2 + J(J+1)/\rho^2 + V^*(\rho)\}.\psi = E^*.\psi \qquad (2.1)$$

where

$$\rho = R/\sigma$$
$$E^* = 2\mu\sigma^2E/\hbar^2$$
$$V^*(\rho) = 2\mu\sigma^2V(R)/\hbar^2$$

and $\sigma$ is any convenient length parameter. This in turn may be written as

$$d^2\psi/d\rho^2 = F(\rho).\psi \qquad (2.2)$$

where

$$F(\rho) = ( V^*(\rho) + J(J+1)/\rho^2 - E^* )$$

The best approach for solving second order differential equations like equation 2.2, i.e. $y'' = f(x,y)$, is undoubtedly Numerov's method [1,2]:

$$\psi_{n+1} - 2\psi_n + \psi_{n-1}$$
$$= 1/12h^2.\{ F_{n-1}\psi_{n-1} + 10F_n\psi_n + F_{n+1}\psi_{n+1} \} \qquad (2.3)$$

where h is the step length with which the $F_n$ are defined.

Equation 2.3 was first applied to the Radial Schrödinger equation by Cooley in 1961 [3] (see also Zare [4] and Cashion [5]). If $\sigma$ is chosen as the grid spacing over which V(R) is tabulated, then h, as defined by equation 2.3, will equal unity, and on rearranging equation 2.3:

$$\psi_{n+1} = ( 2\psi_n - \psi_{n-1} + 1/12( F_{n-1}\psi_{n-1} + 10F_n\psi_n )$$
$$/( 1 - F_{n+1}/12)) \quad \text{to } O(h^6) \qquad (2.4)$$

A suitable choice of $\psi_0$ and $\psi_1$ then allows, by outward integration, the wavefunction to be calculated as a one dimensional array containing values at the grid points of the potential.

Lawley and Wheeler [6] suggested that the most efficient way of calculating large numbers of sequential eigenvalues and eigenvectors lying between specified limits is through the replacement of the second order differential

operator of equation 2.1, by the second central difference, followed by a matrix formulation of the eigenvalue problem. This method is still preferred when calculating bound eigenvalues and eigenvectors within the potential well. However, in continuum regions, above the dissociation energy, it requires an infinite potential barrier at very large R to create a quasi-continuum with a high density of states such that slit convolution renders a 'smooth' simulation of bound-free fluorescence structure. This is costly in computing time. The Cooley-Numerov method is far more efficient by comparison. The continuum states need only be sampled at energies corresponding to the monochromator steps, and outward integration is only continued until the upper state wavefunction is exhausted and an accurate value of the asymptotic amplitude available.

The bound wavefunctions were normalised as usual and the continuum wavefunctions to unit asymptotic amplitude. Rather than repeat the integration of equation 2.4 until a stable asymptotic amplitude is attained, the second order correction to the amplitude of the primitive WKB wavefunction was monitored . When this fell below the 1% level (equation 2.5) the WKB solution was regarded as adequate and the asymptotic amplitude calculated by equation 2.6.

$$V_n^{*\prime\prime} + 5/4.(V_n^{*\prime})^2/(E^* - V_n^*) < (E^* - V_n^*)^2 \times 0.1 \qquad (2.5)$$

$$A_\infty = A_n.((E^*-V_n^*)/(E^*-V_\infty^*))^{1/4} \qquad (2.6)$$

It was found that the primitive WKB wavefunctions became good surprisingly quickly, in some cases at bond lengths on the attractive limb corresponding to only 30% of dissociation. However, one could easily be deceived at energies in the continuum just above dissociation. In rotationally excited molecules, the centrifugal barrier may distort the continuum wavefunction such that $A_\infty$, calculated by equations 2.5 and 2.6, could be inaccurate. Implementation of safeguards against such errors are planned e.g. monitoring the magnitude of the centrifugal barrier. Despite this, for purely repulsive, monotonic potentials, or large amplitude upper states, all should still be well.

Equations 2.4 and 2.6 can be easily identified in the IMP subroutine listed in Appendix A. The accuracy of the Numerov method was checked by solving $y''=yx$ and comparing with tables of the Airy function [7].

## 2.2 Reduced Potential Curves.

The potential curve of a diatomic, V(R), as defined by equation 1.6, is a function of three parameters; $Z_1$ and $Z_2$ , the atomic number of the two nuclei and n, the number of electrons. Thus, the structure of the Hamiltonians of different diatomics, where the Born Oppenheimer approximation is valid, are analogous, and one could conjecture the existence of a Universal Potential function containing the three parameters $Z_1$, $Z_2$ , and n. Since all other molecular constants may be deduced from the potential function, a universal function may alternatively be parameterised by (at least three) molecular constants. This is the foundation of the so far elusive, 'empirical' potential function for diatomic molecules [8]. Another approach is to replace the normal quantities , V and R, by 'reduced' variables $V^*$ and $\rho$ whose definition is based on molecular constants De, $R_e$, $\omega_e$ etc. This may lead to a common 'reduced' potential for all diatomics. However, the underlying assumption, that the structure of the vibrational problem remains unaltered for different diatomics, is not strictly correct; it (the vibrational problem) is dependent on atomic number. More importantly, irregularities may be expected in highly excited states where non-adiabatic perturbations appear. In the ground states such perturbations are rare, and as they are generally well known they are ideal to test various reduction schemes.

For the halogen/halide ground states several methods were investigated; (i) Jenč's Reduced Curve Method [9,10], which was initially developed for analysis of the alkali diatomics repulsive inner walls. Applied to the halogen/halide diatomics the reduced curves gave excellent agreement on the repulsive wall but appeared 'skewed' on the attractive limb, the discrepancies starting very low within the well; (ii) A simple scheme with $V^*=V/De$ and $\rho=R/R_e$. This gave slightly closer agreement with the attractive limb than (i), but much poorer alignment of the inner walls and consequently was of little practical use. (iii) The most successful scheme was the Harmonic Oscillator Reduced Curve (HORC) based on the following reductions:

$$V^* = V/De \tag{2.7}$$

and

$$\rho = (\mu\omega_e^2/De)^{\frac{1}{2}}.(R - R_e) \tag{2.8}$$

(This is identical to the reduction scheme suggested by the Morse potential).

Using the molecular constants available for the ground states of $Br_2$ [11], $I_2$ [12,13] and $Cl_2$ [14], the reduced potentials plotted in fig. 2.1 were derived. Good coincidence is maintained up to 80% of dissociation.

As an additional test of the technique, the reduced ground state of IBr was estimated by a simple midway interpolation between the contributory halogen reduced potentials.

$$V^*_{IBr} = (V^*_{I_2} + V^*_{Br_2})/2 \qquad (2.9)$$

The resulting potential was then 'unreduced' using the molecular constants in reference [15] and a comparison made with the limited RKR analysis, also presented in reference [15]. The RKR turning points extend to 30% of dissociation and at this energy the unreduced curve agreed to within 40 $cm^{-1}$, the entire curve being skewed slightly anticlockwise. In chapter 4 where the ion-pair → ground state dispersed fluorescence of IBr is analysed, this potential gave a very useful 'first' guess of the ground state beyond the range of the available RKR turning points.

## 2.3 The Ion-Pair - Ground State Rovibronic Contour

In this thesis access to the ion-pair manifold was often via a single photon process from low lying (v"=0 and 1) vibrational levels of the ground state; $\Delta\Omega=0$ transitions appear to dominate (see chapters 3-5). If the Boltzmann population distribution is assumed for the ground state, what does the rovibronic contour of these transitions look like?

Normally when $R_e' > R_e''$, and this is universally the case for ion-pair ← X transitions, the R branch ($\Delta J = +1$) of a $^1\Sigma^+ \leftarrow {}^1\Sigma^+$ transition will reverse to form a band head to the blue of the band origin. Each individual line, of both P and R branches, will have an intensity reflecting the population of the original J" level in the ground state. The energies of the R branch contributions are

$$E_R = G_{v'} - G_{v''} + B_e'(J''+1)(J''+2) - (v'+1/2)\alpha'(J''+1)(J''+2) - B_{v''}(J''(J''+1)) \qquad (2.10)$$

For simplicity we have ignored the centrifugal distortion coefficients of both states. Since only low vibrational levels of the ground state are included we can also safely discard $\alpha''$, the vibration-rotation interaction constant . $G_{v'}-G_{v''}$ is the energy of the band origin.

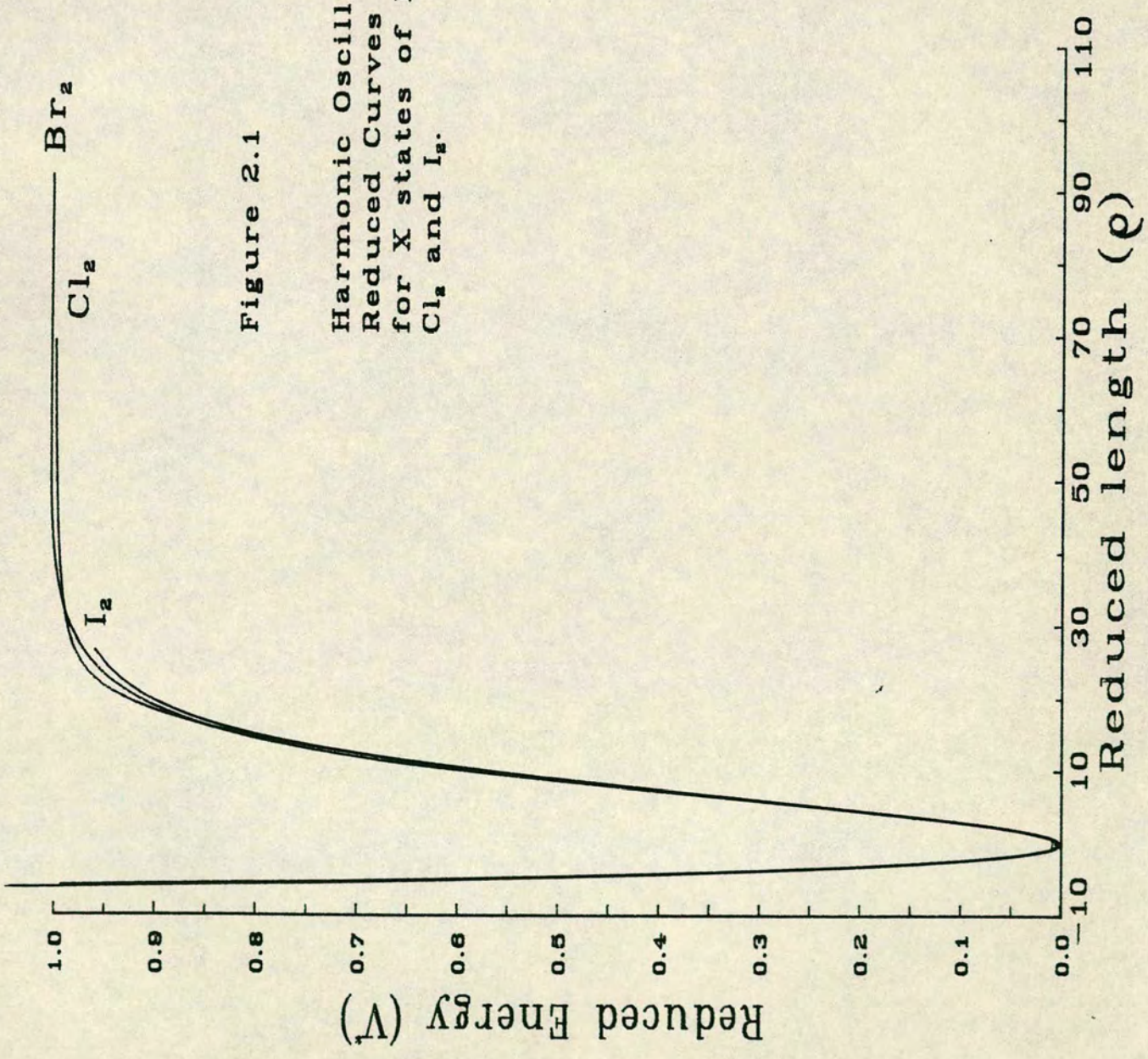


Figure 2.1

Harmonic Oscillator
Reduced Curves (HORC)
for X states of $Br_2$,
$Cl_2$ and $I_2$.

The point at which the R branch reverses may be defined as:

$$dE_R/dJ'' = 0 \qquad (2.11)$$

or alternatively when

$$J''_* = (3v'\alpha' - 3B_{e'} + B_{v''})/(2B_{e'} - 2B_{v''} - 2v'\alpha') \qquad (2.12)$$

Typical values for a halogen ion-pair ← ground state single photon absorption are; $v' \simeq 100$; $B_{v'} \simeq 0.04$ cm$^{-1}$, $B_{v''} \simeq 0.08$ cm$^{-1}$ and $\alpha' \simeq 1 \times 10^{-4}$ cm$^{-1}$. Substituting these values into equation 2.12 gives $J''_* = 0.1$ i.e. the band reverses immediately.

Instead of the maximum of the rovibronic contour lying at a band head, as is more normal, because of the large difference in $B_{v'}$ and $B_{v''}$ the maximum in the rovibronic contour is now to the red of the band origin and dependent on resolution. Figure 2.2 shows the rovibronic contour of an isolated vibronic transition in $Br_2$ :$D(0_u^+)$ ← $X(0_g^+)$ for $v' \simeq 140$ and $v''=0$. The actual maximum is found at an energy equivalent to $J''=16$, compared with $J_{max}=36$ (equation 2.13) the most populated level.

$$J_{max} = 2((kT/2hB_{v'}) - 1)^{\frac{1}{2}} \qquad (2.13)$$

As a rough guide we found that in ion-pair ← ground state absorption, at resolutions typical of the work presented in this thesis, the rotational level corresponding to the maximum of the rovibronic absorption contour is $J''=J_{max}/2$ n.b. the most populated rotational levels in the upper state will still be the P and R branches associated with $J''_{max}$, they will not however correspond to the maximum of the profile in figure 2.2.

Fortunately most of the analysis in this thesis has proved to be rather insensitive to initial rotational populations and this rough guide is thought to be sufficient to estimate rotational contributions (see sections 3-5.4).

## 2.4 Dispersed Fluorescence Simulation Procedure

The following notation will be used. The envelope of a structured continuum will have their peaks numbered from 0 at the longest wavelength. In the case of a maximum in the Mulliken difference potential, W(R), $I_0$ will refer to the rainbow peak and $I_1$ to the first supernumerary peak and so on. If W(R) is a monotonic function, only the high frequency structure will remain and $I_0$

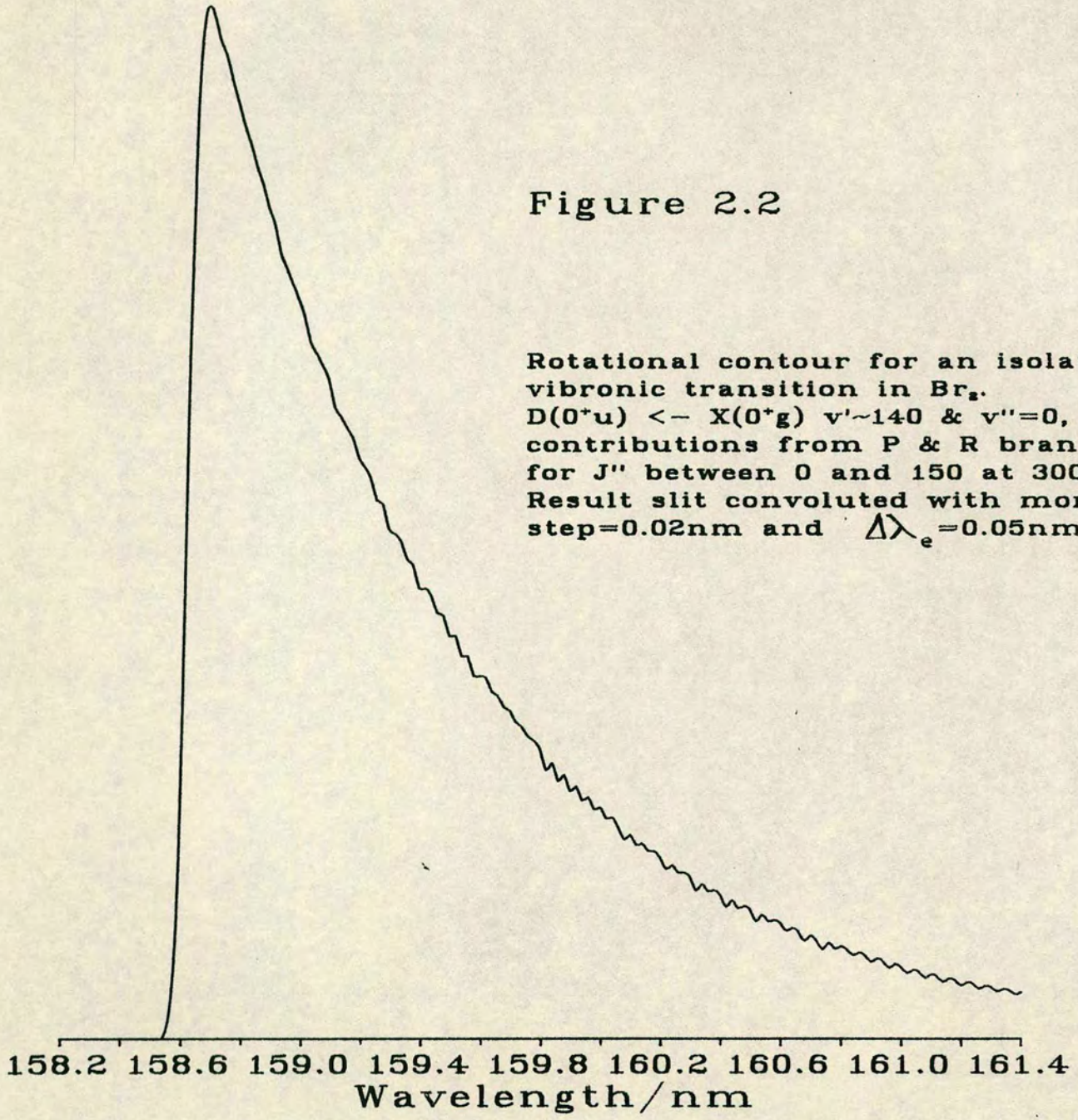


Figure 2.2

**Rotational contour for an isolated vibronic transition in $Br_2$. $D(0^+u) \leftarrow X(0^+g)$ $v' \sim 140$ & $v''=0$, includes contributions from P & R branches for J'' between 0 and 150 at 300K. Result slit convoluted with monochromator step=0.02nm and $\Delta\lambda_e$=0.05nm**

will come from a classical point of transition close to the inner turning point of the upper state vibrational motion. The classical point of transition for a given fluorescent frequency, $\omega$, will be denoted by $R^*(\omega)$ and the energy of the unbound motion in the lower state by $E(\omega) = \hbar(\omega_i - \omega_f) + T_{00}''$. The classical turning point on the lower surface at this energy is $R^0(E)$.

Having identified the upper and lower states involved in a transition a unique fit can be obtained, if either the upper or lower states are well characterised over most of the vibrational displacement responsible for the emission [16,17]. There are several qualitative rules, based on section 1.4, to help in the fitting of structured continua.

### 2.4.1 Low Frequency Envelope of 'Double' Frequency Structured Continua

As mentioned in section 1.4, by taking a quadratic fit to the difference potential, $V_{12}(R)$ at $R_m$ (the point at which $V_{12}'=0$), we avoid the discontinuity in $M_{21}$ suggested by equation 1.19. It can be shown [18], that when $E_1 \gg V_1(R_m)$, the spacing, $\omega^1 - \omega^0$, between the rainbow maximum, $I_0$ and the first supernumerary $I_1$, has a 1/3 power dependence on $K=d^2V_{12}/dR^2\,|_{R=R^*(\omega^0)}$

$$\omega^1 - \omega^0 \simeq (v^2K/h)^{1/3} \times 2.2 \qquad (2.14)$$

where v is the mean relative velocity at $R_m$. This relationship is only valid for, at most, the first three peaks in the low frequency envelope.

The maximum in W(R) will usually lie close to the minimum, $R_e'$, of the upper ion-pair state and so the curvature of $W(R_e')$ can be increased by increasing $\omega_e'$ of the upper state or by shifting the lower state potential relative to the upper state in the direction that reflects $R_e'$ in a steeper portion of the lower state potential.

### 2.4.2 High Frequency Structure of 'Double' Frequency Structured Continua

The periodicity of the high frequency structure underlying the low frequency envelope is given in the primitive semi-classical treatment [18] by

$$\Delta\omega = \pi/\tau_2 \qquad (2.15)$$

where $\tau_2$ is the transit time between $R^*(\omega)$ and the inner turning point on the lower state potential $R^0(E)$. Thus if the high frequency structure in the simulated spectrum is too compressed, either $R^0$ must be increased or $R^*(\omega)$

decreased. This in turn can be achieved by a relative translation of upper and lower state potentials or by a steepening of $V_2$ in the region of the inner turning points of the continuum motion.

### 2.4.3 The Phase of the High Frequency Structure

The phase of the high frequency structure relative to that of the envelope (if present) is governed by the position of the inner wall of $V_2$ or $V_1$ at $R^0(E)$. Consider the radial Schrödinger equation for a purely repulsive continuum state $V(R)=V_0.e^{-R/a}$:

$$-\hbar^2/2\mu.d^2\psi/dR^2 + (-E + V_0e^{-R/a}).\psi = 0 \qquad (2.16)$$

A change of variable $\varepsilon=(8\mu a^2V_0/\hbar^2)^{\frac{1}{2}}.e^{-R/2a}$, in equation 2.16 produces:

$$\varepsilon^2d^2\psi/d\varepsilon^2 + \varepsilon d\psi/d\varepsilon - (\varepsilon^2+(2kai)^2).\psi = 0 \qquad (2.17)$$

This is a modified Bessel Function of imaginary order; $\nu=2kai$. The solution to equation 2.16 at small $\varepsilon$ and large R has the asymptotic form:

$$I_\nu(\varepsilon) = (\tfrac{1}{2}\varepsilon)^\nu/\Gamma(\nu+1) \qquad (2.18)$$

If 'a' remains constant, then $\nu$ also remains unaltered and the denominator in equation 2.18, $\Gamma(\nu+1)$, will have no effect on the phase of the continuum wavefunctions, even if $V_0$ is varied. The change of the inner turning point, $\delta R_0$, with respect to $V_0$ is:

$$\delta R^0 = a/V_0.\delta V_0 \qquad (2.19)$$

The numerator in equation 2.18 suggests the phase relation:

$$\eta = 2ka.\ln(2\mu a^2V_0/\hbar^2)^{\frac{1}{2}} \qquad (2.20)$$

Thus

$$\delta\eta = ka/V_0.\delta V_0$$
$$= k\delta R^0 \qquad (2.21)$$

which is obviously true for a vertical wall potential, where k is the asymptotic wavenumber of the relative motion on the lower potential surface. This phase information cannot locate $R^0(E)$ absolutely but only cyclically. For $Br_2$:$D(0_u^+)$ $v'=136 \rightarrow X^1\Sigma_g^+$ analysed in section 3.4 the precision attainable in this way is <0.05 Å.

### 2.4.4 The Gradient of the Lower State Potential in Single Frequency Spectra

In a band originating at the inner turning point, the 2/3 power plot of the peak index as described in ref [19], continues to be useful in giving a first estimate of the gradient of the lower state potential at the turning point. By linearising the upper and lower states potentials, $V_1(R)$ and $V_2(R)$ respectively, near the inner turning point of the upper state, $R^0(V_1)$, we can approximate the upper and lower state vibrational wavefunctions as Airy functions. A little manipulation [18] yields expression 2.22:

$$\omega^n - \omega^0 = (3/2.\pi\,|V_2'|)^{2/3}.(|V_1'-V_2'|/2\mu\hbar\,|V_1'|)^{1/2} \times [(n+1/4)^{2/3} - 1/4^{2/3}] \qquad (2.22)$$

where $\omega^n$ are the peak position labelled from $\omega^0$ the band origin. $V_i'$ are the constant potential gradients. It is found that when W(R) is a fairly slowly varying function, $V_2'$ can be recovered to within roughly 10% but tends to be on the low side (see section 3.4.2.2). This may be because the transition moment, which is assumed constant in the above treatment, has 'clipped' and distorted the peak positions artificially compressing their 'true' spacing.

### 2.4.5 First Approximation to the Transition Moment Function

Successive peaks $I_n$ depend upon both the gradient of the difference potential at $R^*(\omega)$ and the strength of the transition moment function at that point.

$$\frac{I_n}{I_m} = \left[\frac{\omega^n}{\omega^m}\right]^3 \cdot \frac{\mu_{12}(R_n^*)^2}{\mu_{12}(R_m^*)^2} \cdot \left[\frac{W'(R_m^*)k_m}{W'(R_n^*)k_n}\right] \qquad (2.23)$$

In the preliminary rounds of fitting, the potentials are secured by simulating the peak positions using a constant reference transition moment, $\mu_{ref}$. This determines the gradient of W(R) in the Franck-Condon region and hence, by using equation 2.24 in simple ratio form

$$I_n^{obs}/I_n^{sim} = \mu_{12}(R_n^*)^2/\mu_{ref}^2 \qquad (2.24)$$

a first approximation to the transition moment function can be obtained at selected points, usually the $R_n^*(\omega)$. As will be seen $\mu_{12}(R)$ is often a rapidly varying function over the range of R probed by the fluorescence (e.g. fig 5.11), and can distort the peak positions. One or two more rounds of adjusting the

potential are sometimes needed with the realistic $\mu_{12}(R)$ function. Care must be exercised when simulating spectra where only an estimate of the instrument response is available and the conclusions drawn suitably guarded. The derived function $\mu_{12}(R)$ is still directly convoluted with the detector response function.

## References.


1. B. Numerov, Publ. Observatoire Central Atstoph. Russ., 2, 188, (1933).
2. L. Fox and D.F. Mayers, 'Computing Methods for Scientists and Engineers', Oxford Univ. Press, pp 206-208, (1968).
3. J.W. Cooley, Math. Computation, XV, 363, (1961).
4. R.N. Zare, J. Chem. Phys., 40, 1934, (1964).
5. J.K. Cashion, J. Chem. Phys., 39, 1872, (1963).
6. K.P. Lawley and R. Wheeler, J. Chem. Soc., Faraday Trans. 2, 77, 1133, (1981)
7. 'The Airy Integral', Math. Tables, part-vol. B, British Assoc. for the Adv. of Science.
8. Y.P. Varshni, Rev. Mod. Phys., 29, 664, (1957).
9. F. Jenč, Ad. in Atomic and Mol. Phy., 19, 265 (1983).
10. J. Tellinghuisen and M.B. Moeller, Chem. Phys., 50, 301, (1980).
11. J.A. Coxon, J. Quant. Spec. Radiat. Trans., 11, 443, (1971).
12. R.J. Le Roy, J. Chem. Phys., 52, 2683, (1970).
13. J.B. Tellinghuisen, M.R. McKeever and A. Sur, J. Mol. Spectrosc., 82, 225, (1980).
14. A.E. Douglas and A.R. Hoy, Can. J. Phys., 53, 1965, (1975).
15. E.M. Weinstock and A. Preston, J. Mol. Spectrosc., 70, 188, (1978).
16. J.B. Tellnghuisen, Can. J. Phys., 62, 1933 (1984)
17. K.P. Lawley, D.I. Austin, R.J. Donovan and A. Yencha submitted to Chem. Phys. (1987).
18. K.P. Lawley, private communication (1984)
19. K.P. Lawley, M.A. MacDonald, R.J. Donovan and A. Kvaran, Chem. Phys.Lttrs., 92, 322, (1982).

# CHAPTER 3
# BROMINE

## 3.1 Introduction

Several ion-pair states of $Br_2$ have been successfully characterised around their equilibrium bond length. A summary of their molecular constants is given in table 3.1. Recently, the most successful technique in accessing the ion-pair states has been by a sequential two photon excitation process through the intermediate $B^3\Pi_{0u}^+$ valence state [1-5]. Termed optical-optical double resonance (OODR), this technique avoids working in the vacuum ultraviolet (VUV), as required by single photon direct access, but has the disadvantage of there only being favourable Franck-Condon factors to relatively low lying ion-pair vibrational levels (v'<30 typically).

Tellinghuisen and co-workers [6,7] have also studied the emission spectra of $Br_2$ in Ar. His analysis of the $D'(2_g) \rightarrow A'(2_u)$ transition shows facile collisionally induced transfer between states of the ion-pair manifold; this has been exploited in the design of the halogen lasers (e.g. the $F_2$ laser, section 3.2.2).

Prior to the above studies, in 1969 Venkateswarlu, using conventional high resolution techniques [8], studied the single photon absorption spectra of $Br_2$ giving a detailed analysis of several Rydberg states converging on the $Br_2^+:{}^2\Pi_{3/2g}$ and ${}^2\Pi_{1/2g}$ ionisation limits. However, no analysis was given for an extensive, discrete ion-pair absorption system in the region 150-170 nm. Fluorescence from this ion-pair state has been observed following laser excitation at 157.8 nm [9] and by excitation with atomic bromine lines at similar wavelengths [10].

In this chapter new observations of ion-pair (150-170 nm) absorption using synchrotron radiation are presented; a detailed fitting of the partially resolved ion-pair structure is proposed. Franck-Condon arguments dictate that single photon absorption must be to high lying vibrational levels of the ion-pair states (v' > 100); this naturally compliments the three photon OODR work involving the lower vibrational levels. Single isotope VUV dispersed fluorescence studies of $^{81,81}Br_2$ using an $F_2$ laser are also discussed. The phenomena of isotopic 'washing-in' is demonstrated and the three fluorescence systems observed by MacDonald et al [9] at 285 nm, 360 nm and 440 nm are successfully simulated. All the potentials involved proved consistent with the analysis of the absorption spectra.

Table 3.1

Spectroscopic constants for valence and ion-pair states of $Br_2$

| State | $J_{Br}$ [a)] | $J_{Br}$ | $T_e/cm^{-1}$ | $\omega_e/cm^{-1}$ | $\omega_e X_e/cm^{-1}$ | $R_e/\AA$ | $T_\infty/cm^{-1}$ | Ref. |
|---|---|---|---|---|---|---|---|---|
| $F(0_u^+)$ | 0 | 0 | 53900 | 154.8 | 0.78 | 3.276 | 88082 | 2, 35 |
| $f(0_g^+)$ | 0 | 0 | 53102 | 152.8 | 0.42 | 3.167 | 88082 | 3 |
| $(1_g)$ | 1 | 0 | 52641 | 153.9 | - | 3.17 | 87619 | 36 |
| $\gamma(1_u)$ | 2 | 0 | 50213 | 125.5 | 0.087 | 3.22 | 84480 | 37 |
| $D(0_u^+)$ | 2 | 0 | 49928 | 134.5 | 0.087 | 3.175 | 84480 | 1, 4 |
| $E(0_g^+)$ | 2 | 0 | 49778 | 150.8 | 0.41 | 3.197 | 84480 | 5, 6, 38 |
| $\beta(1_g)$ | 2 | 0 | 49390 | 151.7 | 0.41 | 3.183 | 84480 | 39, 40 |
| $D'(2_g)$ | 2 | 0 | 48930 | 150.9 | 0.38 | 3.170 | 84480 | 7 |
| $B(^3\pi_{0u^+})$ | 1/2 | 3/2 | 15902 | 167.6 | 1.64 | 2.678 | 19743 | 29 |
| $A(^3\pi_{1u})$ | 3/2 | 3/2 | 13905 | 153.0 | 2.70 | 2.695 | 16056.9 | 41 |
| $X(^1\Sigma_g^+)$ | 3/2 | 3/2 | 0.0 | 325.3 | 1.08 | 2.281 | 16056.9 | 29 |

a) The J states of the atomic or ionic products that correlate diabatically with the molecular state are given

## 3.2 Experimental

### 3.2.1 The SRS

The absorption and fluorescence excitation studies, the time resolved work and some of the dispersed fluorescence spectra (figures 3.5-8), were all performed using the synchrotron radiation source (SRS) at the SERC Daresbury Laboratory. The experimental details are well documented elsewhere [11-14] and only the salient features are discussed below.

In 'multibunch' mode 160 discrete electron bunches circulate the main storage ring separated by 2 ns and of 120 ps duration. Alternatively, in 'single bunch' mode only one electron bunch circulates providing a 120 ps light pulse every 320 ns. Typical operational parameters were 2.0 GeV beam energy with a current of 200 mA (multibunch) or 10-20 mA (single bunch). Light is collected at various ports corresponding to the 17 magnets accelerating the electrons around the ring.

Two ports were used for the work described in this chapter (i) Beam line 13.2 equipped with a 0.5 m normal incidence Seya monochromator with output focused by a $CaF_2$ lens (cut-off 128 nm). The highest effective resolution was ca. 0.1 nm. Line 13.2 was employed to record low resolution absorption and fluorescence excitation spectra, dispersed fluorescence and lifetime studies;(ii) Beam line 3.2 equipped with a 5 m MacPherson monochromator with output focused by a LiF lens (cut-off 105 nm). The highest effective resolution was ca. 0.008 nm. Line 3.2 was employed to record medium resolution absorption and fluorescence excitation spectra.

The absorption observation axis (coincident with the excitation beam) , the fluorescence excitation observation axis and the dispersed fluorescence observation axis were all mutually perpendicular.

The MacPherson and Seya monochromators were initially calibrated by setting their wavelength indicators to zero at the maximum of zero order light Further calibration checks were made against the Schumann-Runge bands of $O_2$ , and final accuracy confirmed by comparison with the known Rydberg absorption of $Br_2$ between 130 nm and 151 nm [8]. The dispersed fluorescence spectra were cross-calibrated by using known emission lines from atomic

iodine produced by excitation of $I_2$ at short wavelengths [15].

Absorption and fluorescence excitation spectra were collected simultaneously. Corrections for changes in synchrotron light intensity and the spectral response of the Seya monochromator have been incorporated in the presented spectra. The dispersed fluorescence spectra are only corrected for the SRS beam decay but not for the spectrometer response (0.25m Spex Minimate monochromator employing a 2400 groove/mm aberration corrected concave holographic grating in the first order).

The data acquisition and processing techniques used for fluorescence lifetime studies have been discussed previously [11].

### 3.2.2 The Fluorine Laser

The experimental set-up was of conventional design [16], and essentially the same as described in reference [9] with the significant introduction of the pure $^{81,81}Br_2$ isotopic combination. An Oxford Lasers KX2 multigas excimer laser, operating on the $F_2$ ($D' \rightarrow A'$) transition was used ($\lambda_e$ = 157.8 nm and $\Delta\lambda$ = 0.05 nm [17]). Laser pulses delivered typically 30-40 mJ over roughly 10 ns. Cavity windows were back coated $MgF_2$ and the beam output along the axis of an evacuated cylindrical chamber connected directly to the sample cell to avoid diminution of the 157.8 nm beam through air. The cylindrical sample cell had a $MgF_2$ entrance window and a Spectrosil quartz transverse observation window. The resulting fluorescence was dispersed using a Jobin-Yvon 0.3 m monochromator equipped with either a low resolution (2.6 nm) or a high resolution (0.3 nm) grating. The signal was detected and stored with an optical multichannel analyser (Princeton Applied Research EG&G OMA II) with a silicon diode array head [18]. To maintain purity and extend the beam lifetime the lasing gas mix of He and $F_2$ was continually circulated via a liquid $N_2$ cold trap.

As demonstrated in reference [9], the red line emission of atomic fluorine did not cause coincidental pumping of the A or B states and could safely be ignored.

All spectra were background corrected and calibrated against known resonances from Mercury and Neon discharge lamps [19]. However, no correction for monochromator response has been made, although it is assumed

to increase very slowly to the red over the relatively narrow spectral ranges probed by the observed spectra. In addition it was found that the diode array sensitivity across the detector head broadly peaked around its centre and decayed slightly towards the wings. Since all the laser spectra reproduced (figures 3.9–10 & 3.12–13) involved composites of several 'exposures' of the array head, relative intensity comparisons of widely spaced peaks across any system must be made with care. This has specific implications for any discussion of the transition dipole moments.

All the $F_2$ laser observations were performed at the SERC Rutherford and Appleton Laboratory's Ultraviolet Radiation Facility.

## 3.3 Observations

### 3.3.1 The VUV Absorption Spectrum

The absorption spectrum of $Br_2$ recorded using synchrotron radiation between 125–175 nm exhibits two types of structure (figure 3.1). An extensive, discrete band system between 148 and 169 nm with a local vibrational spacing of 70 $cm^{-1}$ at 159 nm decreasing to 57 $cm^{-1}$ at 152 nm (figure 3.3). And, below 151 nm, numerous sharp and intense systems with a local vibrational spacing of 330 $cm^{-1}$ under a Gaussian envelope. The former is characteristic of absorption to high on the inner wall of a broad diffuse ion–pair state (see Table 3.1).

The selection rules governing such transitions from the ground state are:

$$g \leftrightarrow u \; ; \; g \not\leftrightarrow g \; ; \; u \not\leftrightarrow u \qquad (3.1)$$

and

$$\Delta\Omega = 0,+1 \qquad (3.2)$$

These, combined with the absence of any analogous absorption to the red suggest the upper state must be either the $D(0_u^+)$:(1441) or the $\gamma(1_u)$:(2332); both members of the first cluster of ion–pair states. Of these, only the D state involves a single electron rearrangement from the $X(^1\Sigma_g^+)$:(2440) configuration, this may explain why $\Delta\Omega$=0 transitions are characteristically strong in such halogen/halide transitions [20]. The $\gamma(1_u) \leftarrow X(0_g^+)$ transition is not forbidden but is expected to be weak, although configuration interaction with the close lying

Low resolution absorption (solid line) and fluorescence excitation (dotted line) spectra of $Br_2$ ($\Delta\lambda$ = 0.1 nm).
For the fluorescence excitation spectrum fluorescence was monitored in the VUV region (120–200 nm). Mixed isotope (natural abundance) $Br_2$ was used at a pressure of 130 mTorr in fluorescence and 67 mTorr in absorption.

Figure 3.1

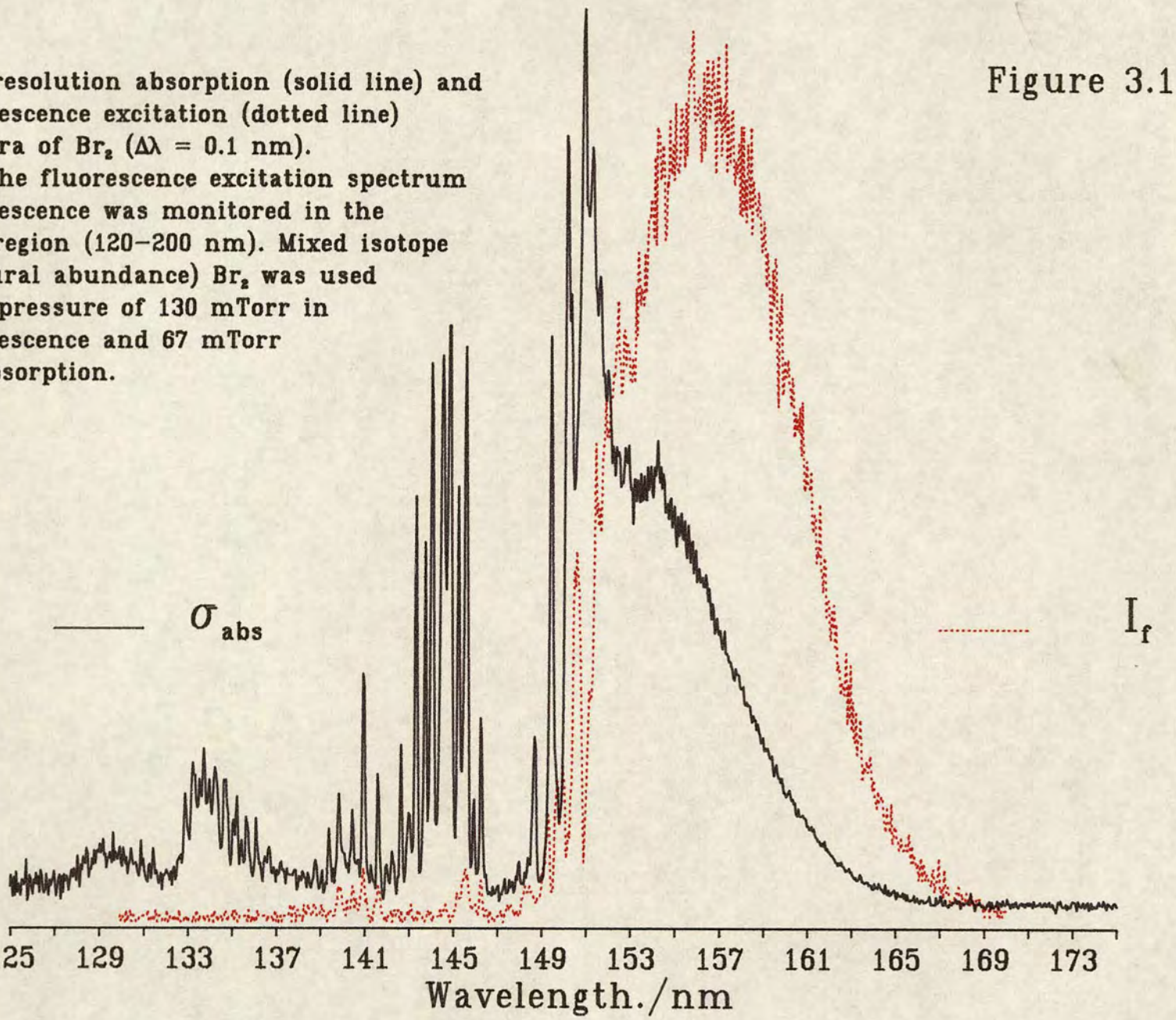

Low resolution absorption (solid line) and fluorescence excitation (dotted line) spectra of $Br_2$ ($\Delta\lambda$ = 0.1 nm). For the fluorescence excitation spectrum fluorescence was monitored in the region 200–600 nm (compare this with figure 3.1 where VUV fluorescence, 120–200 nm, was monitored). The other conditions are the same as for figure 3.1 (except P=67mTorr).

Figure 3.2

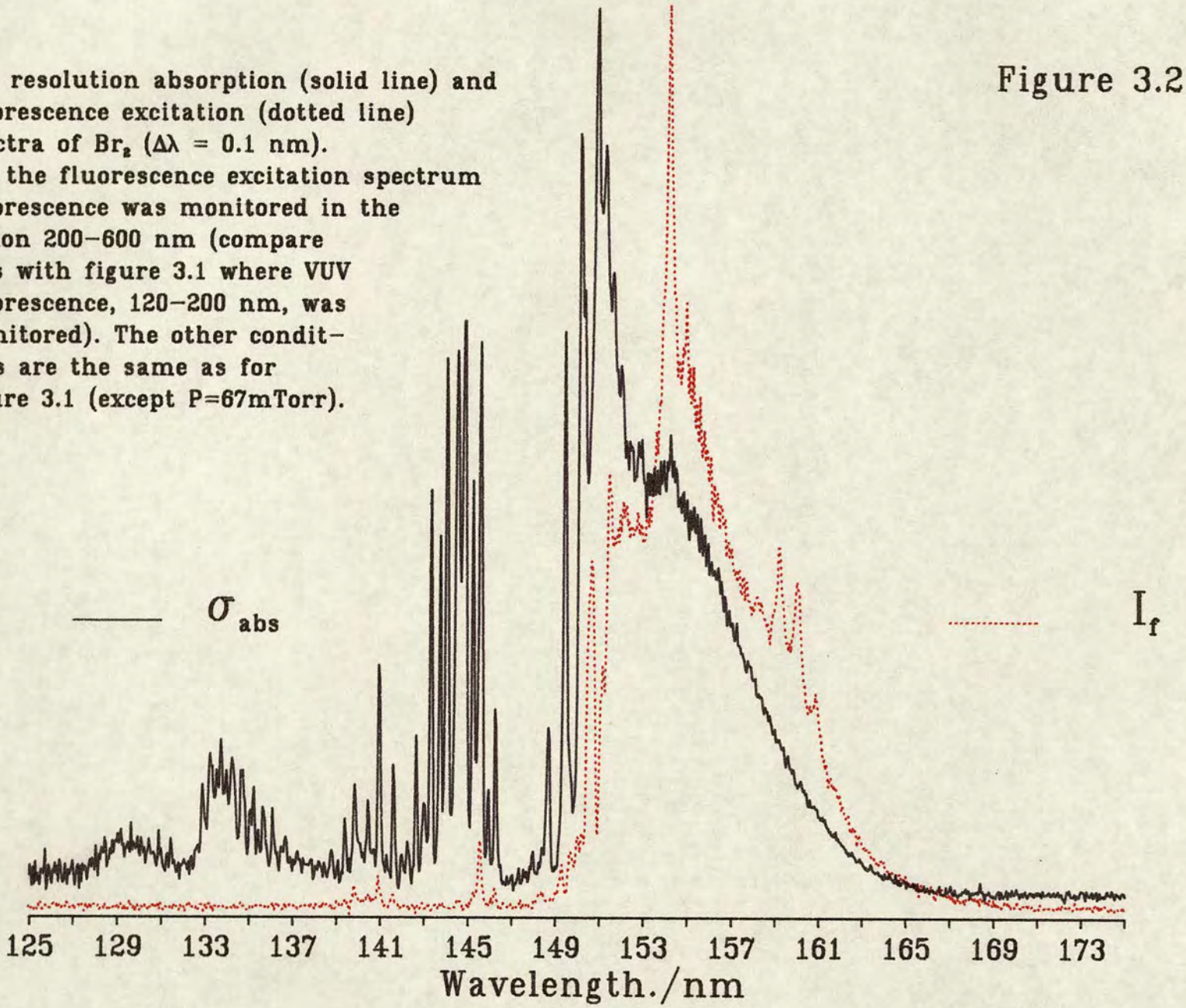

Figure 3.3

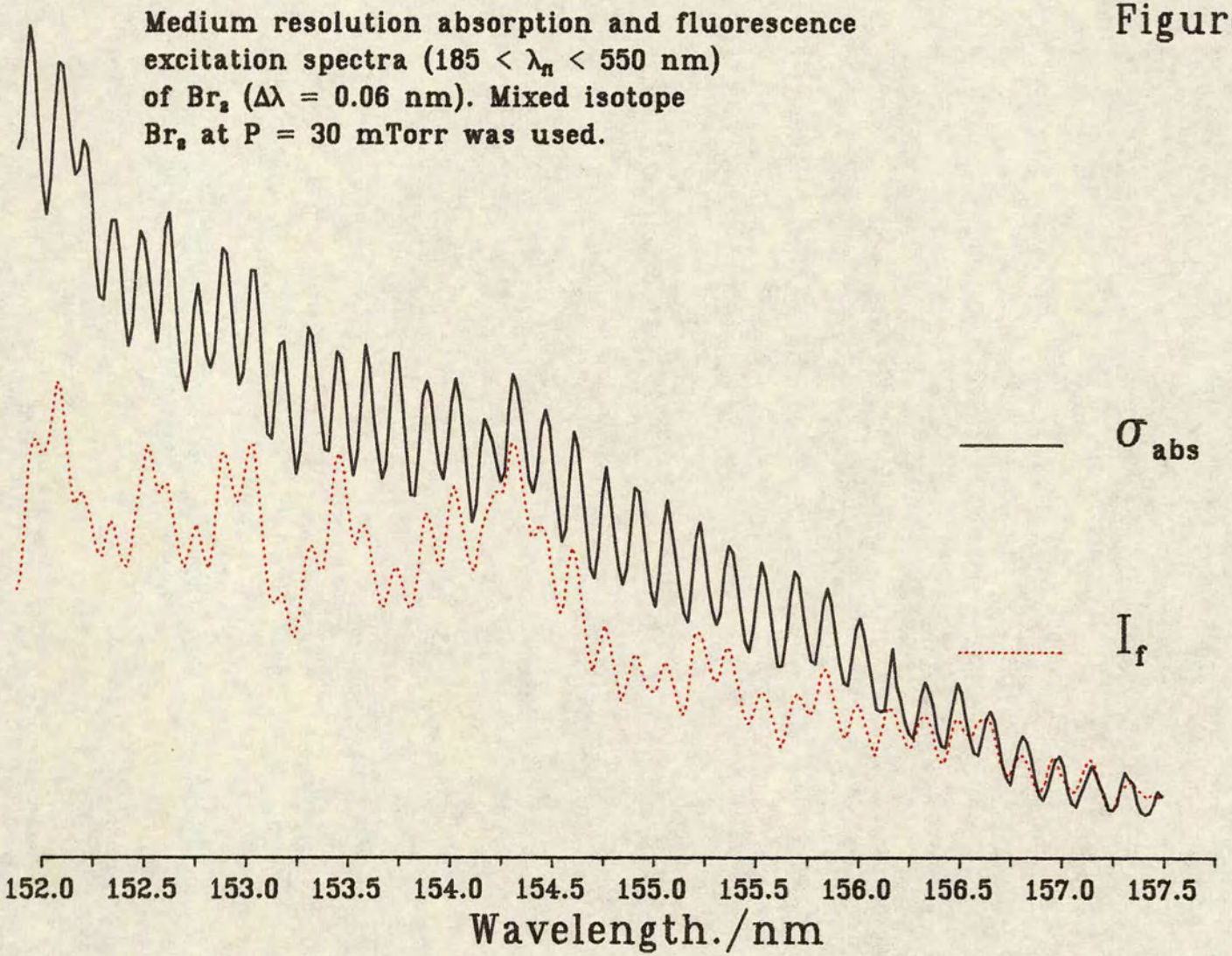
Medium resolution absorption and fluorescence excitation spectra (185 < λn < 550 nm) of Br2 (Δλ = 0.06 nm). Mixed isotope Br2 at P = 30 mTorr was used.
σabs
If
152.0 152.5 153.0 153.5 154.0 154.5 155.0 155.5 156.0 156.5 157.0 157.5
Wavelength./nm

Rydberg $[(2340),Br_2^+](n+1)\pi_g$ state may strengthen it (as with IF [20]).

A quadratic, equation 3.3, was fitted through 41 partially resolved vibronic levels (table 3.3):

$$E_{v+n} = E_v + a_1 n + a_2 n^2 : 0<n<40 \qquad (3.3)$$

where

$E_v = 63243.1\ cm^{-1}$ (=158.12 nm)
$a_1 = 69.27\ cm^{-1}$
$a_2 = -0.1527\ cm^{-1}$
$\sigma = 3\ cm^{-1}$ (std.dev.)

(n.b. $\Delta(E_{v+n+1} - E_{v+n}) = 69.117 - 0.3054\ n$). In section 3.4.1 we assign v = 133 for $^{79,81}Br_2$, assuming normal rotational and vibrational populations in the ground state.

The wider spaced structures below 151 nm are transitions to low lying levels ($0<v'<6$) of Rydberg states and have been extensively analysed and assigned by Venkateswarlu using a 10.7 m spectrograph and photographic plates [8]. With the advantage of relative intensities a new numbering for the $h_5$ and $i_5$ series is proposed, suggesting a more normal Gaussian absorption profile (Table 3.2). The mammoth perturbation of the $h_5(3,0)$ level for which no explanation was proffered, is also avoided. Neither the location of the $d_5(0,0)$ band nor the fitting of the $d_n$ series formula (equation 1.2) have been altered. However, the inherent problems of 'integrating' high resolution work to compare with medium suggest that a high resolution spectrum with reliable relative intensities is necessary to fully resolve this minor discrepancy.

The lines identified in table 3.2 provided a useful calibration check on the other methods described in section 3.2.1.

### 3.3.2 The Fluorescence Excitation Spectrum

Ion-pair fluorescence is known to extend from 440 nm down to the excitation wavelength ([9] and section 3.3.3). Any Rydberg fluorescence to the ground state will be confined to the vacuum ultraviolet region, and if to low lying valence states, the ultraviolet. In figure 3.1 the synchrotron fluorescence excitation spectrum was recorded by monitoring fluorescence in the 120-200 nm region, and in figure 3.2 by monitoring fluorescence between 200 and 600 nm.

Table 3.2

Assignment of some Rydberg series of $Br_2$

| line position | | assignment | | | | | |
|---|---|---|---|---|---|---|---|
| /$cm^{-1}$ | /nm | previous work [8] | | | | this work | |
| 66227 | 151.0 | $d_5(0,0)$ | | | | $d_5(0,0)$ | |
| 66473 | 150.4 | | $e_5(0,0)$ | | | | $e_5(0,0)$ |
| 66559 | 150.2 | $d_5(1,0)$ | | | | $d_5(1,0)$ | |
| 66885 | 149.5 | $d_5(2,0)$ | | | | $d_5(2,0)$ | |
| 67203 | 148.8 | $d_5(3,0)$ | | | | $d_5(3,0)$ | |
| 68330 | 146.3 | $h_5(0,1)$ | | | | $h_5(0,1)$ | |
| 68491 | 146.0 | | $i_5(0,1)$ | | | | $i_5(0,1)$ |
| 68651 | 145.7 | $h_5(0,0)$ | | | | $h_5(0,0)$ | |
| 68813 | 145.3 | | $i_5(0,0)$ | | | | $i_5(0,0)$ |
| 68983 | 145.0 | $h_5(1,0)$ | | | | $h_5(1,0)$ | |
| 69132 | 144.7 | | $i_5(1,0)$ | | | | $i_5(1,0)$ |
| 69357 | 144.1 | $h_5(2,0)$ | | $j_5(0,0)$ | | $h_5(2,0)$ | |
| 69529 | 143.8 | $h_5(3,0)$ | | | | | $i_5(2,0)$ |
| 69721 | 143.4 | | | $j_5(1,0)$ | | $h_5(3,0)$ | |
| 69882 | 143.1 | $h_5(4,0)$ | | | | | $i_5(3,0)$ |
| 70061 | 142.7 | | | $j_5(2,0)$ | | $h_5(4,0)$ | |
| 70234 | 142.4 | $h_5(5,0)$ | | | | | $i_5(4,0)$ |

Table 3.3

Observed and simulated partially resolved vibrational structure for the D state of $Br_2$ : $D(0u^+) \leftarrow X(^1\Sigma_g^+)$

| n | $\lambda_{obs}$ [a] /nm | $\lambda_{sim}$ /nm | n | $\lambda_{obs}$ /nm | $\lambda_{sim}$ /nm |
|---|---|---|---|---|---|
| **40** | 152.06 | 152.08 | | 154.04 | 155.04 |
| | 152.18 | 152.22 | | 155.20 | 155.18 |
| | 152.32 | 152.34 | | 155.34 | 155.34 |
| | 152.46 | 152.48 | | 155.50 | 155.50 |
| | 152.60 | 152.60 | **15** | 155.66 | 155.66 |
| **35** | 152.74 | 152.74 | | 155.82 | 155.82 |
| | 152.86 | 152.88 | | 155.98 | 155.98 |
| | 153.00 | 153.00 | | 156.14 | 156.14 |
| | 153.16 | 153.14 | | 156.30 | 156.30 |
| | 153.28 | 153.28 | **10** | 156.46 | 156.46 |
| **30** | 153.42 | 153.42 | | 156.62 | 156.62 |
| | 153.56 | 153.56 | | 156.78 | 156.78 |
| | 153.72 | 153.70 | | 156.96 | 156.96 |
| | 153.86 | 153.86 | | 157.12 | 157.12 |
| | 154.00 | 154.00 | **5** | 157.28 | 157.28 |
| **25** | 154.14 | 154.14 | | 157.44 | 157.46 |
| | 154.28 | 154.28 | | 157.62 | 157.62 |
| | 154.44 | 154.44 | | 157.80 | 157.80 |
| | 154.58 | 154.58 | | 157.96 | 157.98 |
| | 154.74 | 154.74 | **0** | 158.12 | 158.14 |
| **20** | 154.88 | 154.88 | | | |

[a] estimated error +/- 0.01 nm

In regions of pure ion-pair absorption (153 - 169 nm), peaks in absorption correspond to peaks in excitation fluorescence (figure 3.3), whereas in regions of overlapping ion-pair/Rydberg absorption (148-153 nm) peaks in absorption correspond to minima in fluorescence. Further to the blue (139-147 nm), in regions of pure Rydberg absorption, only very low, $v'<3$ , vibronic levels of the $h_5$, $i_5$, $k_5$, $m_5$ and $l_5$ series contribute to any emission. The higher levels of these series, and all levels of the remaining Rydberg systems down to 127 nm, have very little associated fluorescence. We therefore deduce that these Rydberg states are strongly predissociated and that the $d_5$ or $e_5$ states (see Table 3.2) may act as 'doorway' states to the predissociation of the ion-pair system.

Using port 3 of the SRS (see section 3.2.1), further Rydberg absorption below 120 nm was observed (figure 3.4). This system does not seem to be predissociated and was not reported in reference [8]. An assignment is not attempted here, although the scope for future work is self evident.

The excitation spectra of figures 3.1 and 3.2 differ markedly . The peaks at 154 nm and around 160 nm of figure 3.2 have no counterparts in figure 3.1. In addition, no corresponding features in absorption were observed. Haranath and Rao [21] reported discharge excited Rydberg → ground state fluorescence in the VUV indicating vibronic levels $v'=1,2$ and 3 at 161, 160 and 159 nm respectively. However, further work with filters narrowed the range of anomalous fluorescence to between 310 and 385 nm, this precludes their Rydberg state, labelled C, as the responsible state. It could be that a Rydberg state, perhaps the hitherto unobserved $[(2430),Br_2^+]5s\sigma_u$, with a characteristically small $R_e$, crosses the inner wall of the D state around 62000 $cm^{-1}$, at which point each vibrational level could become coupled to one or more of the densely spaced ion-pair states. This coupling, either Coriolis or spin-orbit in nature, gives some Rydberg character to these ion-pair rovibrational levels in near resonance. These vibronically mixed states have a fluorescence spectrum characteristic of both a Rydberg and an ion-pair state. The former, with only a weakly allowed transition to the ground state will fluoresce in the UV or visible to a repulsive state, as opposed to the much shorter wavelength of the major portion of the D→X fluorescence (see section 3.3.3). However, lifetime studies in this region indicate bi-exponential decay with a long lived component that is absent in other regions of ion-pair absorption (see section 3.3.4). This

Figure 3.4

Medium resolution absorption and fluorescence excitation spectra ($180 < \lambda_n < 550$ nm) of $Br_2$ ($\Delta\lambda = 0.09$ nm). Mixed isotope $Br_2$ at P = 124 mTorr was used.

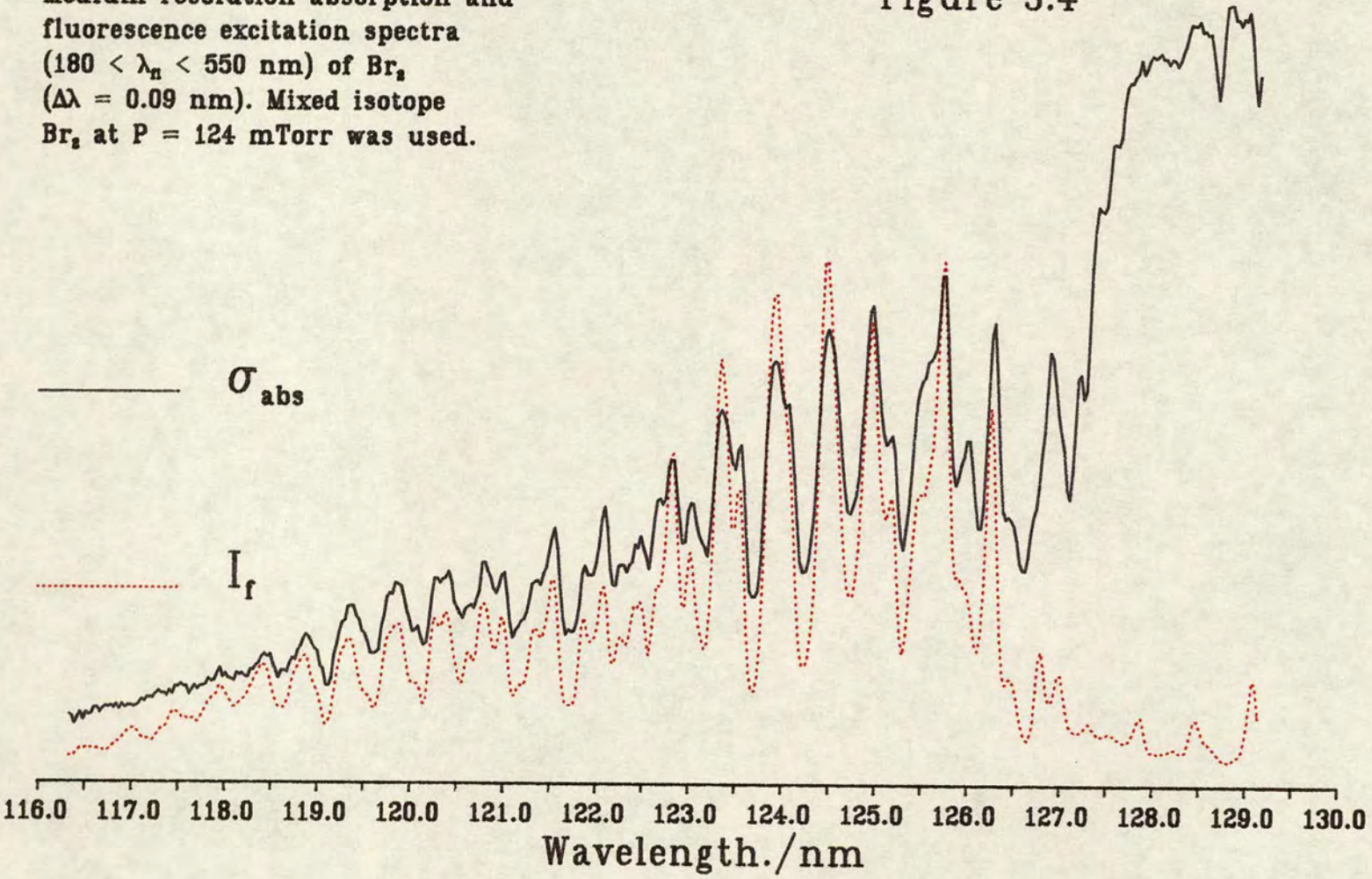

suggests that there is indeed another electronic state involved, but the two lifetimes imply that it is not coupled to the ion-pair state. As yet we do not completely understand these features and further experimental work is required.

### 3.3.3 Dispersed Fluorescence Spectra

Low resolution fluorescence spectra were recorded at 162, 157.8 and 152 nm using synchrotron radiation, (figures 3.5-7 respectively). Emission is observed from 440 nm down to the excitation wavelength. The signal strength excited at 157.8 nm is an order of magnitude stronger than at 162 or 152 nm (c.f. fluorescence excitation in figure 3.1). By comparison with the analogous $I_2$ systems, MacDonald et al [9], using an $F_2$ laser ($\lambda_e$ = 157.8 nm), suggested three separate oscillatory continuum systems; two are associated with repulsive lower states and the third with transitions to unbound (above 210 nm) and bound (below 210 nm) regions of the ground state. The latter is the shortest wavelength system below 290 nm with a maximum at 275 nm extending, presumably, beyond air cut-off down to the excitation wavelength. Both high and low frequency structure are observed within this transition (see Figure 3.10) paralleling the McLennan bands of $I_2$ [22,23] i.e. $I_2$ ($D^1\Sigma_u^+ \rightarrow X^1\Sigma_g^+$).

The two other systems also present structured continua. The 300-360 nm system is shown under higher resolution in figure 3.8 (c.f. figure 3.11) and figure 2 of reference [9]. In contrast to $D(0_u^+) \rightarrow X(0_g^+)$ above, only a single frequency is superimposed on the continuum. The iodine counterpart may be found between 350 and 400 nm [24]. Similarly the 360-440 nm system also exhibits single frequency oscillatory continua and $I_2$ also emits in an analogous spectral region (between 400 and 450 nm) [16,24].

Fluorescence spectra involving wide band width excitation, typical of weak (although tunable) synchrotron radiation, present resolution limitations. Compounding this, as suggested by MacDonald [25], the use of a natural isotopic mix i.e. $^{79,79}Br_2$, $^{79,81}Br_2$ and $^{81,81}Br_2$ in ratio 1:2:1, also imposes a physical constraint. Figure 3.9 shows the D→X band head following excitation by an $F_2$ laser ($\lambda_e$ = 157.8 nm). Although having a much narrower excitation bandwidth ($\Delta\lambda$ = 0.05 nm) and a medium monochromator resolution (FWHM = 0.3 nm), the fine structure seems irregular and 'washed-in' more than would be suggested by the estimated resolution. The high frequency structure has been degraded by a shifting and overlapping of spectra emitted from different

Dispersed fluorescence from $Br_2$ excited by synchrotron radiation at 162 nm ($\Delta\lambda$=2.25nm). Mixed isotope $Br_2$ at P = 440 mTorr was used. (FWHM=4.0nm).

Figure 3.5

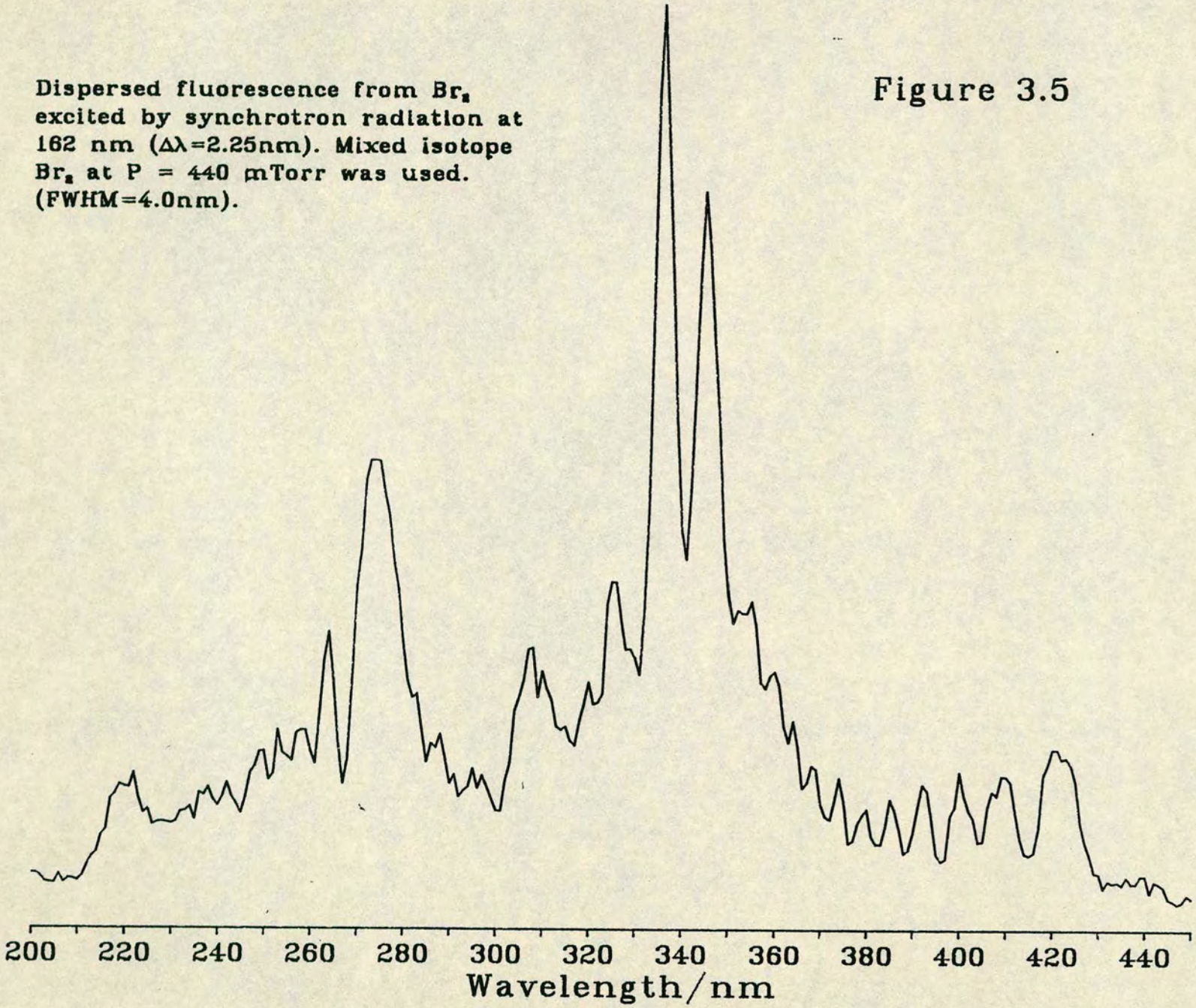

Figure 3.6

Dispersed fluorescence from $Br_2$ excited by synchrotron radiation at 157.8 nm ($\Delta\lambda$=2.7nm). Mixed isotope $Br_2$ at P = 440 mTorr was used. (FWHM=5.0nm).

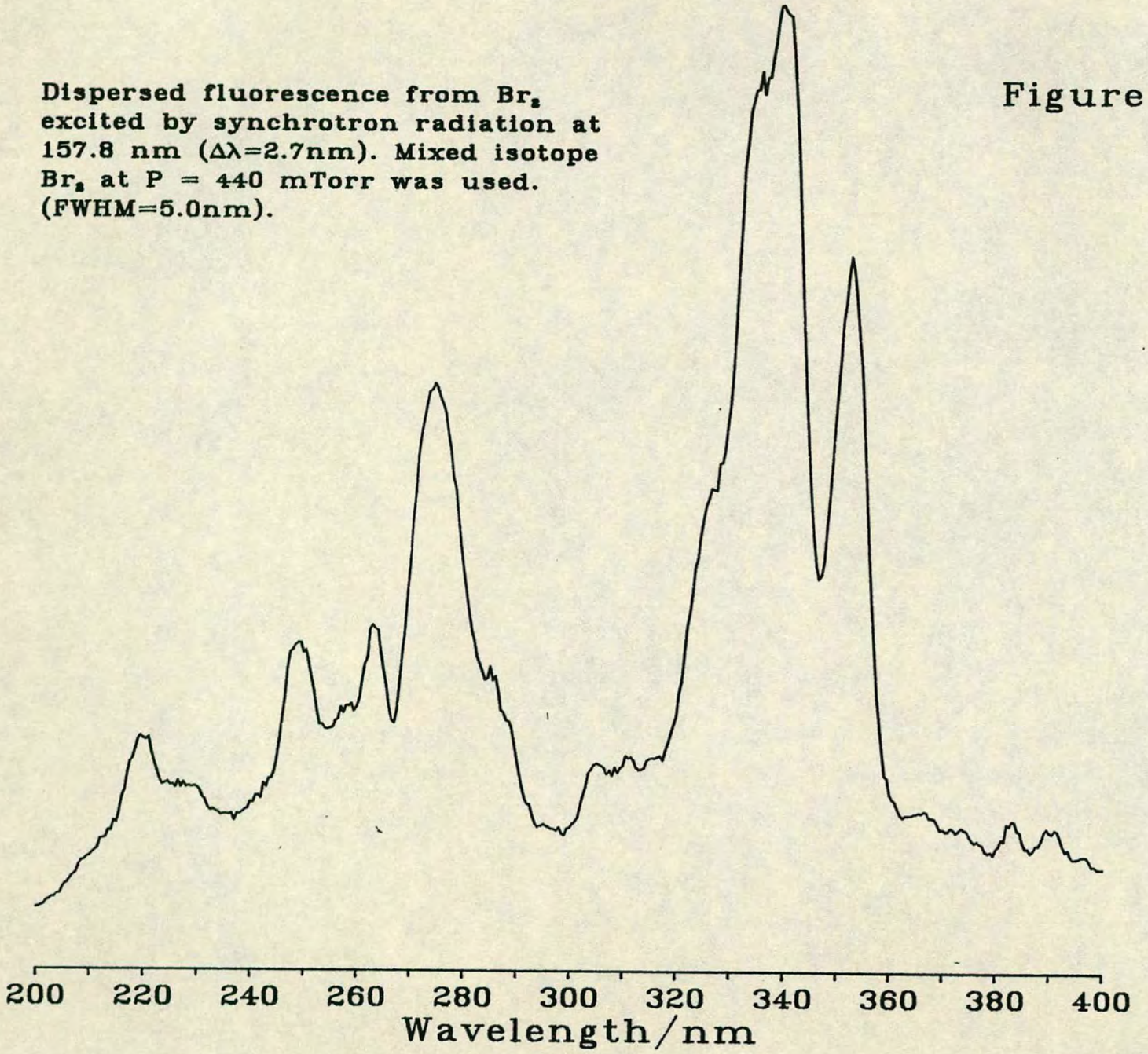

Dispersed fluorescence from $Br_2$ excited by synchrotron radiation at 152 nm ($\Delta\lambda$=2.25nm). Mixed isotope $Br_2$ at P = 440 mTorr was used. (FWHM=5.0nm).

Figure 3.7

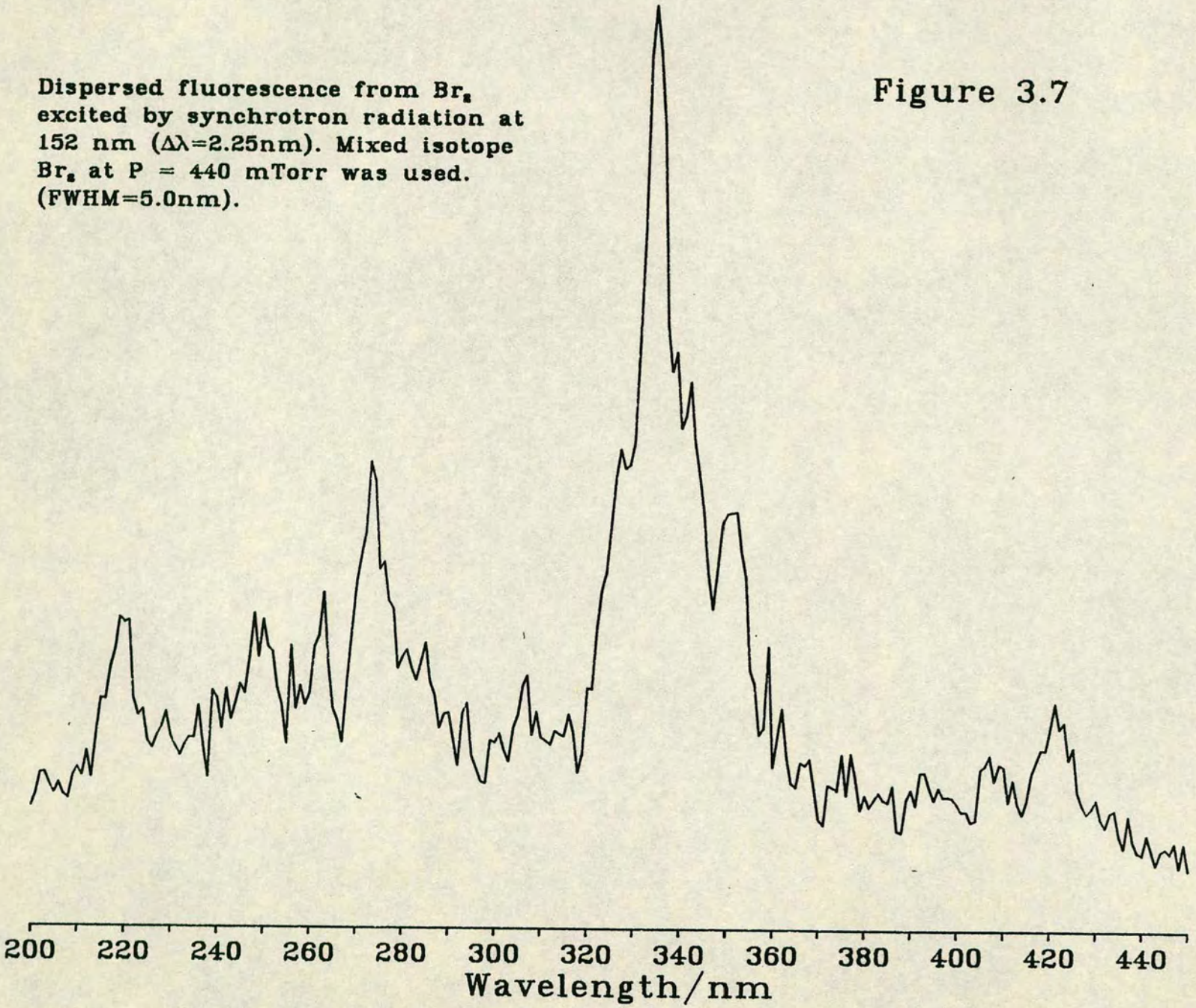

Figure 3.8

**Observed and simulated dispersed fluorescence from $Br_2$ excited by synchrotron radiation at 157.8 nm ($\Delta\lambda$ = 1.35 nm). Mixed isotope $Br_2$ at P = 200 mTorr was used. For simulation details see section 3.4.2.2. (FWHM=0.3nm).**

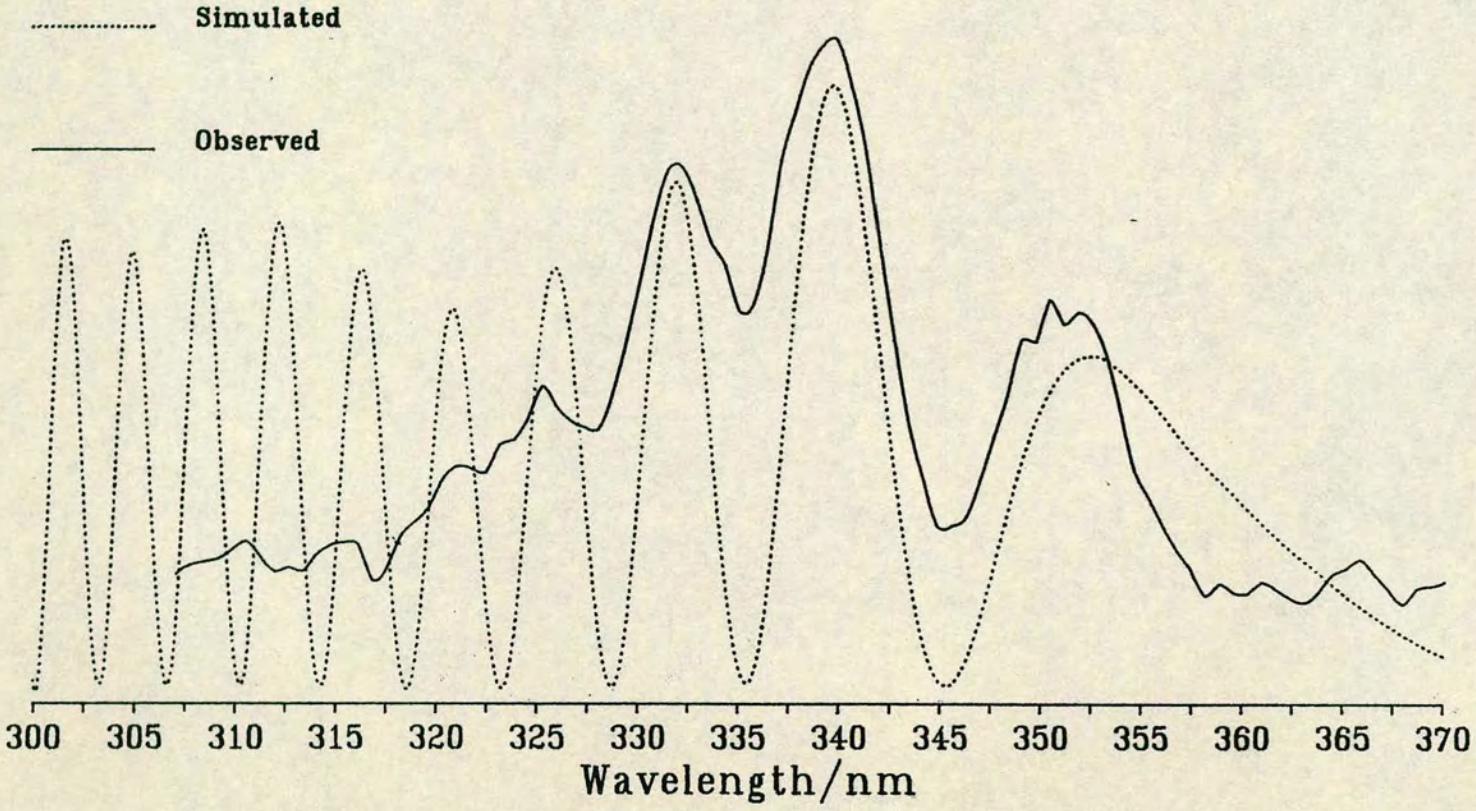

Dispersed fluorescence from $Br_2$ recorded by averaging 500 shots of an $F_2$ laser at 157.8 nm ($\Delta\lambda$<0.05nm). Mixed isotope $Br_2$ at P = 1 Torr was used. (FWHM=0.3nm).

Figure 3.9

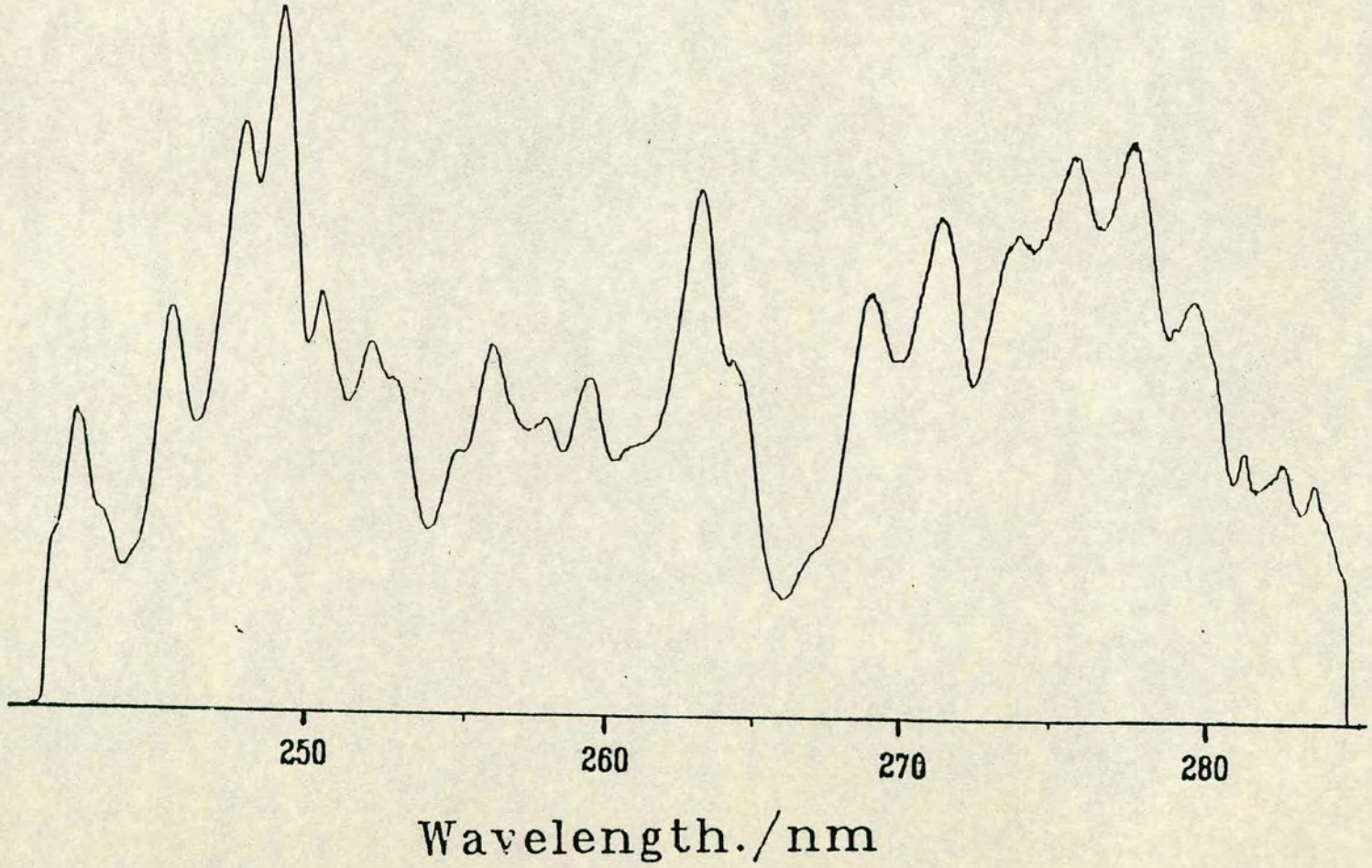

Figure 3.10

Simulated and observed dispersed fluorescence from $Br_2$ recorded by averaging 10 shots of an $F_2$ laser at 157.8 nm ($\Delta\lambda$<0.05nm). Single isotope $^{81,81}Br_2$ at P = 1 Torr was used c.f. fig.3.9 (FWHM=0.3nm). For simulation details see section 3.4.2.1.

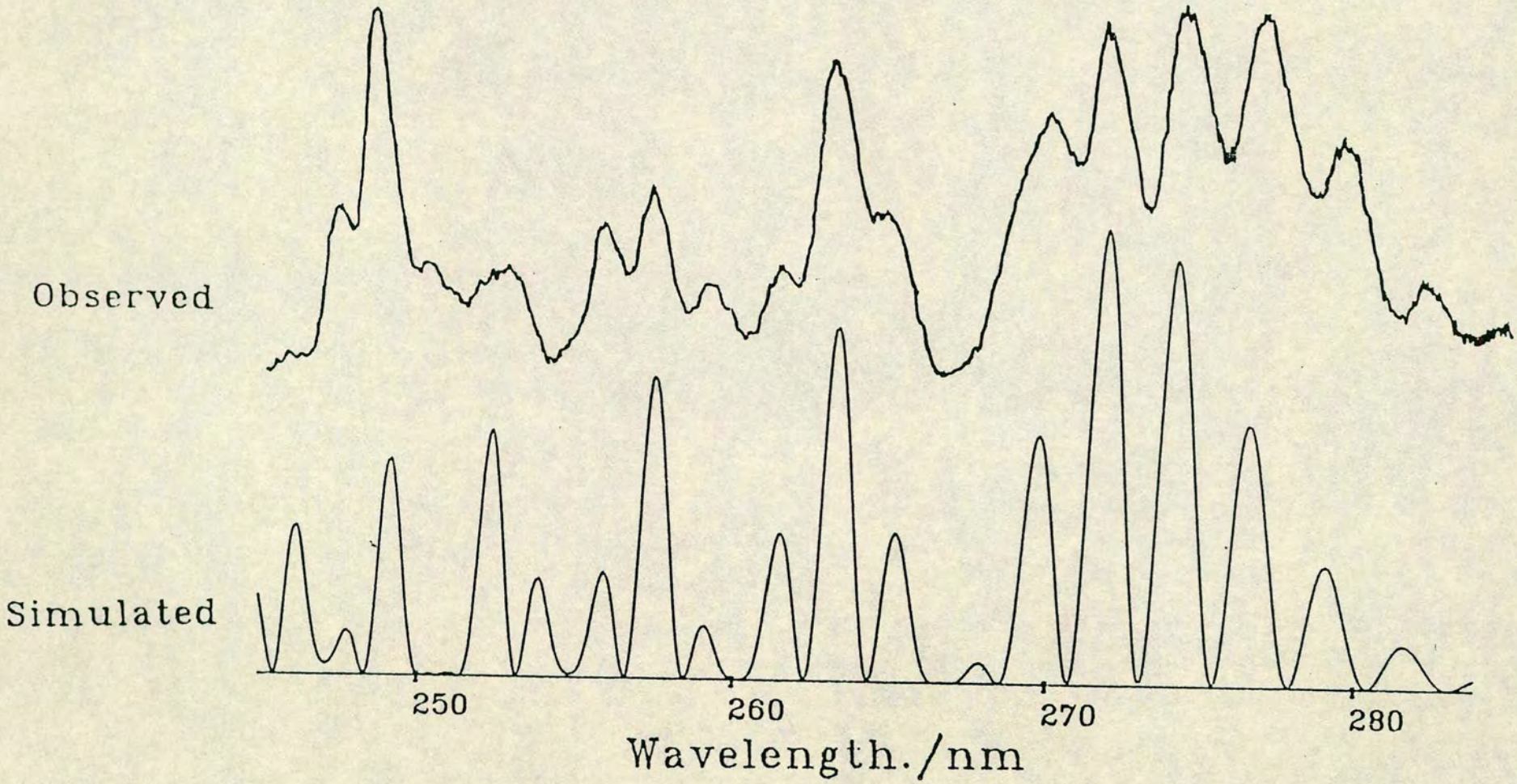

isotopic pairs which are coincidently absorbing. Substituting pure $^{81,81}Br_2$ renders a much cleaner spectrum (figure 3.10) in which both high and low frequencies are clearly visible. Simulations have shown that in $Br_2$, substitution of isotopic pairs as expected, leaves the low frequency structure unchanged but results in a phase shift of the fine structure, markedly reducing the effective resolution (see figure 3.11).

In contrast, the 360 nm and 440 nm systems appear almost unchanged by employing a narrower band pass or a pure isotope (figure 3.12 and 3.13). This confirms our interpretation of these systems as bound → repulsive 'single' frequency fluorescence which are relatively insensitive to excitation energy and isotopic substitution (see section 1.4).

Finally, returning to the D→X fluorescence excited at 157.8 nm (figures 3.6 and 3.10), an anomalous peak at 248 nm cannot be accounted for by pure D state fluorescence (see section 3.4.2.1). Analogous features have been observed with $I_2$ [6], IBr (section 4.3.3) and ICl (section 5.3.5). Figures 3.5 and 3.7 reveal an excitation wavelength dependence and there is also evidence of a pressure dependence. We suggest this emission originates in the $f(0_u^+)$ state [3], the next highest ion-pair state with $0_u^+$ symmetry; population may be direct, by collisional transfer or both. $\Delta T_e$ of the $D(0_u^+)$ and $f(0_u^+)$ states predict the observed rainbow separations to within 1 nm.

Figures 3.5-13 are entirely consistent with our interpretation of the absorption and fluorescence excitation spectra discussed in section 3.3.1 and 3.3.2.

### 3.3.4 Lifetime Studies

Time resolved fluorescence decay was studied at three excitation wavelengths centred at 152 nm, 157.8 nm and 162 nm. These are regions of predominantly ion-pair absorption and fluorescence (see above). The excitation band width was such that roughly eight ion-pair vibrational levels were excited, but the fluorescence in each case followed a single exponential form. Stern-Volmer plots are shown in figure 3.14. All three groups of vibronic states have similar collision free (zero pressure) lifetimes (see Table 3.4). However, the slopes of the three Stern-Volmer plots differ. The cross section for self quenching of the lowest group of vibrational states at 61,700 $cm^{-1}$ (162

Figure 3.11

**Simulation of D−>X fluorescence of $Br_2$ excited at 157.8 nm. The three isotopic combinations are displayed showing very definite 'washing−in' of fine structure.**

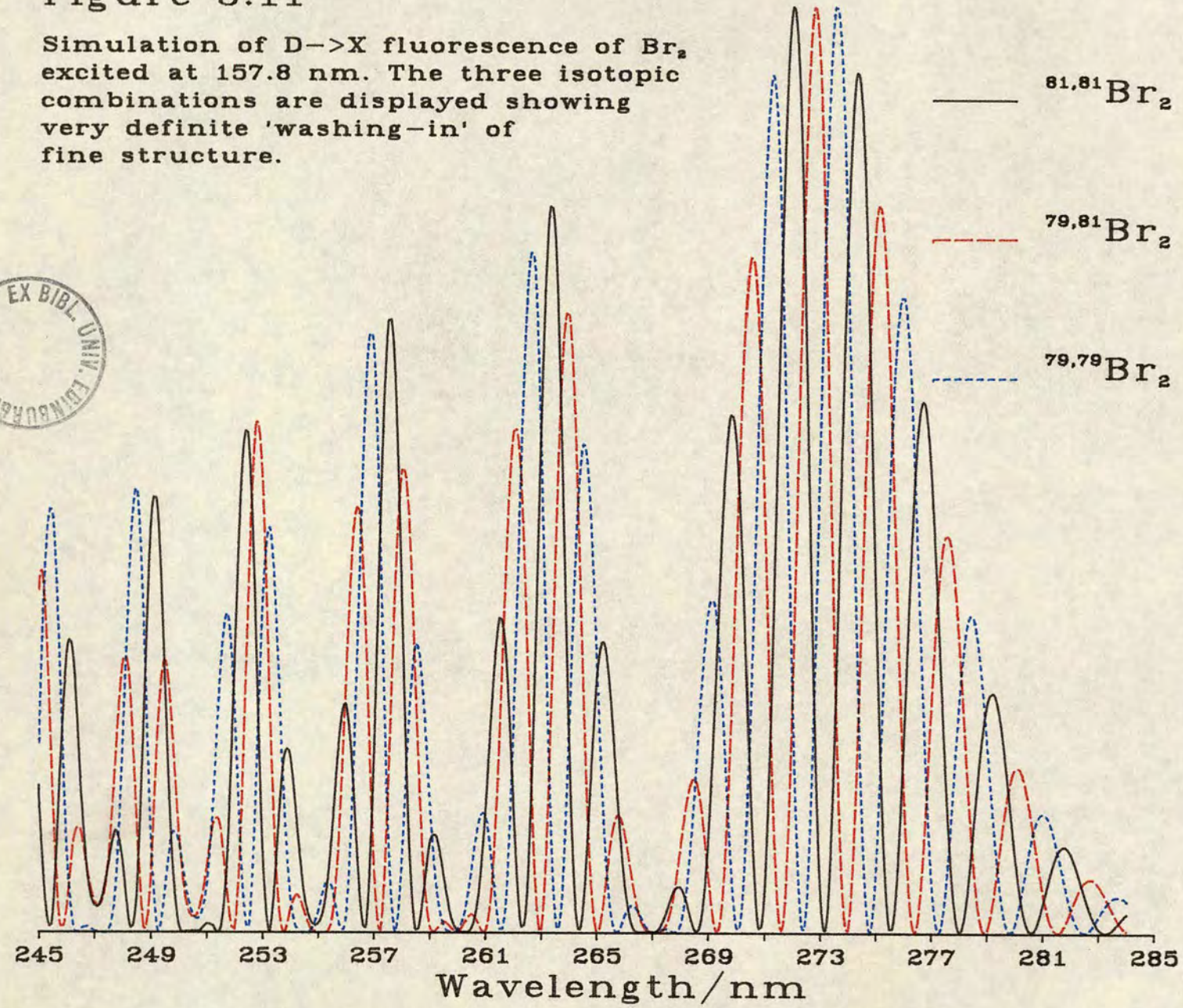

Simulated and observed dispersed fluorescence from $Br_2$ recorded by averaging 10 shots of an $F_2$ laser at 157.8 nm ($\Delta\lambda$<0.05nm). Single isotope $^{81,81}Br_2$ at P = 1 Torr was used c.f. fig.3.8 (FWHM=0.3nm). For simulation details see section 3.4.2.2.

Figure 3.12

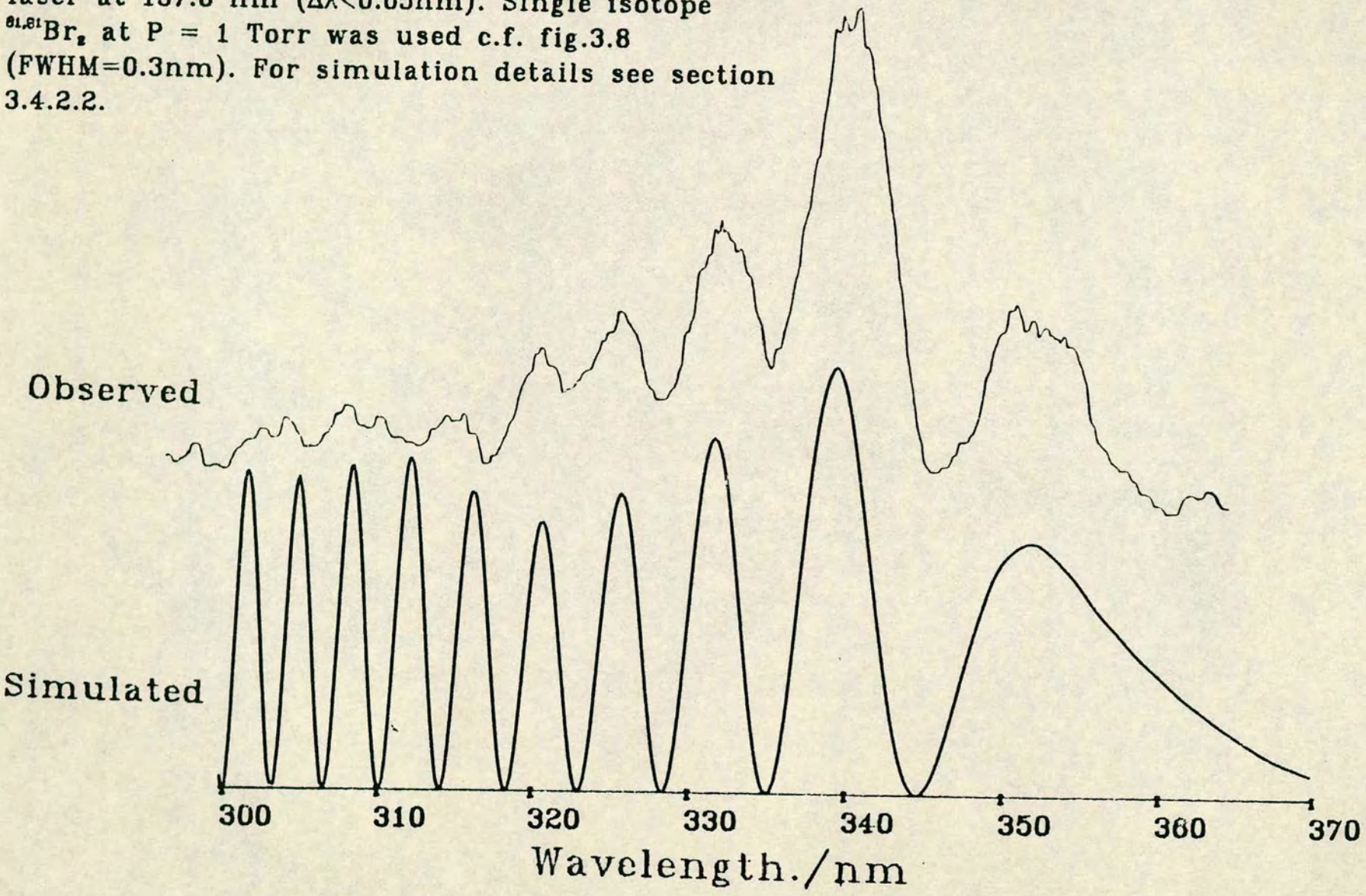

Simulated and observed dispersed fluorescence from $Br_2$ recorded by averaging 10 shots of an $F_2$ laser at 157.8 nm ($\Delta\lambda$<0.05nm). Single isotope $^{81,81}Br_2$ at P = 1 Torr was used (FWHM=0.3nm). For simulation details see section 3.4.2.2.

Figure 3.13

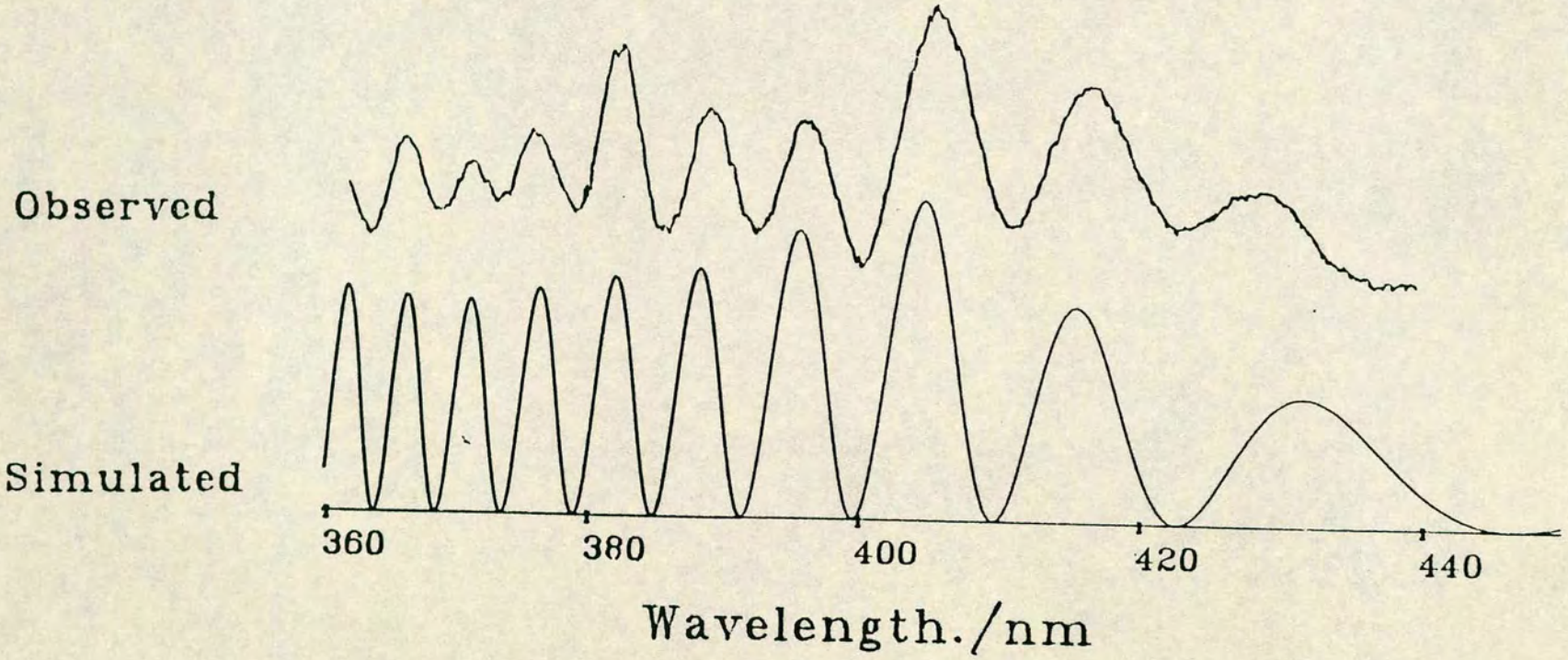

Figure 3.14

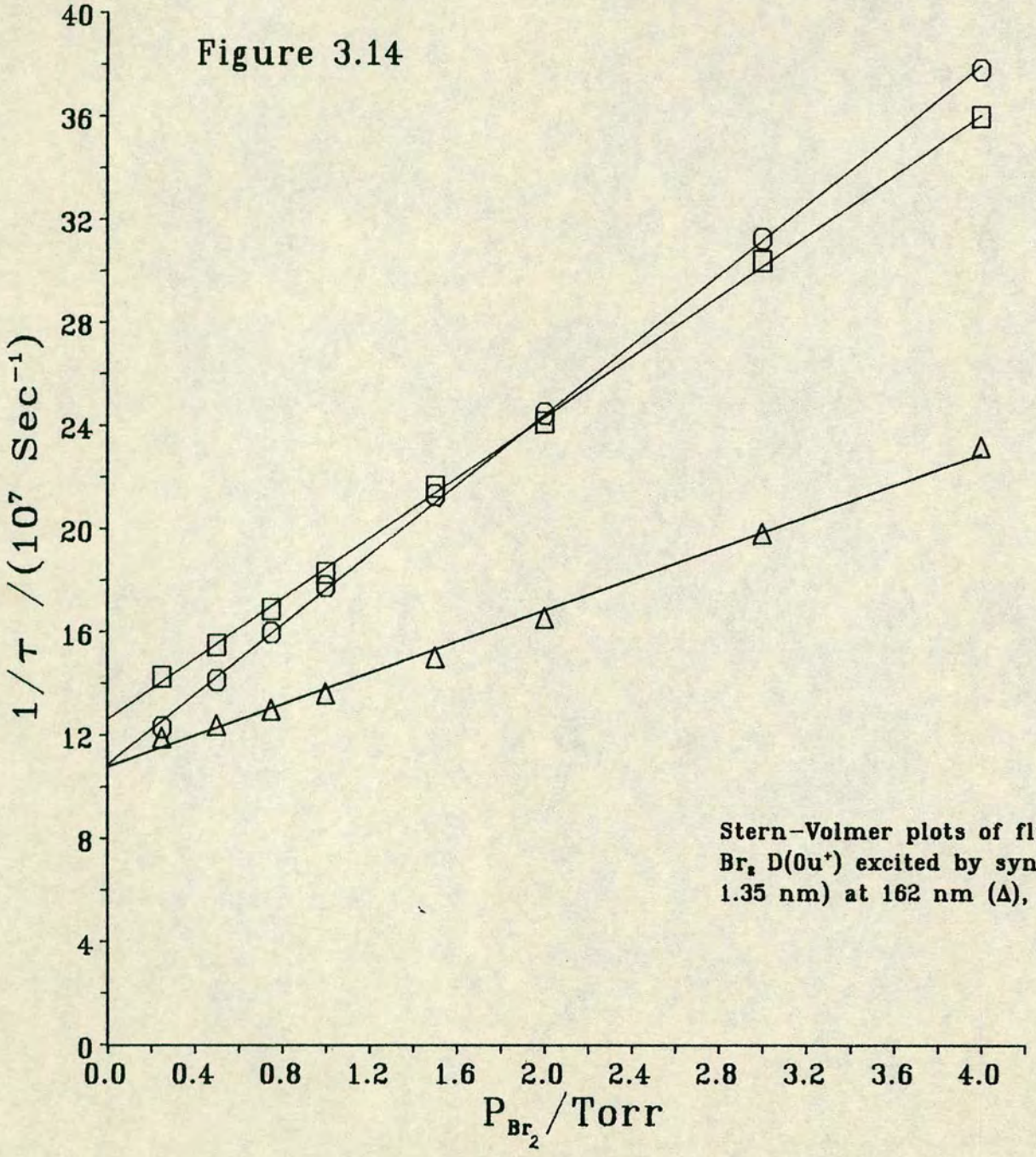


**Stern–Volmer plots of fluorescence lifetimes for $Br_2$ D($0u^+$) excited by synchrotron radiation ($\Delta\lambda$ = 1.35 nm) at 162 nm (Δ), 158 nm (□) and 152 nm (0).**

Table 3.4

Radiative lifetimes for the $D(0u^+)$ state of $Br_2$

| Excitation wavelength*/nm | Lifetime/ns |
|---|---|
| 162 | 9.3 ± 0.4 § |
| 158 | 7.9 ± 0.2 |
| 152 | 9.2 ± 0.4 |

* band pass = 2.6 nm

§ Errors quoted for two standard deviations

nm) is roughly half of that of the higher groups, perhaps indicating the opening of an excitation transfer channel for the latter.

Lifetime data was also obtained for other regions of particular interest. The previously discussed anomalous fluorescence excitation peaks at 154 nm and around 160 nm (see section 3.3.2 and figure 3.2) indicate bi-exponential decay with a long lived component (~20 ns) that is absent in the data plotted in figure 3.14. Similar behaviour was also measured at 152.5 nm a region of both ion-pair and Rydberg absorption. This suggests two very different uncoupled electronic states at these wavelengths.

## 3.4 Detailed Analysis

### 3.4.1 The SRS Absorption Spectrum 148 nm -169 nm

We established in section 3.3.1 that the state responsible for the narrow vibrational spacing in absorption between 152 nm and 169 nm is most likely to be the $D(0_u^+)$ (Table 3.3). An RKR analysis based on the first 17 vibrational levels exists for the D state [4] covering turning points from 2.799 Å to 3.730 Å and up to 10% of De. $T_e$ is firmly located at 49928 $cm^{-1}$. To simulate the absorption spectrum an extensive upper state must be constructed to support the wave functions involved.

A divided difference table of the attractive limb of the RKR points reveals that the point of inflection has not been reached; we must therefore extrapolate before we can use a modified Rittner analytical function (equation 3.4) n.b. for a $Br^+$ ion in the $^3P_{2,0}$ state the anion-quadrupole interaction energy should be positive.

$$V_D(R) = T_\infty - \underset{R>4.5\ Å}{C6/R^6} - C4/R^4 + C3/R^3 - e^2/4\pi\varepsilon_0 R \qquad (3.4)$$

The extrapolation from 3.730 Å to 4.5 Å was based on a successful simulation of figure 3.10; the difference potential involved spanning 2.9 Å to 4.4 Å (see section 3.4.2.1). The coefficients C6, C4 and C3 were than adjusted so that V(R) was continuous in value and gradient at 4.5 Å. A satisfactory potential was obtained with C6=6.6 x $10^5$ $cm^{-1}$ $Å^6$, C4=6.95 x $10^5$ $cm^{-1}Å^4$ and C3=1.9 x $10^4$ $cm^{-1}Å^3$. The value of C4 is roughly 70% greater than suggested by equation 3.5.

$$C4 = e^2/4\pi\varepsilon_0 \cdot \tfrac{1}{2}(\alpha_+ + \alpha_-) = 4.03 \times 10^5 \text{ cm}^{-1}\text{Å}^4 \quad (3.5)$$

$$C6 = 3/2.\alpha_+\alpha_-\omega_+\omega_-/(\omega_+ + \omega_-) = 3.61 \times 10^5 \text{ cm}^{-1}\text{Å}^6 \quad (3.6)$$

Where $\omega_{+/-}$ are the ionic ionisation potentials and $\alpha_{+/-}$ are the ionic polarisabilities. Similarly, C6 is roughly 80% greater than suggested by equation 3.6. Tellinghuisen [23] mistakenly used a negative C3 term in his parameterisation of the D state potential of $I_2$, correcting this would also entail an increase of roughly 50% in C4. We feel this indicates an underestimation of the polarisability of the $Br^-$ and $I^-$ anions by Wilson and Curtis [27]. Care should be exercised however when discussing the physical significance of these values. At 4.5 Å the C3 term is less than 1% of the Coulomb term, the C4 term roughly 6% and C6 term roughly 0.3%. What is important is that the magnitudes and sign of the long range coefficients should be realistic so that the smallness of the contribution of non-Coulomb terms at R>4.5 Å means that the outer branch of the D state potential is constrained to roughly 30 $cm^{-1}$ by the RKR points and the pure Coulomb limb.

The inner limb presents more of a problem. If it is constructed by fitting an exponential $V(R) = Ae^{-bR}$ to the first two RKR points on the inner branch, the potential rises so steeply that virtually no absorption from the ground state would be seen in the 150 nm region (it would in fact occur <130 nm!). Furthermore, it is found that the vibrational energy level spacing predicted by this potential at around $T_e$ + 15,000 $cm^{-1}$ is roughly 68 $cm^{-1}$ , whereas the observed spacing is 62 $cm^{-1}$ (see equation 3.3 n=25). It is clear that the potential must be widened but, within the constraints mentioned above, the outer branch cannot be lowered sufficiently to produce the observed spacing. Consequently we must relax the inner wall. To do this we adopted a more flexible splined potential rather than a functional form. Thirty-four knot points were supplied by the RKR analysis, ten points by the attractive limb as described above and a further eight described the inner wall. Throughout the fitting procedure a careful check was kept on the output of the spline routine, an unwise choice of knot points can induce 'wobbles' and in extreme cases 'spikes'. The resulting inward shift of the inner wall needed to reproduce the local vibrational spacing resulted in a distinct point of inflection (see figure 3.15 and table 3.5).

The simulation included sampling the Boltzmann distribution of initial

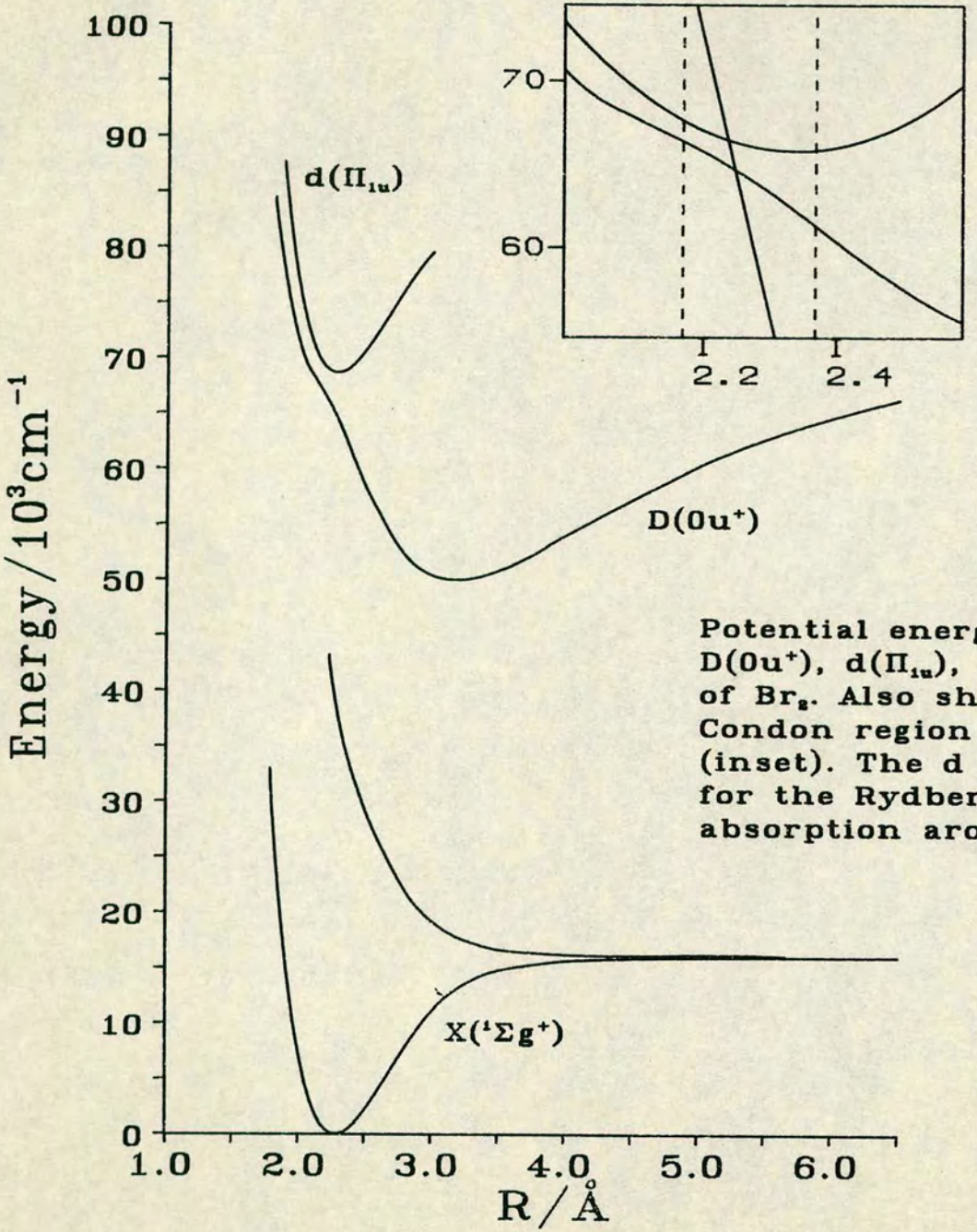


Figure 3.15

Potential energy curves for the $D(0u^+)$, $d(\Pi_{1u})$, and $X(^1\Sigma g^+)$ states of $Br_2$. Also shown is the Franck–Condon region for the upper states (inset). The d state is responsible for the Rydberg system observed in absorption around 150 nm.

Table 3.5

The D state potential defined by the classical turning points of the vibrational levels. The $G_v$ values are appropriate to the $^{79}Br$-$^{79}Br$ isotope and are relative to the potential minimum.

| $R_{min}/\mathring{A}$ | $R_{max}/\mathring{A}$ | $G_v/cm^{-1}$ | v' |
|---|---|---|---|
| 2.695 | 3.981 | 3967.9 | 30 |
| 2.640 | 4.159 | 5161.7 | 40 |
| 2.590 | 4.332 | 6278.1 | 50 |
| 2.542 | 4.497 | 7326.2 | 60 |
| 2.500 | 4.657 | 8320.9 | 70 |
| 2.465 | 4.816 | 9273.0 | 80 |
| 2.434 | 4.975 | 10184.1 | 90 |
| 2.406 | 5.138 | 11052.3 | 100 |
| 2.378 | 5.305 | 11876.5 | 110 |
| 2.352 | 5.475 | 12657.5 | 120 |
| 2.326 | 5.649 | 13396.4 | 130 |
| 2.298 | 5.826 | 14095.0 | 140 |
| 2.269 | 6.005 | 14754.7 | 150 |
| 2.237 | 6.186 | 15377.5 | 160 |
| 2.205 | 6.370 | 15966.5 | 170 |
| 2.175 | 6.556 | 16525.3 | 180 |
| 2.147 | 6.745 | 17057.4 | 190 |
| 2.121 | 6.936 | 17565.1 | 200 |

rotational states in the ground state by 5 values; J"=10,25,36,50 and 65. Using equations 2.13 and 3.7 it is easy to confirm that $J"_{max}$=36 and $NJ"/NJ"_{max}$ = 1/2 when J"=10 and 65 (at 300K). Only the P branches were simulated.

$$\frac{NJ_1}{NJ_2} = \frac{(2J_1+1)}{(2J_2+1)} \cdot \frac{\exp(-EJ_1/kT)}{\exp(-EJ_2/kT)} \qquad (3.7)$$

Furthermore, the Boltzmann distribution of initial vibrational states must also be included. Because $Br_2$ is a relatively heavy molecule, at room temperature v"=1 is significantly populated at 21%. Finally, by including appropriately weighted contributions from all three isotopic combinations and slit convolution with the estimated excitation band width ($\Delta\lambda$ = 0.06 nm) it was hoped we accurately reproduced the prevailing experimental conditions. The result, with a constant transition dipole moment, is illustrated in figure 3.16 and a numerical comparison is given in table 3.3 (c.f. equation 3.3).

By reproducing the observed peak positions and the average vibrational spacings (within experimental error), several important corroborative features arose. The portion of the upper state in the range 10,000–20,000 $cm^{-1}$ above $T_e$ is now accessible from v"=0 (see figure 3.15). The profile of the long tail in the absorption band between 154 nm and 160 nm is also successfully reproduced. In addition, although the simulation was carried out for the three isotopic combinations, the vibrational structure was not washed in. This is because over most of the band, the levels v−1, v and v+1 respectively of the species $^{79,79}Br_2$, $^{79,81}Br_2$ and $^{81,81}Br_2$ are almost coincident. Near the long wavelength limit of the system the three isotopic sublevels are beginning to move out of phase, but we regard the fact that we are able to reproduce the window of partially resolved structure in an isotopic mixture as further proof that our upper state is essentially correct.

From the optimum spline potential, turning points of a band of higher vibrational levels for the $^{79,79}Br_2$ isotopic pair have been extracted, these are listed in table 3.5. Our calculated $G_v$ values allow the absolute numbering of the seven upper state vibrational levels observed by Venkateswarlu [10] to be determined; his level $T_{0v}$ = 63527.16 $cm^{-1}$ is v'=136 (=n is his notation), and follows his numbering scheme 1. An accurate comparison of energy levels reveals differences of typically ±10 $cm^{-1}$ (see also table 3.6 and below) . However, an RKR analysis of the X state based on the rotational and vibrational constants listed in reference [10] produced a severely distorted and 'splayed '

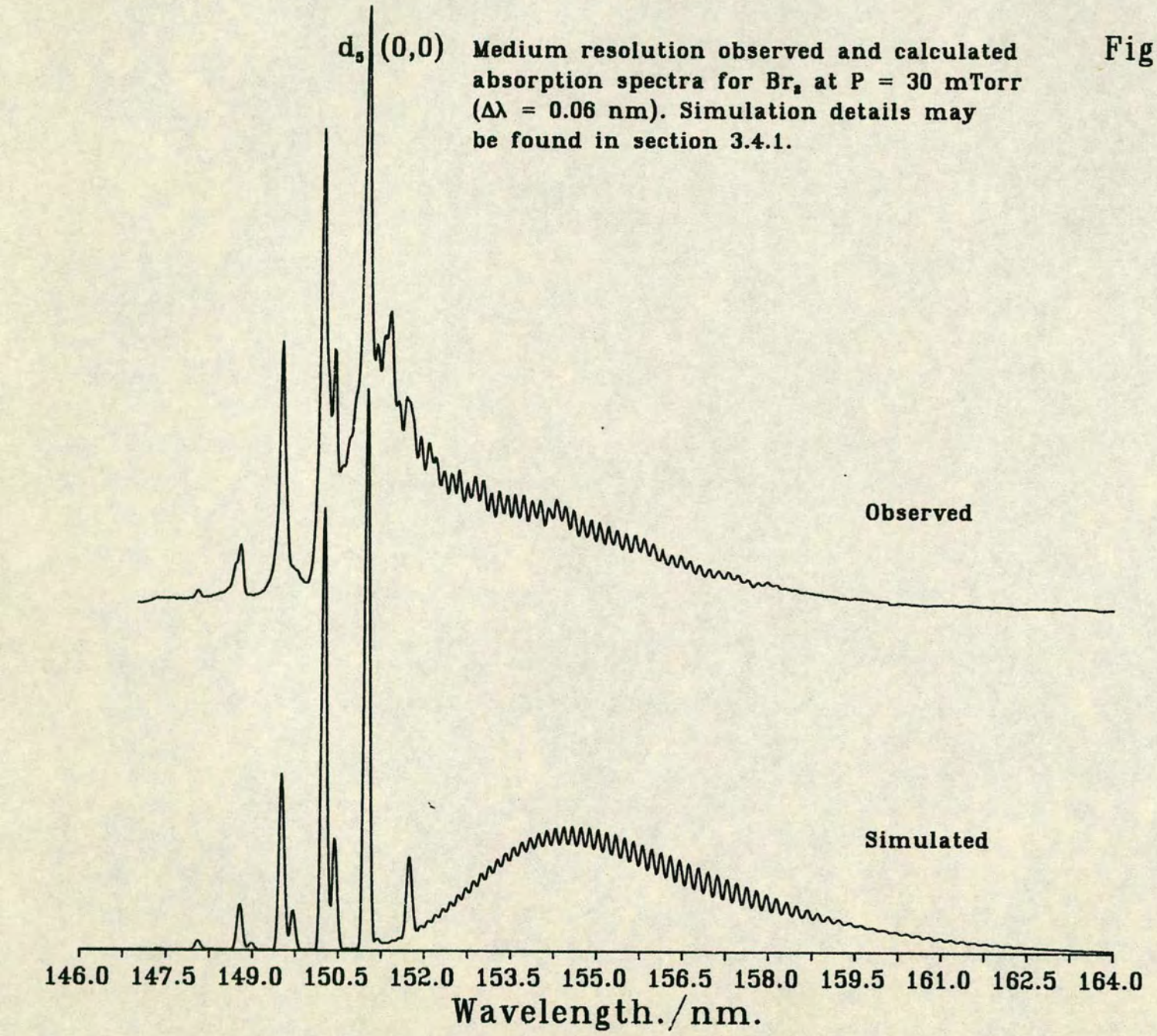


Figure 3.16

**Medium resolution observed and calculated absorption spectra for $Br_2$ at P = 30 mTorr ($\Delta\lambda$ = 0.06 nm). Simulation details may be found in section 3.4.1.**

potential. This is symptomatic of unreliable rotational constants, which coupled with our own relatively high experimental errors probably account for the small differences. As regards equation 3.3 in section 3.3.1, for the $^{79,81}Br_2$ isotopic pair, v is identified as 133 (running up to 173).

The strong Rydberg absorption around 151 nm is assigned to the $d_5(\Pi_{1u})$ state and the weak system to the forbidden $e_5(\Delta_{1u})$ state [8]. Rotational selection rules for such transition are $\Delta J=0,\pm1$ with relative intensities described by the appropriate Hönl-London factors i.e. P, Q and R branches with intensity ratios approximately 1:2:1. To simulate these bands a parabolic potential was fitted to the observed levels as assigned by Venkateswarlu. Thermal Population of v'=1 (hot bands) were again allowed for. However, unlike the ion-pair←ground state transition discussed above, the $B_v$ values of the upper and lower states will be roughly equal. This allows us to safely neglect the lower state Boltzmann rotational distribution since all the Q branches between common vibrational levels will be almost isoenergetic. In addition, since the v' and v" levels involved are all less than 5, all three isotopes will have energy levels lying very close together. We therefore, for economy, only simulated the P, Q and R branches for absorption from v"=0,J"=36 and v"=1,J"=36 in the $^{79,81}Br_2$ isotopic combination. As with the ion-pair states the resultant Franck-Condon factors were slit convoluted.

The full width at half maximum of the simulated Rydberg absorption as shown in figure 3.16, compares favourably with the observed. This indicates that the above approximations and our estimated experimental resolution ( $\Delta\lambda$ = 0.06 nm) are essentially correct.

It was found that the simulation of the Gaussian profile of a Rydberg series was very sensitive to the equilibrium position of the upper state, $R_e'$. However, in the present case we can only proffer estimates because the underlying ion-pair absorption has distorted the true intensity envelope. In the harmonic limit, this technique can only define $|R_e'-R_e''|$. It was found that $|\Delta R_e|$ was 0.059 Å for $d_5(\Pi_{1u})$ and 0.084 Å for $e_5(\Delta_{1u})$, both shifts with respect to the ground state. The violet degradation of both series previously observed by Venkateswarlu indicates that both $R_e'$ are shifted to shorter bond lengths. We estimate in the ideal case, given a flat base line, $R_e'$ may be located to within 0.01 Å, without recourse to any rotational analysis.

The largest discrepancy between simulated and observed spectra is in the 151–153 nm region where the observed absorption continues to rise to a maximum at 151 nm, whereas the simulated absorption peaks at around 154 nm. We first sought to achieve a better fit by introducing a transition moment function that rose sharply in the region around R = 2.2 to 2.3 Å. There is justification for this in that the inflection in the D state potential in this region indicates a fairly rapidly changing electronic structure that could result in an R dependant transition moment. Although we explored a wide variety of steeply rising $\mu_{12}(R)$ functions, which indeed resulted in increased absorption in the 151–153 nm region, we could not reproduce the observed band profile of the D←X absorption near 152 nm. We feel that a considerable amount of enhanced absorption in this region is due to a repulsive state with a moderately strongly allowed transition from the ground state. If this is the case the position and local gradient of the repulsive state can be approximately located, subject to assumptions about $\mu_{12}(R)$. The relevant section of this repulsive state is sketched in the inset to figure 3.15 assuming both D←X and repulsive state ← X transition moments are constant . At smaller R it may begin to predissociate both the ion-pair and nearby Rydberg states and be responsible for the loss in fluorescence noted in section 3.3.2. Comparing the simulated D←X absorption band (figure 3.16) and the observed fluorescence excitation band (figures 3.1 and 3.2), the latter is seen to peak very slightly to the red of the absorption maximum at 154 nm. If the transition moment functions are not rapidly changing across the band, the fluorescence should peak at the position of maximum absorption. However, if the repulsive state under discussion intersects the D state at around 64,000 $cm^{-1}$ (corresponding to $v' \simeq 150$) it may well be that predissociation of higher vibrational levels creates the peak in fluorescence at the observed position.

Forgetting for the moment the persuasive evidence of section 3.3.3 and 3.4.2 regarding our assignment of the ion-pair state of the 148–169 nm absorption system, the $1_u$ state cannot be entirely ruled out by our having found a potential that reproduces most of the observed absorption features and which can be grafted onto the known RKR region of the D state. We merely note that if the observed absorption profile and small vibrational spacing is to be maintained, an ion-pair potential must be used that has a width and inner wall gradient at roughly 10,000 $cm^{-1}$ above $T_e$ similar to those of the potential derived here. If we abandon the RKR points and join the inner and outer

branches at 10,000 $cm^{-1}$ without a point of inflection a potential with a minimum at least 2000 $cm^{-1}$ greater than that of the D or D' states would be created. Table 3.1 indicates that the term values of the $1_u$ and $0_u^+$ states in the lowest ion-pair cluster can only differ by a few hundred $cm^{-1}$. We conclude that the upper state potential does indeed have a point of inflection around 2.2 Å. Such a perturbation has recently been postulated in the $F(0_u^+)$ state of iodine by Hoy and Brand [28].

We can also calculate effective $B_v$ values for the (v'J') levels of $^{79,81}Br_2$, assigned by Venkateswarlu [10], that range smoothly from 2.773 x $10^{-2}$ $cm^{-1}$ at (136,40) to 2.629 x $10^{-2}$ $cm^{-1}$ at (165,36) (Table 3.6). The corresponding $B_v$ values found by Venkateswarlu change erratically from 2.703 x $10^{-2}$ $cm^{-1}$ to 2.730 x $10^{-2}$ $cm^{-1}$ and peak sharply at v'=159 ($T_{0v}$ = 65010 $cm^{-1}$) indicating strong perturbation, probably by a Rydberg state with a characteristically large B value.

### 3.4.2 Dispersed Fluorescence

Calculations show that the $F_2$ laser output i.e. $\lambda_e$ = 157.8 nm and $\Delta\lambda_e$ = 0.05 nm (~20 $cm^{-1}$), corresponds to a near resonance in absorption to v'=136 of the $D(0_u^+)$ state in the $^{81,81}Br_2$ isotopic combination (c.f. table 3.5). It can also be shown that, despite large differences in the $B_v$ values of upper and lower states, the rotational dependence of all three systems analysed was minimal, and simulations were all performed at $J_{max}'$=36 (see equation 2.13).

#### 3.4.2.1 The 280 nm (D-X) System.

The ground state has been analysed by Barrow et al [29]; RKR turning points are given up to v"=36 and $G_v$=10302.1 $cm^{-1}$ (i.e. 64% of $D_e$) spanning 1.9627 Å to 2.9519 Å. The inner repulsive wall was extended by fitting an exponential , $Ae^{-bR}$, to the first two RKR points. Since the D state RKR turning points [4] extend from 2.799 Å to 3.760 Å, the region around the difference potential maximum (figure 3.17) , and hence the simulation of the rainbow (figure 3.10), depends solely on the extrapolation of the X state attractive limb. Consequently this portion of the spectra (263-285 nm) was simulated first.

Having thus extended the ground state to roughly 3.9 Å, its long range behaviour as described by equation 3.8 becomes valid.

Table 3.6

The energy levels and the numbering scheme of reference [10] for the E state.
A comparison of the effective and simulated rotational constants is also given.

| | v' | J' | $T_{ov}/cm^{-1}$ | $10^2 \times B_{eff}/cm^{-1}$ [a] | $10^2 \times B_{eff}/cm^{-1}$ [b] |
|---|---|---|---|---|---|
| E [a] | 165 | 36 | 65358.74 | 2.730 | 2.629 |
| B | 161 | 62 | 65117.01 | 2.796 | 2.622 |
| C | 159 | 44 | 65009.77 | 2.810 | 2.647 |
| $A_{34}$ | 144 | 66 | 64062.97 | 2.627 | 2.666 |
| $A_{12}$ | 143 | 56 | 63996.27 | 2.623 | 2.722 |
| D | 137 | 52 | 63588.40 | 2.690 | 2.765 |
| G | 136 | 40 | 63527.17 | 2.703 | 2.773 |

[a] see ref. [10]

[b] this work

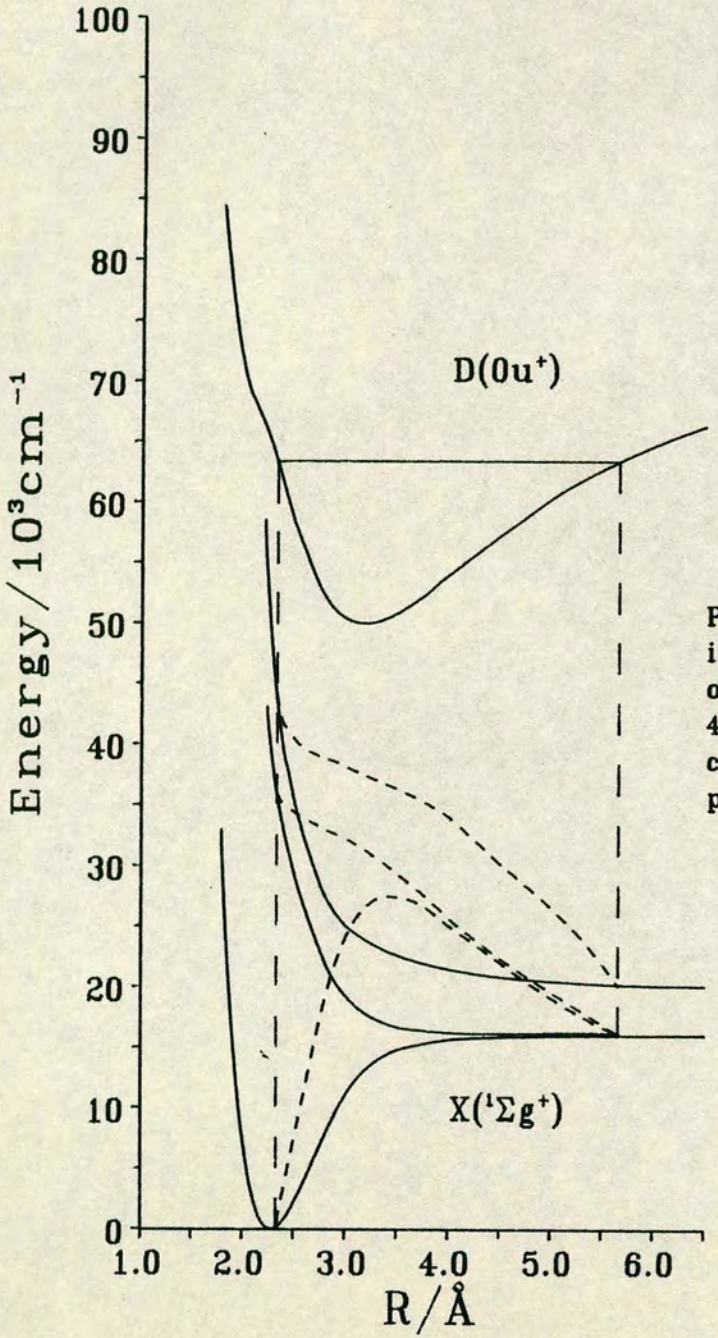


Figure 3.17

**Potential energy curves involved in the three fluorescence systems observed at 280 nm, 360 nm and 440 nm. Also shown are the corresponding difference potentials.**

$$V_x(R) = T_\infty - C5/R^5 - C6/R^6 - C8/R^8 \; ; \; R>3.9 \text{ Å} \qquad (3.8)$$

As indicated by Chang [30] and Brand and Hoy [31], the C5 term for the ground state should be zero. Although Saute et al [32] included it in their calculations of the long range coefficients of $Br_2$ $X(^1\Sigma_g^+)$ and found it to be negligible in comparison with the C6 term: C5 = 0.0033 x $10^5$ $cm^{-1}$ $Å^5$ and C6 = 6.274 x $10^5$ $cm^{-1}$ $Å^6$. The remaining parameter C8 was then adjusted so that equation 3.8 fitted both in value and gradient to our short extrapolation of the RKR points up to 3.9 Å. A successful potential was found with C8 = 1.65 x $10^7$ $cm^{-1}$ $Å^8$; C6/C8 = 0.038 compares with C6/C8 = 0.05 for $I_2$ [33] and C6/C8 = 0.094 for $Cl_2$ [34]. The resulting attractive limb for the ground state is listed at equal intervals of R in table 3.7.

The remainder of the observed spectrum, below 263 nm, was fitted by extending the RKR points of the D state up to roughly 4.4 Å, followed by reflection in our newly constructed ground state until the correct difference potential was formed. Once safely beyond its point of inflection the attractive limb of the D state could be parameterised as a Rittner function, equation 3.4. The inner wall is as described in section 3.4.1.

We consider the reproduction of the fine structure 'phase' in figure 3.10 as further proof that our upper state is essentially correct. The range of R probed by the simulated spectrum was 2.9 Å to 4.4 Å (see figure 3.17).

The observed fluorescence shows a marked fall-off of intensity towards the blue (with the exception of the satellite at 248 nm discussed in section 3.3.3). This could only be accounted for by the transition moment function, $\mu_{12}(R)$, being broadly peaked just to the long bond length side of the minimum of the D state, i.e. around 3.4 Å. Tellinghuisen in his simulation of the McLennan bands of $I_2$ , used a rather broadly peaked function for $\mu_{12}(R)$ centred 0.5 Å beyond $R_e$ of the $D(0_u^+)$ state [23]. Our final transition moment function takes the form

$$\mu_{12}(R) = R^{-2}/(1 + (R - 3.4)^4) \qquad (3.9)$$

We do not attach any particular significance to the functional form of the equation 3.9, it is possible for $\mu_{12}(R)$ to pass through zero for instance, but the position of the maximum can be located to within 0.2 Å. In addition, the exponent of $(R-R_{max})$ in the denominator has to be greater than with $I_2$ (=2) since with $Br_2$ only 4 or 5 peaks of the envelope structure can be observed

Table 3.7

Attractive limb of the ground $X^1\Sigma g^+$ state tabulated between 3.0 and 5.2 Å at equal intervals of 0.1 Å

| R/Å | $E(R)^a/cm^{-1}$ |
|---|---|
| 3.0 | 11008 |
| 3.1 | 12255 |
| 3.2 | 13188 |
| 3.3 | 13880 |
| 3.4 | 14408 |
| 3.5 | 14785 |
| 3.6 | 15026 |
| 3.7 | 15200 |
| 3.8 | 15368 |
| 3.9 | 15526 |
| 4.0 | 15650 |
| 4.1 | 15726 |
| 4.2 | 15772 |
| 4.3 | 15810 |
| 4.4 | 15845 |
| 4.5 | 15875 |
| 4.6 | 15903 |
| 4.7 | 15927 |
| 4.8 | 15947 |
| 4.9 | 15964 |
| 5.0 | 15978 |
| 5.1 | 15989 |
| 5.2 | 15997 |

[a] relative to minimum of potential

covering 5000 $cm^{-1}$, compared with 13500 $cm^{-1}$ in the McLennan bands of $I_2$.

### 3.4.2.2 The 360 nm and 440 nm Systems

Both the observed systems at 360 nm and 440 nm have been assigned as 'single' frequency oscillatory continua emission corresponding to inner turning point fluorescence to a repulsive state with a monotonic difference potential. Assuming the upper state inner wall has been successfully characterised by the analysis in section 3.4.1, $V_1'$ will be reliably known and a plot of $\omega^n - \omega^0$ vs. $\{(n+1/4)^{2/3} - 1/4^{2/3}\}$ (see section 2.4.4) should allow $V_2'$ to be calculated. Plots for each system are displayed in figure 3.18 and yield results summarised below:

360 nm system $V_2' \simeq 31350\ cm^{-1}Å^{-1}$ @ 2.317 Å
440 nm system $V_2' \simeq 29350\ cm^{-1}Å^{-1}$ @ 2.317 Å

The two gradients are very similar, however, the displacement of the two band origins, $\Delta\omega^0$ , by 3500 $cm^{-1}$ indicates that the lower state of the 360 nm system correlates with

$$Br(^2P_{3/2}) + Br(^2P_{3/2})\ (T_\infty = 16056.9\ cm^{-1})$$

and that the lower state of the 440 nm system correlates with

$$Br(^2P_{1/2}) + Br(^2P_{3/2})\ (T_\infty = 19743\ cm^{-1}).$$

The above information was incorporated into two sets of 15 spline points and constituted a useful first approximation to each of the lower states.

Prior to the work described in section 3.3.1 and 3.4.1, initial attempts to analyse these systems involved an unperturbed upper state inner wall. The unusual intensity envelopes i.e. $I(\omega^1)>I(\omega^0)$ and $I(\omega^2) > I(\omega^1) > I(\omega^0)$ for the 360 nm and 440 nm systems respectively, could not be reproduced without a sharply varying transition moment functions with maxima at internuclear separations corresponding to the most intense peak. However, when the perturbed upper state, described in table 3.5, was used, the two systems yielded successful simulations with the lower states listed in table 3.8 (360 nm) and 3.9 (440 nm). These simulations are shown in figures 3.12 and 3.13 and used a constant transition moment. This emphasises that the unusual intensity envelopes are a consequence of Franck–Condon factors and not an artefact of the transition moment function. In addition, since these systems span relatively small internuclear separations, 2.3 Å – 3.2 Å for the 360 nm system

Figure 3.18

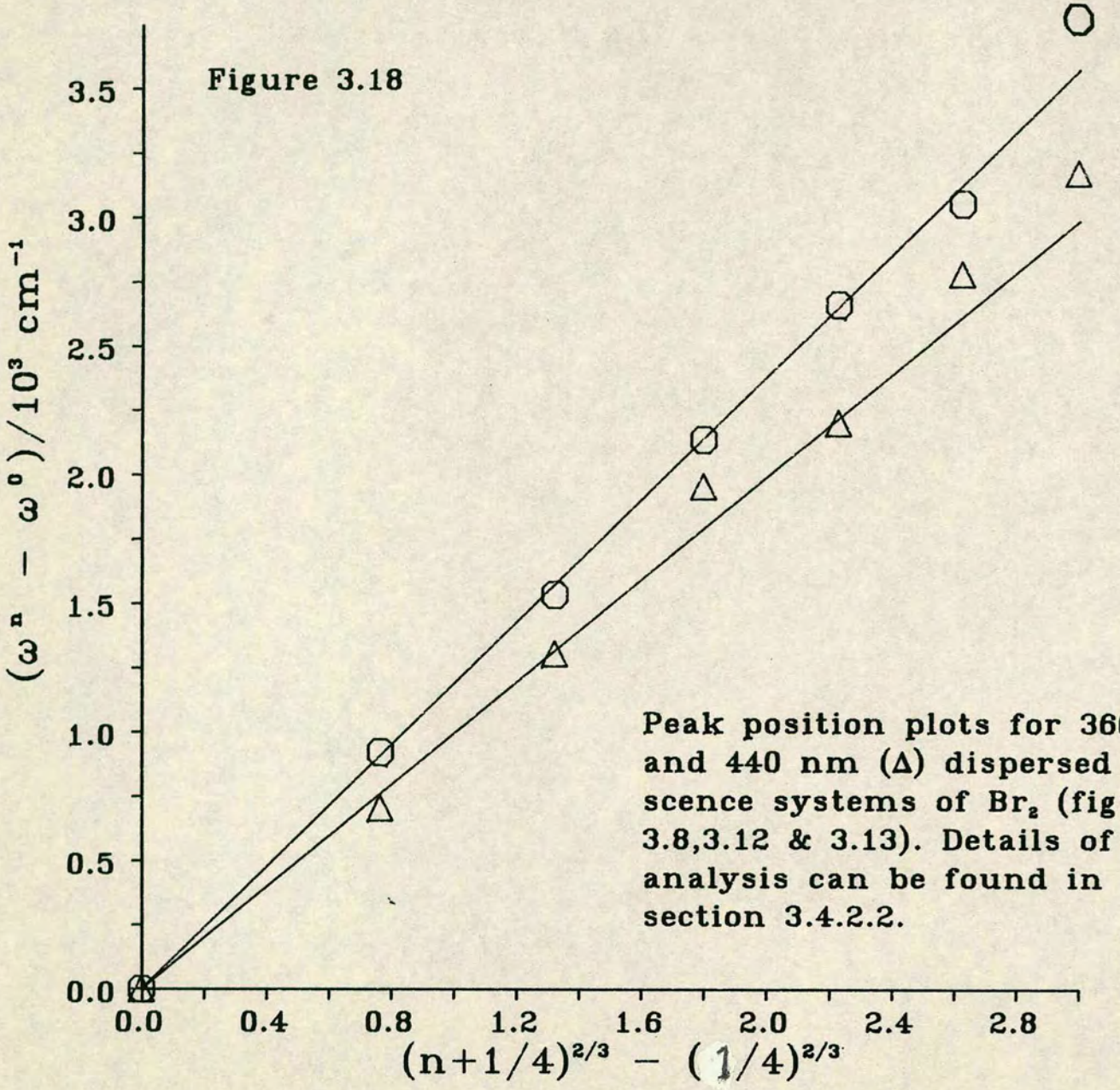


Peak position plots for 360 nm (O) and 440 nm (Δ) dispersed fluorescence systems of $Br_2$ (figs. 3.8,3.12 & 3.13). Details of analysis can be found in section 3.4.2.2.

Table 3.8

Lower repulsive state involved in bound-free 360 nm system.
Dissociation products $Br(^2P_{3/2}) + Br(^2P_{3/2})$; $T_\infty = 16056.9\ cm^{-1}$

| R/Å | $E(R)^a/cm^{-1}$ |
|---|---|
| 2.35 | 18698 |
| 2.40 | 16615 |
| 2.45 | 14819 |
| 2.50 | 13162 |
| 2.55 | 11688 |
| 2.60 | 10387 |
| 2.65 | 9191 |
| 2.70 | 8049 |
| 2.75 | 6933 |
| 2.80 | 5882 |
| 2.85 | 4983 |
| 2.90 | 4252 |
| 2.95 | 3650 |
| 3.00 | 3136 |
| 3.05 | 2672 |
| 3.10 | 2251 |
| 3.15 | 1897 |
| 3.20 | 1611 |

[a] relative to dissociation

Table 3.9

Lower repulsive state involved in bound-free 440 nm system.
Dissociation products $Br(^2P_{3/2}) + Br(^2P_{1/2})$; $T_\infty = 19743\ cm^{-1}$

| R/Å | $E(R)^a/cm^{-1}$ |
|---|---|
| 2.35 | 22428 |
| 2.40 | 19377 |
| 2.45 | 17538 |
| 2.50 | 15482 |
| 2.55 | 13807 |
| 2.60 | 12331 |
| 2.65 | 11040 |
| 2.70 | 9784 |
| 2.75 | 8670 |
| 2.80 | 7673 |
| 2.85 | 6954 |
| 2.90 | 6273 |
| 2.95 | 5772 |
| 3.00 | 5233 |
| 3.05 | 4852 |
| 3.10 | 4550 |
| 3.15 | 4272 |
| 3.20 | 4014 |
| 3.25 | 3775 |
| 3.30 | 3552 |
| 3.35 | 3347 |
| 3.40 | 3156 |
| 3.45 | 2980 |
| 3.50 | 2816 |
| 3.55 | 2665 |
| 3.60 | 2525 |

[a] relative to dissociation

and 2.3 Å - 3.6 Å for the 440 nm, a simple exponentialy decaying transition moment would adequately reproduce the observed intensity decay to the blue.

From comparison with $I_2$ spectroscopy [42], we can tentatively assign the 360 nm lower state (table 3.8) to be the analogue of the $a'(0_g^+)$ state of $I_2$. The second lower state at 440 nm (table 3.9) dissociates to $Br(^2P_{3/2}) + Br(^2P_{1/2})$. The $\Delta\Omega=0$ rule for ion-pair $\leftrightarrow$ valence transitions suggests to us that the 440 nm state has $\Omega=0$, '+' parity and gerade symmetry i.e. it is the $0_g^+$ state correlating with the above dissociation products [32]. All potentials involved in the above fluorescence systems and the accompanying difference potentials are illustrated in figure 3.17.

## 3.5 Discussion

The $D(0_u^+)$ ion-pair state is identified as the upper state responsible for the discrete absorption between 148 nm and 169 nm. Detailed fitting of the partially resolved vibrational structure indicates a point of inflection in the inner wall of the D state roughly 15,000 $cm^{-1}$ above $T_e$. This is presumably due to an avoided crossing with a Rydberg state, the molecular motion being slow enough for the adiabatic potentials to be followed, but still causing a rather severe perturbation of the rotational levels observed by Venkateswarlu [10]. A D state potential is presented that accounts for the previously observed low lying vibrational levels (v = 0-16) [4], the present band of levels (v' = 133-173) and a handful of rotationally resolved around v'=136 observed by Venkateswarlu [10].

The common upper state involved in the three observed fluorescence systems excited at 157.8 nm is identified as v' = 136 of the $^{81,81}Br_2$ isotopic species. The information in the 280 nm 'McLennan' type system fixes the upper state around the difference potential maximum i.e. 3.4 Å. Outward extrapolation of the D state RKR analysis [4] is well characterised by the Rittner function and probably accurate.

The 360 nm and 440 nm systems involve transitions from the proposed perturbed inner wall. Successful simulations involving well behaved repulsive lower states reinforces our interpretation of the absorption spectra.

With the 280 nm system a broadly peaked transition moment function was

needed to reproduce the fluorescence decay to the blue. This has proven to be a common feature of fluorescence from high vibronic states where the electron configuration (or valence bond character) can change rapidly especially near an avoided crossing.

The fluorescence excitation spectrum indicates rapid predissociation of most of the Rydberg states and near resonant ion-pair vibrational levels of appropriate symmetry; the lower ion-pair vibrational levels (as noted above) fluoresce strongly. To characterise this predissociation and to fully understand the nature of the proposed Rydberg/ion-pair perturbation, single isotope high resolution ( < 0.005 nm) absorption studies in the 151-153 nm region are planned.

## References


1. T. Ishiwata, A. Tokunaga, T. Shinzawa and I. Tanaka, Bull. Chem. Soc. Japan, 57, 1469 (1984)
2. T. Ishiwata, T. Shinzawa, A. Tokunaga and I. Tanaka, Chem. Phys. Letts., 101, 350 (1983)
3. T. Ishiwata, H. Ohtoshi and I. Tanaka, J. Chem. Phys., 81, 2300 (1984)
4. T. Ishiwata, A. Tokunaga, T. Shinzawa and I. Tanaka, J. Mol. Spectrosc., 108, 314 (1984)
5. T. Ishiwata, A. Tokunaga, T. Shinzawa and I. Tanaka, Bull. Chem. Soc. Japan,57, 1317 (1984)
6. P. Berwanger, K.S. Viswanathan and J. Tellingjuisen, J. Mol. Spectrosc., 91, 275 (1982)
7. A. Sur and J. Tellinghuisen, J. Mol. Spectrosc., 88, 323 (1981)
8. P.Venkateswarlu, Canad. J. Phys., 47, 2525 (1969)
9. M. MacDonald, R.J. Donovan and M.C. Gower, Chem. Phys. Letts., 97, 72 (1983)
10. P. Venkateswarlu, V.N. Sarma and Y.V. Rao, J. Mol. Spectrosc., 96, 247 (1982)
11. R.J. Donovan, G. Gilbert, M. MacDonald, J.P.T. Wilkinson, I. Munro and D. Shaw, J. Photochem., 31, 1 (1985)
12. D. Austin, R.J. Donovan, A. Hopkirk, K.P. Lawley, D. Shaw and A.J. Yencha, Chem. Phys., accepted for publication (1987)
13. E. Kerr, M.A. MacDonald, R.J. Donovan and J.P.T. Wilkinson, J. Photochem., 31, 149 (1985)
14. M.A. MacDonald, Ph.D. Thesis, Edinburgh University, 1984, pp.37–42
15. R.J. Donovan, B.V. O'Grady, K. Shobatake and A. Hiraya, Chem. Phys. Letts., 122, 612 (1985)
16. M. Martin, C. Fotakis, R.J. Donovan and M.J. Shaw, Nuovo Cimento 63B, 300 (1981)
17. H. Pummer, K. Hohla, M. Diegalmann and J.P. Reilly, Opt. Commun., 28, 104 (1979)
18. W. Demtröder, Springer Series in Chem. Phys., 5 Laser Spec., p222 (1982)
19. M.I.T. Wavelengths Tables, Wiley & Sons Inc., New York.
20. B.K. Clark and I.M. Littlewood, Chem. Physics, 107, 97 (1986)
21. P.B.V. Haranath and P.T. Rao, J. Mol. Spectrosc., 2, 428 (1958)
22. R.S. Mulliken, J. Chem. Phys., 55, 288 (1971)
23. J.B. Tellinghuisen, Canad. J. Phys., 62(2), 1933 (1984)
24. K.P. Lawley, M.A. MacDonald A. Kvaran and R.J. Donovan, Chem. Phys. Letts., 92, 322 (1982)
25. M.A. MacDonald, Ph.D. Thesis, Edinburgh University 1984, p.102
26. J. Tellinghuisen, Chem. Phys. Letts., 29 359 (1974)
27. J.N. Wilson and R.M. Curtis, J. Phys. Chem., 74, 187, (1970)
28. A.R. Hoy and J.C.D. Brand, Chem. Physics, 109, 109 (1986)
29. R.F Barrow, T.C. Clark, J.A. Coxon and K.Yee, J. Mol. Spectrosc., 51, 428 (1974)
30. T.Y. Chang, Rev. Mod. Phys., 39, 911 (1967)
31. J.C. Brand and A.R. Hoy, J. Mol. Spectrosc., 114, 197 (1985)
32. M. Saute, B. Bussery and M. Aubert-Frecon, Mol. Phys., 51, 1459 (1986)
33. F. Martin, S. Churassy, R. Bacis, R.W. Field and J. Verges, J. Chem. Phys., 79, 3725 (1983)
34. A.E. Douglas and A.R. Hoy, Canad. J. Phys., 53, 1965 (1975)
35. T. Shinzawa, A. Tokunaga, T. Ishiwata, I. Tanaka, K. Kasatani, M. Kawasaki and H. Sato, J. Chem. Phys., 80, 5909 (1984)

36. T. Ishiwata, K. Obi and I. Tanaka, to be published.
37. A.R. Hoy, J. Mol. Spectrosc., 115, 232 (1986)
38. J.C.D. Brand, V.D. Deshpande, A.R. Hoy and S.M. Jaywant, J. Mol. Spectrosc., 100, 143 (1983)
39. J.C.D. Brand, A.R. Hoy, S.M. Jaywant and A.W. Taylor, J. Mol. Spectrosc., 123, 84 (1987)
40. T. Ishiwata, T. Hara, K. Obi and I. Tanaka, J. Chem. Phys., 87, 2513, (1987)
41. J.A. Coxon, J. Mol. Spectrosc., 41, 548 (1972)
42. S. Churassy, F. Martin and R. Bacis, J. Chem. Phys., 75, 4863 (1981)

# CHAPTER 4
# IODINE MONOBROMIDE

## 4.1 Introduction

The absorption spectrum of IBr between 124 nm and 200 nm is shown in figure 4.1. It has the characteristic appearance of several sharp Rydberg vibrational progressions superimposed on broad vibrationally unresolved ion-pair absorption systems. Although the absorption spectrum of IBr, above 154 nm, has been reported previously [1,2], the present work extends observations down to 124 nm and data on the relative absorption cross section are presented for the first time.

We will be concerned with the ion-pair absorption system around 165 nm; this state will later be identified as the $E(0^+)$ state of the first ion-pair cluster. Previous work has shown that this, and other, halogen ion-pair states give rise to highly structured oscillatory continuum emission in the near ultraviolet (UV) following excitation in the vacuum and far ultraviolet (VUV) [3-6].

By monitoring the fluorescence excitation spectrum in the near UV, the VUV fluorescence associated with the strong Rydberg absorptions is in effect 'filtered' out, leaving mostly ion-pair fluorescence. This yielded valuable information on predissociations and interactions between the higher excited states.

We also report analysis of dispersed fluorescence from high in the vibrational manifold of the $E(0^+)$ state ($110 < v' < 205$). This was excited in three different ways: (i) with synchrotron radiation in the 169 nm and 180 nm regions; (ii) by the ArF laser line at 193 nm; (iii) using a Perkin-Elmer spectrofluorimeter at 200 nm. The fluorescence typically ranges from 300 nm to 390 nm and will be shown to end in the ground state. This corresponds to transitions at internuclear separations between 3.1 Å and 4.8 Å, a region well characterised in the upper state but not well known in the ground state. Previous studies, [5,6] have shown that a unique fit can be obtained if either the upper or lower state is well defined over most of the vibrational displacement responsible for the emission.

## 4.2 Experimental

### 4.2.1 The SRS

The absorption , fluorescence excitation and some of the dispersed fluorescence work (i.e. figures 4.1-5), were all performed using the Synchrotron Radiation Source (SRS) at the SERC Daresbury Laboratory. The experimental details are well documented elsewhere [5,7,8], however, some of the salient features are discussed in section 3.2.1. Although the SRS is a tunable radiation source in the VUV, the relatively low intensity of the monochromated output limits its use to regions of relatively strong absorption i.e. $\lambda < 180$ nm.

Absorption and fluorescence excitation spectra were collected simultaneously. Corrections for changes in synchrotron light intensity and the spectral response of the Seya excitation monochromator have been incorporated in the presented spectra (figures 4.1 and 4.2). The Seya excitation monochromator was initially calibrated by setting the wavelength indicator to zero at the maximum of zero order light. Further calibration checks were made across the Schumann-Runge bands of $O_2$, and final accuracy confirmed by comparison with the known Rydberg absorptions of $Br_2$ between 130 nm and 157 nm [9].

The dispersed fluorescence was calibrated against known emission lines from atomic iodine produced by excitation of $I_2$ at short wavelengths [10]. The combined response function for the fluorescence monochromator and photomultiplier was flat, to within 10%, over the region 300 to 370 nm and thus corrections to the observed spectra are unnecessary.

### 4.2.2 The ArF Laser

The experimental set-up for exciting IBr using an ArF laser ($\lambda$ = 193 nm) has been described previously [3]. The present work was performed at the SERC Rutherford and Appleton Laboratory's Ultraviolet Radiation Facility. A line narrowed ArF laser and a monochromator (Jobin-Yvon HRS2) of somewhat higher resolution (0.3 nm) were used [8]. The high intensity (see below) of the ArF laser greatly facilitates observation of the relatively weak fluorescence from IBr, but the fixed excitation frequency clearly limits the data that can be obtained.

As used, the laser delivered a pulse energy of 10 mJ lasting 20 ns. The output was tunable across the normal gain profile of an ArF laser (192.8 - 193.6 nm) giving a narrow line of less that 10 $cm^{-1}$ bandwidth. The spectral output consists of two contributions, intense line narrowed laser radiation and broader weak amplified spontaneous emission (ASE). Although the line narrowed laser line was 100 times more intense than the background ASE the wavelength integrated intensities of the two components were much more comparable.

The signal was detected and stored using an optical multichannel analyser (Princeton Applied Research EG&G OMA II) with a silicon diode array head [11]. Digitisation of the spectrum allowed background correction and calibration was against known atomic resonances from Mercury and Argon [12].

### 4.2.3 The Spectrofluorimeter

To overcome the intensity problems associated with the use of synchrotron radiation and the limitations of the fixed frequency ArF laser, a standard Perkin-Elmer 650-40 spectrofluorimeter was used to record spectra at 200 nm [13]. For further details the reader is referred to the manufacturers specification list and reference [8].

## 4.3 Observations

### 4.3.1 The VUV Absorption Spectrum

The single photon absorption spectrum of IBr between 124 nm and 200 nm is shown in figure 4.1. A pressure ratio of 2:1 of $Br_2$ to IBr ensured that equilibrium was established with negligible $I_2$ present. It is known that $Br_2$ absorption and fluorescence excitation are confined below 161 nm thus all the structure to the red may be attributed to IBr. Further careful work should allow the subtraction of the spectrum due to $Br_2$ (see figure 3.1), but this has not been possible here.

Between 160 nm and 200 nm the absorption spectrum of IBr exhibits two types of structure (figure 4.2); (i) an underlying, extensive, quasi-continuous, band system between roughly 165 nm and 185 nm: (ii) Three sharp and intense systems with a local vibrational spacing of 270 $cm^{-1}$ each under a Gaussian envelope.

Figure 4.1

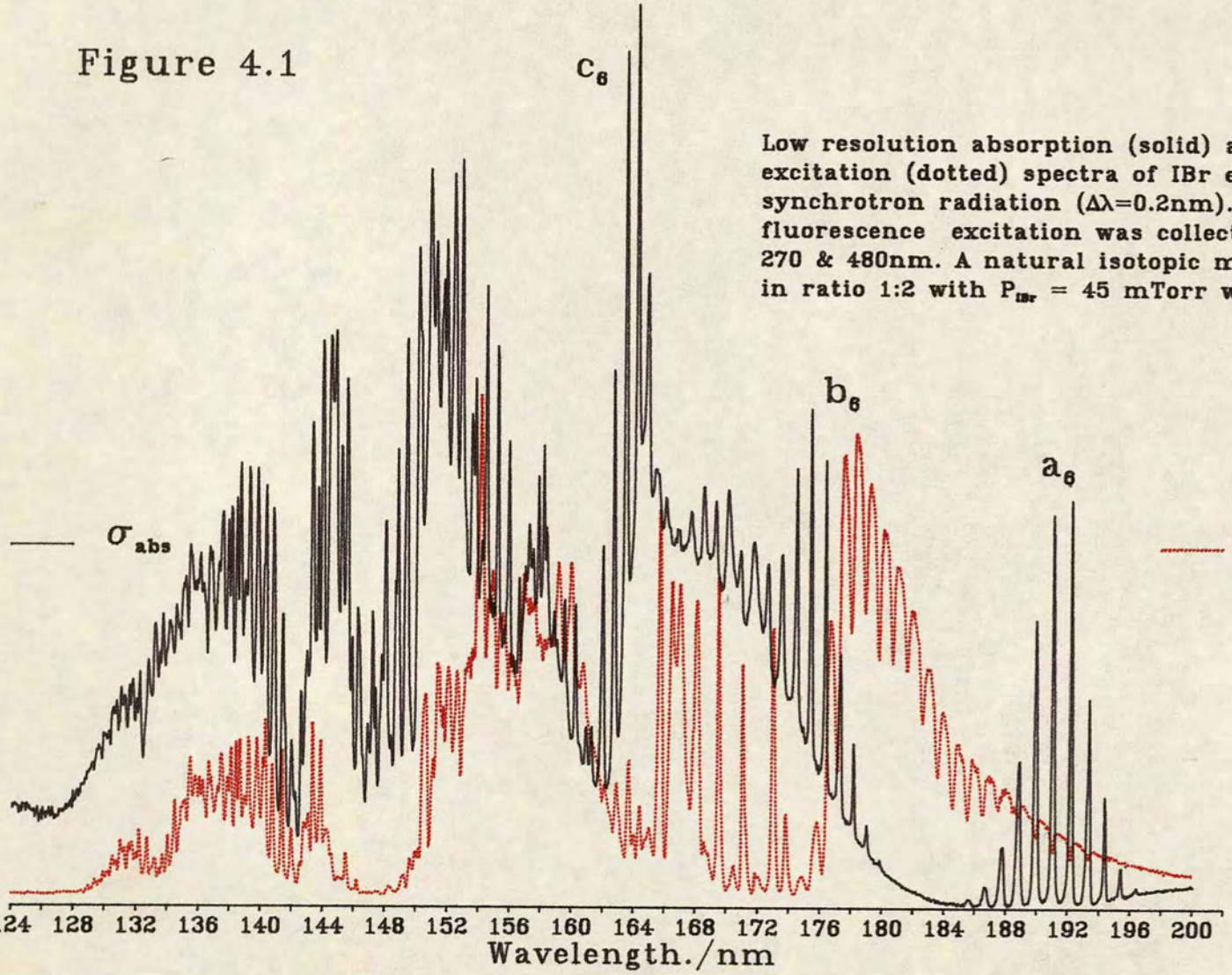


Low resolution absorption (solid) and fluorescence excitation (dotted) spectra of IBr excited by synchrotron radiation ($\Delta\lambda$=0.2nm). The fluorescence excitation was collected between 270 & 480nm. A natural isotopic mix of IBr/$Br_2$ in ratio 1:2 with $P_{tot}$ = 45 mTorr was used.

Figure 4.2

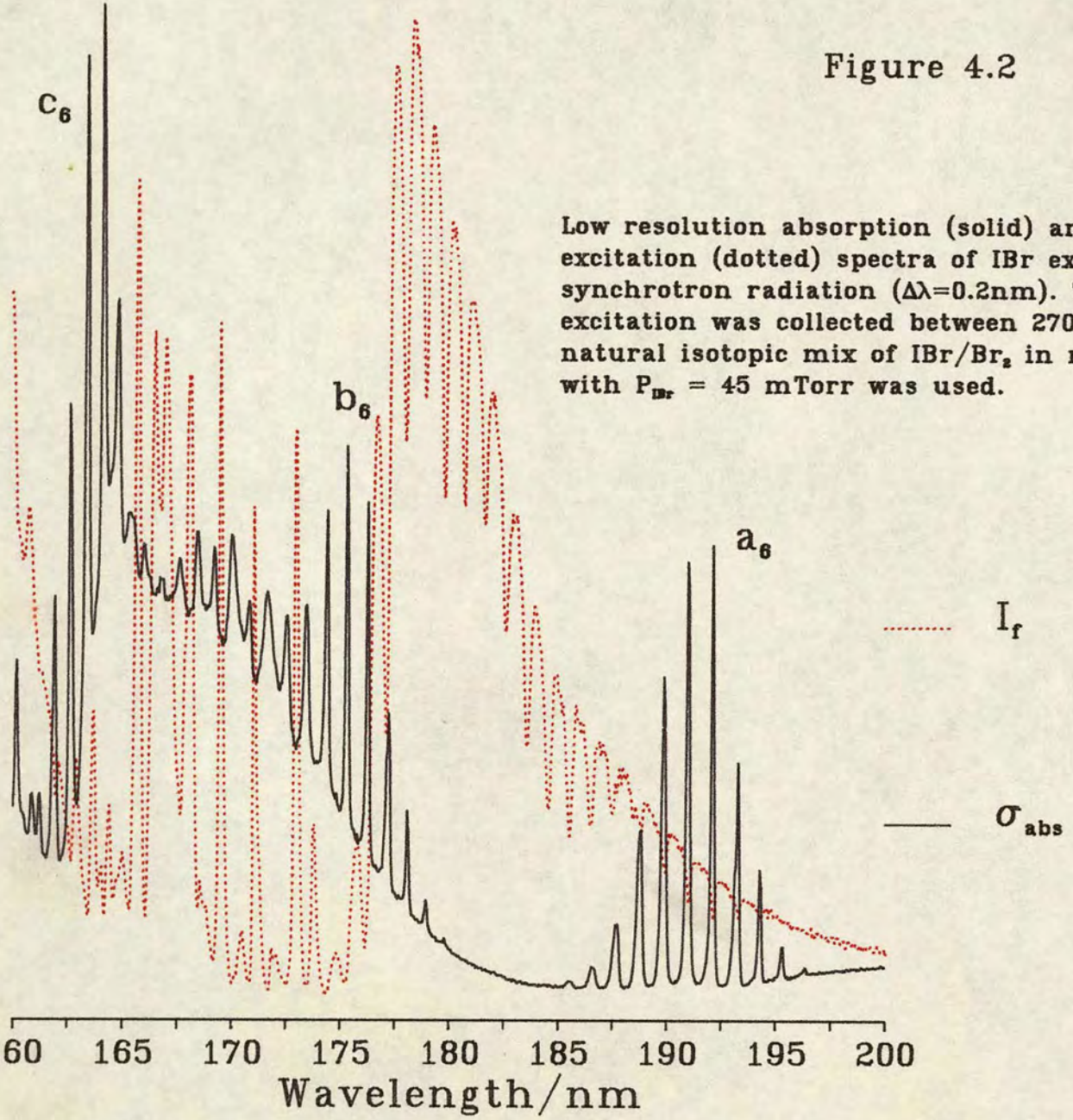


Low resolution absorption (solid) and fluorescence excitation (dotted) spectra of IBr excited by synchrotron radiation ($\Delta\lambda$=0.2nm). The fluorescence excitation was collected between 270 & 480nm. A natural isotopic mix of IBr/$Br_2$ in ratio 1:2 with $P_{IBr}$ = 45 mTorr was used.

The former is characteristic of absorption to high on the inner wall of a broad diffuse ion-pair state (see table 4.1). It is known that $\Delta\Omega = 0$ transitions are strongly favoured in absorption from the ground state [19,35], making the E and f states strong candidates. Furthermore, the absence of any analogous absorption to the red suggests that, as in $Br_2$ (see section 3.3.1) and ICl (see section 5.3.1), we are accessing the first ion-pair cluster. We therefore assign the ion-pair state as the $E(0^+)$.

We know that the large increase in bond length of the ion-pair absorption will lead to an extended rotational contour (section 2.3) and medium to high resolution is required to resolve any ion-pair structure. Furthermore, in contrast to $Br_2$ and ICl no single isotope combination dominates the natural mix; both $I^{79}Br$ and $I^{81}Br$ were present in equal amounts. This probably explains why no vibrational structure was resolved across the entire ion-pair absorption band. Pure isotope studies at higher resolution are planned allowing a similar analysis to that of section 3.4.1 with $Br_2$. The gradual increase in the base line at $\lambda > 185$ nm is due to scattered light from the synchrotron passing through the sodium salicylate fluorescence bandpass filter used to monitor transmitted light.

The wider spaced structure ((ii) above) are transitions to low lying levels of the Rydberg states and have been previously reported [1,2]. A comparison of figures 4.2 and 5.2 suggested we abandon the nomenclature proposed originally by Cordes and Sponer [14] in favour of that established for ICl by Venkateswarlu [15]. The $IBr^+$ cores for the Rydberg states involved in these absorptions are (2430):$^2\Pi_{3/2}$ and $^2\Pi_{1/2}$ [16]; their (the cores) coupling to the Rydberg electron is of $\Omega$-$\omega$ type. Consequently the $(^2\Pi_{3/2})\sigma$ configuration gives rise to $\Pi_2$ and $\Pi_1$ electronic states and the $(^2\Pi_{1/2})\sigma$ configuration to $\Pi_{0^-}$, $\Pi_{0^+}$ and $\Pi_1$ electronic states [16]. The ground state of IBr has the electron configuration (2440):$^1\Sigma^+$ [16]. The allowed transitions are:

$$0^+ \leftrightarrow 0^+ \qquad 0^+ \not\leftrightarrow 0^- \qquad 0^+ \leftrightarrow 1$$

with those involving $\Delta\Omega = 2$ much weaker than those for which $\Delta\Omega = 0$ or 1. The configuration assignments in column 1 of table 4.2 are based on the above discussion (see also reference [15]).

The hot bands of a Rydberg series are separated by an $\omega_e''$ characteristic of the ground state. In contrast, transitions from $v'=0$ of the ground state have a

Table 4.1

Spectroscopic constants for valence and ion-pair states of IBr

| State | $J_{Br}$ [a] | $J_I$ | $T_e/cm^{-1}$ | $\omega_e/cm^{-1}$ | $\omega_e X_e/cm^{-1}$ | $r_e/\AA$ | $T_\infty/cm^{-1}$ | Ref. |
|---|---|---|---|---|---|---|---|---|
| G (1) | 0 | 1 | 45996.0 | 128.5 | 0.319 | 3.363 | 79096.0 | 34 |
| f ($0^+$) | 0 | 0 | 45382.6 | 128.8 | 0.363 | 3.394 | 78462.6 | 20 |
| β (1) | 0 | 2 | 39507.8 | 122.1 | 0.255 | 3.434 | 71987.8 | 21 |
| E ($0^+$) | 0 | 2 | 39487.8 | 119.4 | 0.206 | 3.407 | 71987.8 | 20, 21 |
| D'(2) | 0 | 2 | 38306 (38714) | 154 | - | 3.105 | 71987.8 | 33 |
| B'($^3\pi_0$) | 3/2 | 3/2 | 17053 | 123 | 4.4 | 3.275 | 14664.9 | 32 |
| B($^3\pi_0$) | 3/2 | 1/2 | 16165 | 142 | 2.6 | 2.83 | 18490 | 30,22 |
| A($^3\pi_1$) | 3/2 | 3/2 | 12360.73 | 136.61 | 1.623 | - | 14664.9 | 31 |
| X($^1\Sigma^+$) | 3/2 | 3/2 | 0 | 268.71 | 0.828 | 2.4699 | 14664.9 | 22, 30 |

[a] The J states of the atomic or ionic products that correlate diabatically with the molecular state are given

Table 4.2

IBr Rydberg absorption in the V.U.V.[a)]

| System | v',v" | λvac/nm | $\bar{\nu}$/cm$^{-1}$ | Δν/cm$^{-1}$ |
|---|---|---|---|---|
| $a_6$ | 0,3 | 196.45 | 50904 | |
| ($C^{b)}$) | 0,2 | 195.45 | 51164 | 260 |
| | 0,1 | 194.40 | 51440 | 276 |
| | 0,0 | 193.40 | 51706 | 266 |
| | 1,0 | 192.25 | 52016 | 310 |
| $(^2\pi_{3/2})6s\sigma,\pi_1$ | 2,0 | 191.10 | 52329 | 313 |
| | 3,0 | 190.00 | 52632 | 303 |
| | 4,0 | 188.95 | 52924 | 292 |
| | 5,0 | 187.75 | 53262 | 338 |
| | 6,0 | 186.65 | 53576 | 314 |
| | 7,0 | 185.60 | 53879 | 303 |
| $b_6$ | 0,3 | 179.90 | 55586 | |
| ($D^{b)}$) | 0,2 | 179.05 | 55850 | 264 |
| | 0,1 | 178.25 | 56117 | 267 |
| | 0,0 | 177.35 | 56386 | 269 |
| | 1,0 | 176.40 | 56689 | 303 |
| $(^2\pi_{1/2})6s\sigma,\pi_{0+,1}$ | 2,0 | 175.45 | 56996 | 307 |
| | 3,0 | 174.55 | 57290 | 294 |
| | 4,0 | 173.60 | 57604 | 314 |
| | 5,0 | 172.70 | 57904 | 300 |
| $c_6$ | 0,2 | 164.95 | 60624 | |
| ($E^{b)}$) | 0,1 | 164.25 | 60883 | 259 |
| | 0,0 | 163.55 | 61143 | 260 |
| | 1,0 | 162.75 | 61444 | 301 |
| $(^2\pi_{3/2})6p\sigma,\pi_1$ | 2,0 | 162.05 | 61709 | 265 |

a) estimated error $\Delta\lambda = \pm 0.1$ nm

b) momenclature ref. [ 2 ]

spacing, $\omega_e'$, characteristic of the excited Rydberg state. In general $\omega_e' > \omega_e''$ (see column 5 table 4.2). We identified the resonance immediately to the red of the discontinuity in $\Delta\nu$ as the (0,0) band. Our assignment (column 2 of table 4.2) reinforces Donovan and Robertson's assignment of the $a_6(0,0)$ and $b_6(0,0)$ band origins [2], however we propose a reassignment of the $c_6(0,0)$ transition.

We attempt no assignment of the complex 'Rydberg type' structure overlying the ion-pair absorption between the $b_6$ and $c_6$ Rydberg systems i.e. 164 to 172 nm. We do note however that these peaks in absorption have a striking correlation to troughs in fluorescence excitation. This may suggest an ion-pair/Rydberg interaction where the Rydberg is either strongly predissociated or fluoresces in the VUV. A full discussion of all the points described in this section may be found in reference [17].

The Rydberg transitions of IBr analysed by Donovan and Robertson [2], and the transitions of $Br_2$ analysed by Venkateswarlu [9] provided useful calibration checks on the other methods described in section 4.2.

### 4.3.2 The Fluorescence Excitation Spectrum

The fluorescence excitation spectrum with all light between 270 nm and 480 nm collected, is shown in figure 4.1. We concentrate our discussion on the $Br_2$ free region above 161 nm (figure 4.2). The broad peak between 175 nm and 200 nm comes from the ion-pair state and is punctuated by sharp dips with characteristic Rydberg spacing. There is a sharp cut-off in fluorescence intensity at 175 nm well before the maximum in ion-pair absorption at roughly 166 nm. The sharp resonances to the blue of 175 nm have a peculiar intensity distribution and correspond to ion-pair fluorescence at troughs in Rydberg type absorption (see section 4.3.1 and 4.3.3). Two factors make the Rydbergs invisible in fluorescence collected in the near UV: (i) many such states are predissociated (e.g. the $a_6$ [18]); (ii) the most intense emission would be to bound regions of the ground state and lie in the VUV.

The small dips observed between 187 nm and 197 nm reflect the strength of the corresponding $a_6$ Rydberg absorption and exhibit a pressure dependence. They are clearly due to strong Rydberg absorption by the sample i.e. a reversal effect due to the optical depth of the sample. The troughs between 188 nm and 179 nm have an entirely different origin. These 'resonances' exhibit a

Rydberg type vibrational spacing but have no absorption counterparts. As discussed in section 4.3.1, Ω–ω type coupling between the $IBr^+$ ($^2\Pi_{3/2}$) core and a σ Rydberg electron produces two close lying electronic states; $\Pi_1$ and $\Pi_2$ [16]. Selection rules forbid direct transition to the $\Pi_2$ component and it is not seen in absorption. However, where the blue wing of the $a_6(\Pi_1)$ Rydberg self absorption overlaps the onset of these "resonances" i.e. 189 nm, close study reveals a discontinuity in the vibrational progression between the two processes. We feel this may indicate that two different electronic states are involved in each phenomena. We propose that the E($0^+$) ion–pair state crosses the outer wall of the $\Pi_2$ state at roughly v=4 and that a heterogeneous coupling, perhaps through another Ω=1 ion–pair state, allows the E state to act as a 'doorway' to the Rydberg state which is invisible in absorption and is either predissociated or fluoresces in the VUV.

Similarly, Ω–ω type coupling predicts two close lying accessible electronic states, $\Pi_{0+}$ and $\Pi_1$, arising from the ($^2\Pi_{1/2}$)σ configuration [16]. We suggest it is no coincidence that the ion–pair fluorescence excitation collapses around the $b_6(0,0)$ band, which must necessarily lie very close to the term value of the associated $\Pi_{0+}$ Rydberg state. A homogeneous coupling between the E($0^+$) and $\Pi_{0+}$ states, resulting in an avoided crossing , would shift the inner wall of the E state to shorter bond length. If this was into the path of a steeply rising predissociating repulsive state, it would have a profound effect on the fluorescence excitation profile.

Single isotope, high resolution studies are planned in this spectral region in an attempt to fully rationalise the observed features. Low pressure work of this type would also help analyse the peak–in–absorption, trough–in–fluorescence correlation found between 165 nm and 175 nm. As with section 4.3.1 a full discussion of all the features described in this section may be found in ref [17].

### 4.3.3 Dispersed Fluorescence Spectra

Low resolution fluorescence spectra were recorded at 169 nm and 180 nm using synchrotron radiation, and at 193 nm and 200 nm using an ArF laser and a spectrofluorimeter respectively (see figures 4.3–4.7). By comparison with the analogous $I_2$ systems MacDonald et al [3] suggested two oscillatory continuum systems. The first is associated with a repulsive lower state and the second

Figure 4.3

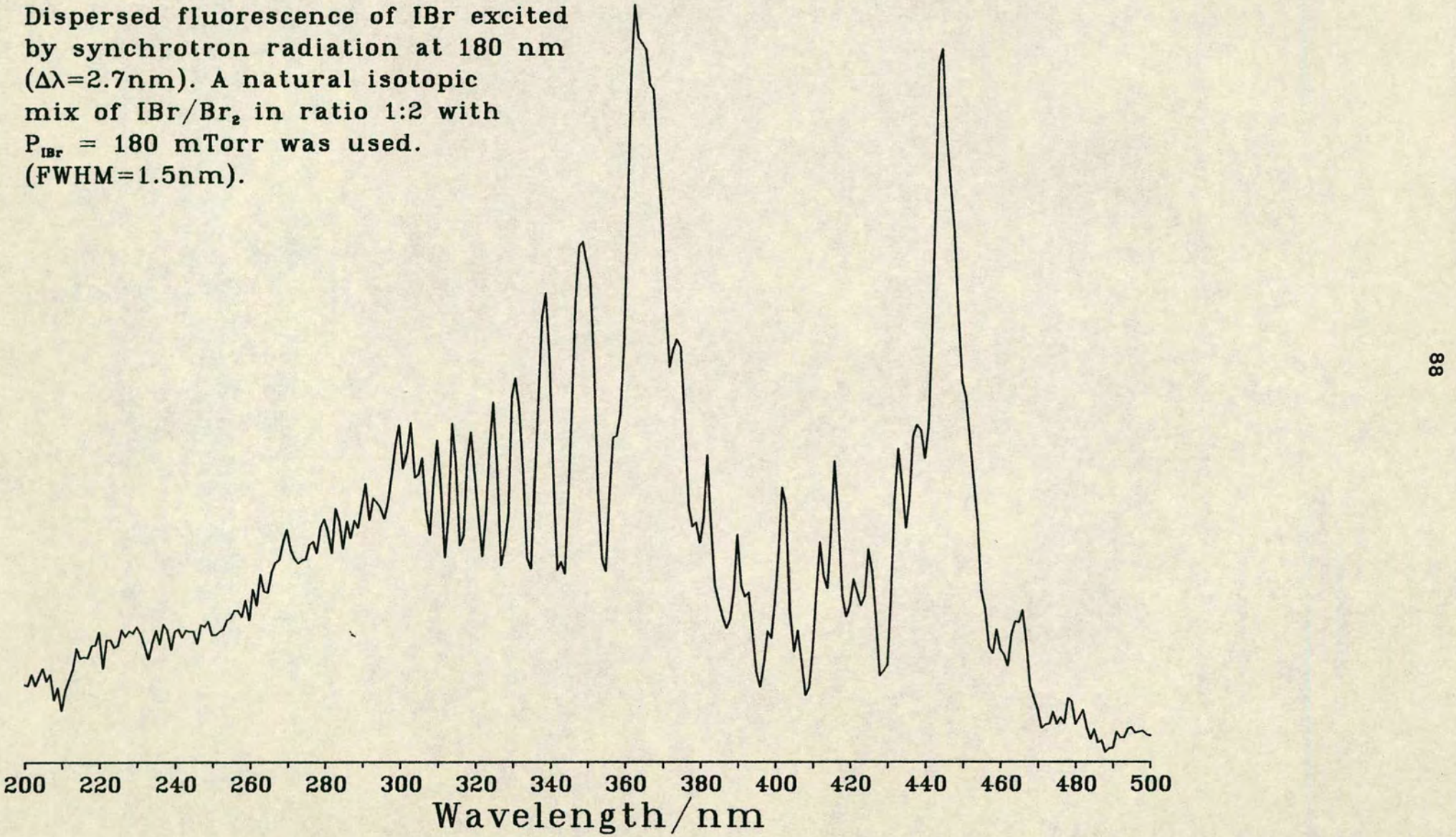
Dispersed fluorescence of IBr excited by synchrotron radiation at 180 nm (Δλ=2.7nm). A natural isotopic mix of IBr/Br2 in ratio 1:2 with P_IBr = 180 mTorr was used. (FWHM=1.5nm).
200
220
240
260
280
300
320
340
360
380
400
420
440
460
480
500
Wavelength/nm

Figure 4.4

Dispersed fluorescence of IBr excited by synchrotron radiation at 169 nm ($\Delta\lambda$=2.2nm). A natural isotopic mix of IBr/$Br_2$ in ratio 1:2 with $P_{Br}$ = 170 mTorr was used. (FWHM=3.0nm).

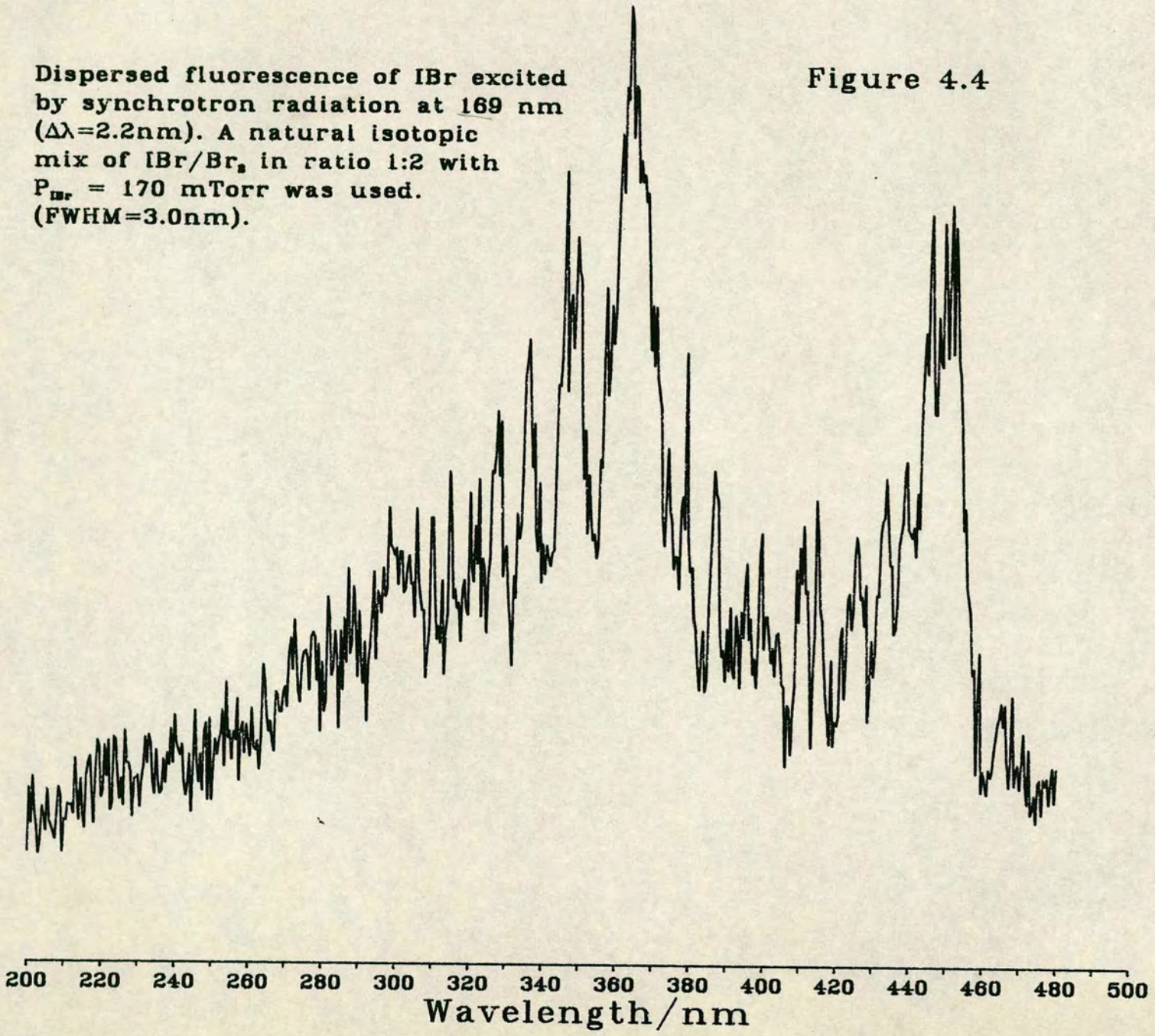

Figure 4.5

Observed and simulated dispersed fluorescence from IBr excited by synchrotron radiation at 180nm ($\Delta\lambda$=1.8nm). A natural isotopic mix of $IBr/Br_2$ in ratio 1:2 with $P_{IBr}$ = 175 mTorr was used. (FWHM=1.5nm). For simulation details see section 4.4.

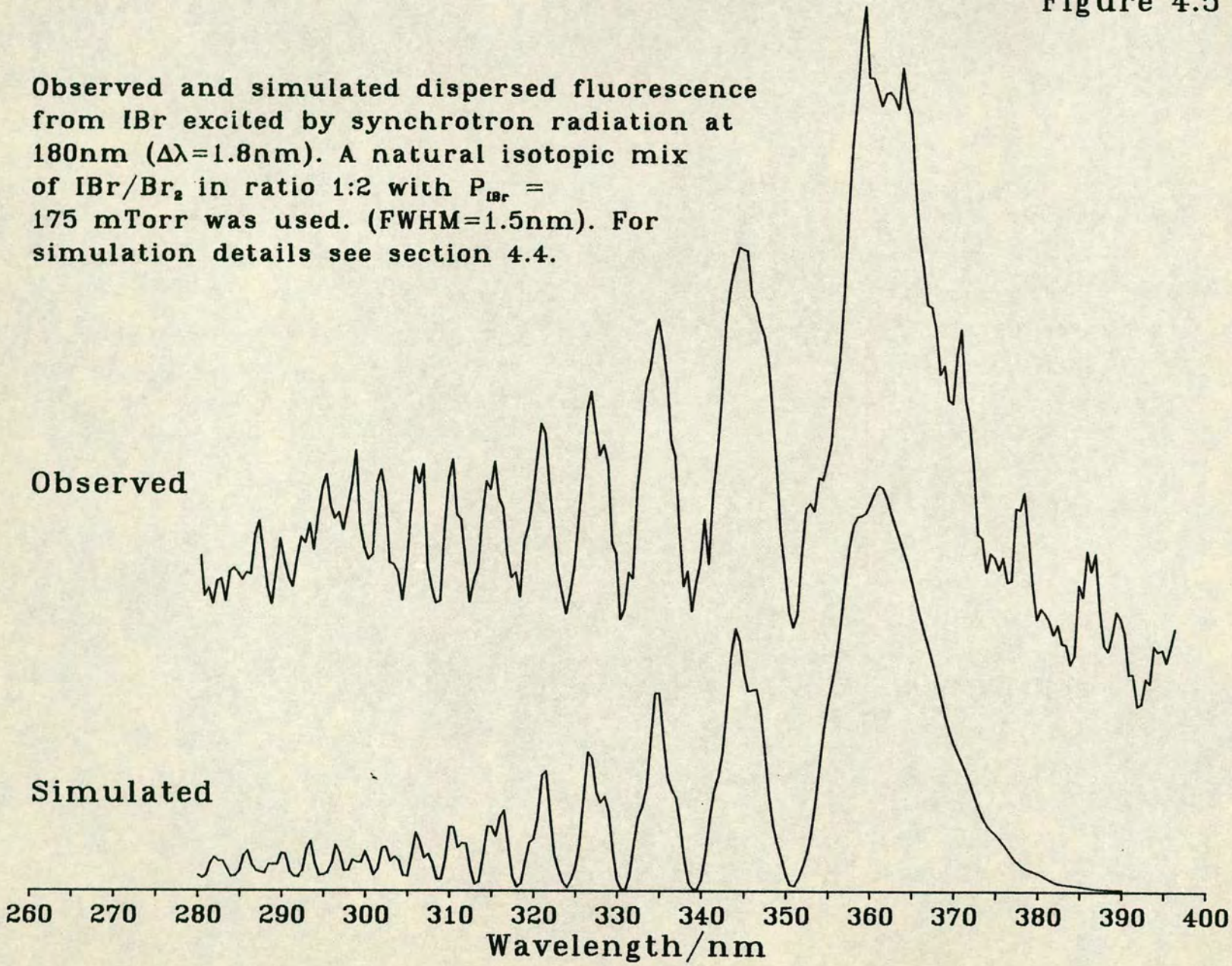

with transitions to unbound (above 244 nm) and bound (below 244 nm) regions of the ground state. The latter is the short wavelength system below 385 nm with a maximum at 365 nm extending, presumably beyond air cut-off, down to the excitation wavelength. The position of the long wavelength extremum is invariant with excitation wavelength. All spectra exhibited strong oscillations to the blue under a monotonically decaying envelope and the spectra in figure 4.5 and 4.6 also show a hint of higher frequency structure appearing as shoulders on these main peaks. The fluorescence excited at 193 nm and dispersed over a wider wavelength range was first published in reference [3] and is re-examined here under higher resolution, see figure 4.6. The overall appearance of this system is characteristic of a structured continuum associated with a maximum in the Mulliken difference potential , the analogy of the McLennan bands of $I_2$. Being the shortest wavelength feature of its type in fluorescence it is likely to end in the ground state. It is also known that $\Delta\Omega = 0$ transitions are strongly favoured in absorption making the E and f states possible upper state candidates. However, if absorption were to the $f(0^+)$ state, the origin of the f → X system would, from the difference in term values, lie approximately 6000 $cm^{-1}$ to the blue of the observed position. The long wavelength limit of the f → A or B system would also lie roughly 4000 $cm^{-1}$ to the blue of the observed origin (see table 4.1 and figure 4.8). We thus identify the strong system originating at 365 nm as $E(0^+) \rightarrow X(0^+)$, paralleling the McLennan bands of $I_2$ [6,19] i.e $I_2$ $D(0_u^+) \rightarrow X(^1\Sigma_g^+)$.

Fluorescence spectra involving wide bandwidth excitation, typical of the weak (although tunable) synchrotron radiation, present resolution limitations. Compounding this, as suggested by MacDonald with $Br_2$ [8], the use of a natural isotopic mix i.e. $I^{79}Br$ : $I^{81}Br$ in ratio 1:1, also imposes a physical constraint. Figure 4.6 shows the E → X system following excitation by an ArF laser ( $\lambda$ = 193 nm). Although having a narrow excitation bandwidth ( $\Delta\lambda$ = 10 $cm^{-1}$) and a medium monochromator resolution (FWHM = 0.3 nm), the high frequency structure, which we would expect to resolve, remains only vaguely hinted at. There are five possible explanations: (i) the bandwidth of the laser is not narrow enough to isolate a single isotope; (ii) The laser can isolate a single isotope but collisions with other $I^{79}Br$ and $I^{81}Br$ molecules result in the original excitation being transferred to the bulk sample; (iii) The laser can isolate and populate a single isotope, but in addition the ASE also populates a comparable population of the bulk sample; (iv) The resolution is poorer than the quoted

Observed and simulated dispersed fluorescence from IBr excited by a line narrowed ArF laser at 193nm ($\Delta\lambda$=0.05nm). A natural isotopic mix of IBr/$Br_2$ in ratio 1:2 with $P_{IBr}$ = 1.5 Torr was used. (FWHM=0.3nm). For simulation details see section 4.4.

Figure 4.6

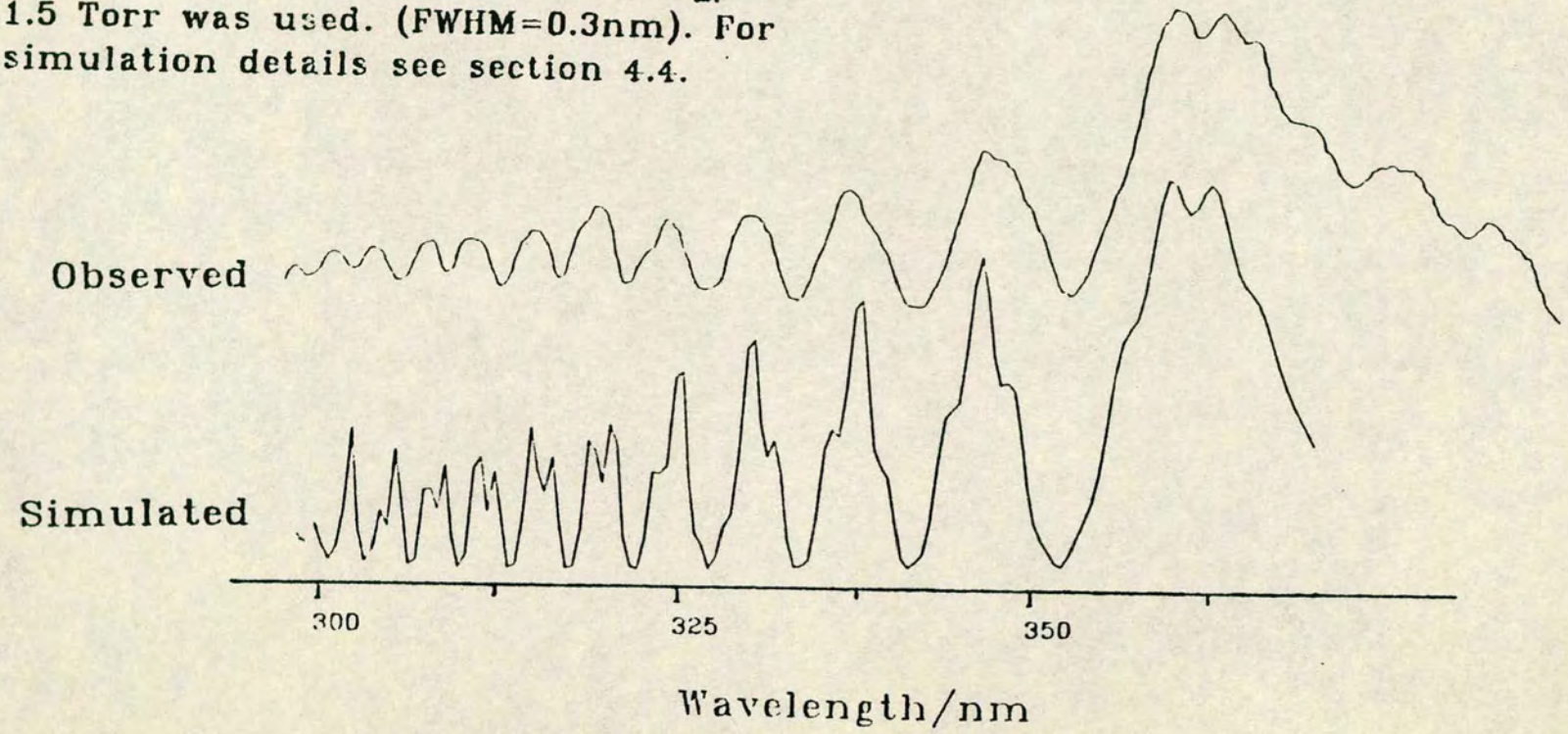

Figure 4.7

Observed and simulated dispersed fluorescence from IBr excited by a spectrofluorimeter centered at 200 nm ($\Delta\lambda$=15nm). A natural isotopic mix of IBr/$Br_2$ in ratio 1:1 with $P_{IBr}$ = 1 Torr was used. (FWHM=3.5nm). For simulation details see section 4.4.

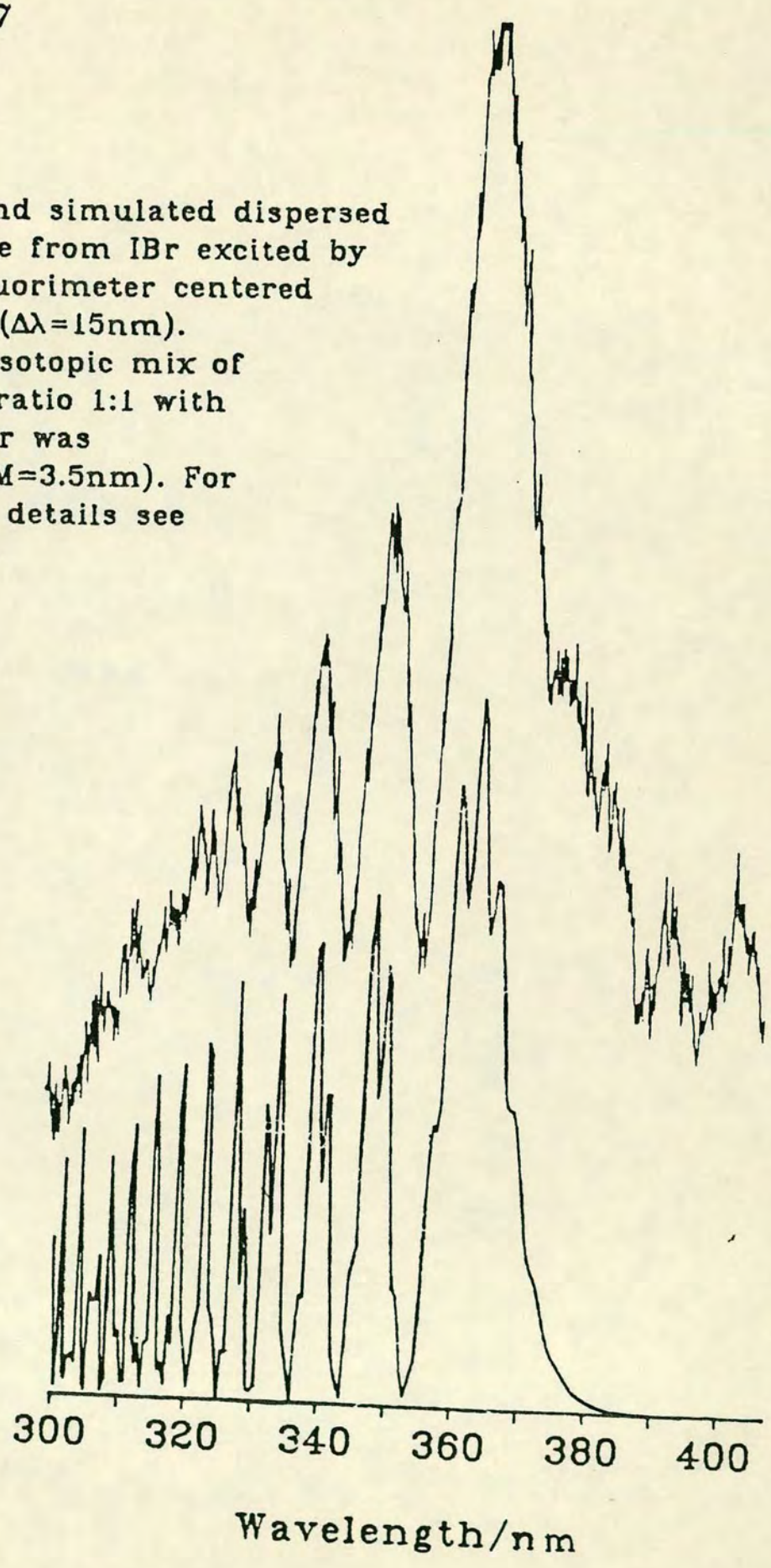

values; (v) There is some underlying (unresolved or structureless) fluorescence perhaps from the f state that when added to the E state fluorescence and renormalised, reduces the apparent amplitude of the high frequency structure.

(ii) cannot be entirely ruled out, although the conditions were typical of other experiments with other halogens and interhalides in which the fine structure was successfully resolved (see chapters 3 and 5). With (v) some fine structure should still be apparent especially since the coarse low frequency structure seems perfectly intact. This leaves, as possible explanations, (i), (iii) and (iv). Therefore it is most likely that the high frequency structure has been degraded by a shifting and overlapping of spectra emitted from different isotopic pairs which are absorbing. The simulations support this (see section 4.4), substitution of isotopic pairs, as expected, leaves the low frequency structure unchanged but results in a phase shift of the high frequency structure, markedly reducing the effective resolution (c.f. figure 3.11 of $Br_2$).

The E → X fluorescence excited at 180 nm (figures 4.3 and 4.5) exhibits anomalous underlying structure around 296 nm. This cannot be accounted for by pure E state fluorescence. Analogous features have also been seen with $I_2$ [6], $Br_2$ (see section 3.3.3) and ICl (section 5.3.3). Its absence in the other spectra reveals an excitation wavelength dependence and there is also evidence of a pressure dependence. We suggest this emission originates in the $f(0^+)$ state [2o], the next highest ion-pair state with $0^+$ symmetry. Population may be direct, by collisional transfer or both. $\Delta T_e$ of the $E(0^+)$ and $f(0^+)$ states predict the observed rainbow separations to within 1 nm (250 $cm^{-1}$).

The second system in figures 4.3 and 4.4 also presents structured continua, although in this case of a single frequency type. The iodine counterpart may be found between 350nm and 400nm [36] and is assigned as $A^a$ transition to a lower repulsive state; from the difference in red extrema we tentatively propose the inner wall of the B or B' states. No analysis of this system is attempted here, for further details see reference [8].

Figures 4.3-7 are entirely consistent with our interpretation of the absorption and fluorescence excitation spectra discussed in section 4.3.1 and 4.3.2.

## 4.4 Detailed Fitting

Small variations in the upper and lower state potentials outside the range of classical points of transition have almost no effect on fluorescence in which the high frequency interference structure is not resolved. However, to simulate the $E(0^+) \rightarrow X(0^+)$ dispersed fluorescence from high vibrational levels, we must extend both states to support all the wavefunctions involved. An RKR analysis based on the first 31 vibrational levels exists for the E state [21] covering turning points from 2.927 Å to 4.199 Å and up to roughly 10% of $D_e$. (see table 4.3). $T_e$ is firmly located at 39487.8 $cm^{-1}$. Similarly, an RKR analysis based on the first 19 vibrational levels exists for the X state [22] covering turning points from 2.2198 Å to 2.8899 Å and up to roughly 30% of $D_e$. The dissociation energy of the ground state is accurately known $D_e$ = 14664.9 $cm^{-1}$ (see table 4.1 and figure 4.8). This implies that the fluorescence between roughly 370 and 346 nm comes from classical points of transition in the known portion of the E state but lying in unknown sections of the X state. Below 346 nm , the observed fluorescence corresponds to bond lengths outwith the range of the RKR analysis of both states. However, both states need only be extrapolated by a further 0.6 Å to encompass all the observed fluorescence and fortunately there are standard funtional expansions for their long range behaviour, i.e. beyond the point of inflection.

A difference table of the attractive limb of the E state RKR points reveals that the point of inflection has just been attained; we can therefore extrapolate to large R by a modified Rittner analytical function, equation 4.1. (N.b. for an $I^+$ ion in the $^3P_{2,0}$ state the anion-quadrupole interaction energy should be positive.)

$$V_E(R) = T_\infty - C6/R^6 - C4/R^4 + C3/R^3 - e^2/4\pi\varepsilon_0 R \quad : R>4.2 \text{ Å} \qquad (4.1)$$

The coefficients C6, C4 and C3 were adjusted so that $V_E(R)$ was continuous in value and gradient with the RKR points at 4.2 Å. A satisfactory potential was obtained with C6 = 8.5 x $10^5$ $cm^{-1}Å^6$, C4 = 7.5 x $10^5$ $cm^{-1}Å^4$ and C3 = 6.2 x $10^4$ $cm^{-1}Å^3$. This extension is in the insensitive portion of the potential and these parameters should be regarded as estimates. In fact the C4 value is roughly 35% greater than suggested by equation 4.2:

$$C4 = e^2/4\pi\varepsilon_0 \cdot \tfrac{1}{2}(\alpha_+ + \alpha_-) = 5.56 \times 10^5 \text{ cm}^{-1}Å^4 \qquad (4.2)$$

Table 4.3

RKR turning points for the E state of $I^{79}Br$ using deperturbed constants of Brand and Hoy [21]

| v' | $R_{min}/\mathring{A}$ | $R_{max}/\mathring{A}$ | $G_v/cm^{-1}$ |
|---|---|---|---|
| 0 | 3.333 | 3.485 | 59.7 |
| 1 | 3.281 | 3.546 | 178.7 |
| 2 | 3.247 | 3.589 | 297.3 |
| 3 | 3.220 | 3.625 | 415.5 |
| 4 | 3.197 | 3.657 | 533.2 |
| 5 | 3.177 | 3.687 | 650.6 |
| 6 | 3.159 | 3.714 | 767.5 |
| 7 | 3.143 | 3.740 | 884.0 |
| 8 | 3.128 | 3.764 | 1000.1 |
| 9 | 3.114 | 3.788 | 1115.8 |
| 10 | 3.101 | 3.810 | 1231.0 |
| 11 | 3.089 | 3.832 | 1345.8 |
| 12 | 3.077 | 3.853 | 1460.1 |
| 13 | 3.066 | 3.874 | 1574.0 |
| 14 | 3.056 | 3.894 | 1687.5 |
| 15 | 3.046 | 3.914 | 1800.5 |
| 16 | 3.036 | 3.934 | 1913.2 |
| 17 | 3.027 | 3.953 | 2025.3 |
| 18 | 3.018 | 3.972 | 2137.0 |
| 19 | 3.010 | 3.990 | 2248.3 |
| 20 | 3.002 | 4.009 | 2359.1 |
| 21 | 2.994 | 4.027 | 2469.4 |
| 22 | 2.986 | 4.045 | 2579.4 |
| 23 | 2.979 | 4.062 | 2688.8 |
| 24 | 2.972 | 4.080 | 2797.8 |
| 25 | 2.965 | 4.098 | 2906.3 |
| 26 | 2.958 | 4.115 | 3014.4 |
| 27 | 2.952 | 4.132 | 3122.0 |
| 28 | 2.945 | 4.149 | 3229.1 |
| 29 | 2.939 | 4.166 | 3335.8 |
| 30 | 2.933 | 4.183 | 3442.0 |
| 31 | 2.927 | 4.200 | 3547.7 |

$$C6 = 3/2.\alpha_+\alpha_-\omega_+\omega_-/(\omega_+ + \omega_-) = 7.6 \times 10^5 \text{ cm}^{-1}\text{Å}^6 \quad (4.3)$$

Similarly, C6 is roughly 12% greater than suggested by equation 4.3. This discrepancy has been encountered previously with $Br_2$ (see section 3.4.1) and $I_2$ [6], and we feel that this probably indicates an underestimation of the polarisability of the $Br^-$ and $I^-$ ions by Wilson and Curtis [23]. Furthermore, at R=4.2 Å, the C3 term is less than 3% of the coulomb term, the C4 term roughly 7% and the C6 term roughly 0.4%. Consequently care should be exercised when discussing the physical significance of these parameters. What is important is that the magnitudes and sign of the long range coefficients should be realistic so that the smallness of the non-Coulomb term contributions at R > 4.2 Å means that the outer branch of the E state potential is constrained to roughly ±30 $cm^{-1}$ by the RKR points and the pure Coulomb limb.

The inner wall was extrapolated from 2.9 Å by fitting the rather soft functional form of equation 4.4 to the first two RKR points:

$$V_E(R) = D_e + A + C10/R^{10} : R<2.9 \text{ Å} \quad (4.4)$$

With $D_e$ = 32500 $cm^{-1}$ the values A = $-3.4316 \times 10^4$ $cm^{-1}$ and C10 = $2.4806 \times 10^8$ $cm^{-1}Å^{10}$ were obtained. This potential results in a maximum in the E ← X absorption around 70000 $cm^{-1}$ (see figure 4.1) compared with the observed maximum of roughly 60000 $cm^{-1}$. There are two possible explanations: (i) our inward extrapolation is too harsh, although an $R^{-10}$ dependence for a repulsive potential wall was thought to be 'soft' enough; (ii) an avoided crossing of the E state at around 60,000 cm displaces the inner wall to smaller R. The latter phenomena is proving common in regions of ion-pair VUV absorption c.f. $Br_2$ (section 3.4.1) and $I_2$ [24]. Unfortunately our present data is not of a high enough quality to decide which of these alternatives is correct.

We first extended the ground state, $V_X(R)$, by scaling the more extensive $I_2$ and $Br_2$ ground state potentials. Reducing V(R) by $D_e$ and $R-R_e$ by $\rho = (\mu\omega_e^2/D_e)^{-\frac{1}{2}}$, yields $V^*(\rho)$ for the two homonuclear cases which are almost identical up to 80% of dissociation (see section 2.2). We took the average of these two reduced potentials and "de-scaled" by $D_e$ and $\rho$ appropriate to IBr. The resulting potential was within 10% in energy and very nearly continuous in first derivative with the last two RKR points on the attractive limb. Nine knot points were placed on this extrapolated curve and subjected to the slight variations needed to simulate the observed fluorescence. The inner wall of the

ground state was extrapolated using equation 4.5:

$$V_X(R) = D_e + A + C13/R^{13} : R<2.2\ \text{Å} \qquad (4.5)$$

The values A = $-1.8265 \times 10^{14}$ $cm^{-1}$, C13 = $2.7065 \times 10^{8}$ $cm^{-1}Å^{13}$ were obtained. At each iteration the potential was obtained by a spline fit of the knot points plus RKR points . The upper state remained unchanged from its description above.

Calculations show that in systems where no fine structure is resolved, simulations are insensitive to excitation band width. In addition, despite large differences in $B_v$ values of upper and lower states, the rotational dependence of the analysed system was minimal and simulations were all performed at $J_{max}' = 43$ (see equation 2.13). The final simulations are shown in figures 4.5–7 (lower traces). Almost all trace of the underlying high frequency structure has been 'washed-in' by the equal weighting of $I^{79}Br$ and $I^{81}Br$ spectra. This is emphasised by not slit convoluting the calculated spectra.

The nature of the fitting procedure makes it hard to assign precise limits of uncertainty to the derived potential, but $V_X(R)$, as quoted at equally spaced values of R between 2.9 Å and 4.5 Å in table 4.4, is probably located to ±40 $cm^{-1}$. Attempting to fit this portion of the potential by the functional form,

$$V_X(R) = D_e - C6/R^6 - C8/R^8 : R>3.1\ \text{Å} \qquad (4.6)$$

will necessarily result in highly correlated values of C6 and C8. As pointed out by Chang [25] and Brand and Hoy [26] the C5 term is zero. If the C6 term is evaluated from the Kramer–Herschbach combination rule ([27] and equation 4.7), the best fit value of C8 is $4.0 \times 10^{7}$ $cm^{-1}Å^{8}$.

$$C_{ab} = 2C_{aa}C_{bb}/[(\alpha_b/\alpha_a)C_{aa} + (\alpha_a/\alpha_b)C_{bb}]$$
$$= 1.093 \times 10^{6}\ cm^{-1}Å^{6} \qquad (4.7)$$

The resulting ratio C6/C8 = 0.027 is rather low when compared with that for $I_2$ and $Cl_2$, 0.050 and 0.094 respectively [28,29].

The optimised E state potential can be described by "pseudo-RKR points", the classical turning points of the vibrational quantum states supported by the potential. The absolute vibrational numbering is thereby established in the E state (subject to our extrapolation of the inner wall); and this is included with the turning points in table 4.5. The E and X states, as described above, and

Table 4.4

IBr X-State, attractive branch [a]

| R/Å | V/cm$^{-1}$ [b] |
|---|---|
| 2.9 | 5070 |
| 3.0 | 6571 |
| 3.1 | 7997 |
| 3.2 | 9276 |
| 3.3 | 10324 |
| 3.4 | 11293 |
| 3.5 | 12136 |
| 3.6 | 12738 |
| 3.7 | 13112 |
| 3.8 | 13378 |
| 3.9 | 13608 |
| 4.0 | 13788 |
| 4.1 | 13933 |
| 4.2 | 14053 |
| 4.3 | 14150 |
| 4.4 | 14229 |
| 4.5 | 14295 |

a) the RKR analysis of Weinstock and Preston [22] finishes at R = 2.9 Å

b) relative to minimum of potential

some other known states of IBr, are shown in figure 4.8.

The observed fluorescence shows a marked fall-off in intensity towards the blue. This could only be accounted for by the transition moment function, $\mu_{12}(R)$ being broadly peaked just to the long bond length side of the minimum of the E state i.e. around 3.65 Å. The observed decay envelope could only be reproduced if both interfering branches of the difference potential are attenuated; a step or tanh like function was not sufficient. The simple Gaussian (equation 4.8) reproduced the ratio of the first few peak intensities quite well.

$$\mu_{12}(R) = A.\exp(-3/2(R - 3.65)^2) \qquad (4.8)$$

Transition moment functions exhibiting a maximum near $R_e$ of the ion-pair state have been seen in the $I_2$:D → X transition [6], the $Br_2$:D → X transition (section 3.4.2.1) and the ICl:E → X transition (section 5.4.2). Because of its symmetric nature, the functional form 4.8 still gives equal weight to the inner and outer classical points of transition on the Mulliken difference potential and this leads to almost complete interference between the low frequency structure. The actual fluorescence shows filling-in of the low frequency minima, even after allowing for loss of resolution due to the slit function. This is particularly evident in figure 4.6 recorded using a line narrowed ArF laser and medium resolution monochromator and may indicate some asymmetry in $\mu_{12}(R)$ about its maximum. But, as this filling-in appears even between the first and second supernumerary oscillations, it is more likely due to other weaker systems running under the dominant E → X fluorescence from the blue, perhaps associated with the f state.

## 4.5 Discussion

In all the halogens studied thus far the $\Delta\Omega = 0$ selection rule for single photon absorption from the ground state is found to dominate. IBr is no exception and the quasi-continuous absorption between 165 and 200 nm, being the furthest red feature of its type, is assigned as $E(0^+) \leftarrow X(0^+)$. The E state belongs to the first ion-pair cluster dissociating to the $^3P_2$ cation. Absorption across this band results in fluorescence in the 300 to 390 nm range; the lower state involved is identified as the ground state. The information contained within this 'McLennan' type system fixed the difference potential between 3.1Å and 4.8Å, corresponding to known regions of the $E(0^+)$ state but unknown

Table 4.5

Pseudo-RKR points for the $E(0^+)$ state of $I^{79}Br$ [a)]

| v' | $R_{min}$/Å | $R_{max}$/Å | $G_v$/cm$^{-1}$ |
|---|---|---|---|
| 40 | 2.882 | 4.349 | 4478 |
| 50 | 2.840 | 4.506 | 5472 |
| 60 | 2.805 | 4.656 | 6431 |
| 70 | 2.775 | 4.804 | 7357 |
| 80 | 2.750 | 4.954 | 8247 |
| 90 | 2.728 | 5.109 | 9096 |
| 100 | 2.708 | 5.272 | 9898 |
| 110 | 2.691 | 5.441 | 10655 |
| 120 | 2.676 | 5.612 | 11371 |
| 130 | 2.663 | 5.785 | 12051 |
| 140 | 2.651 | 5.960 | 12696 |
| 150 | 2.640 | 6.138 | 13310 |
| 160 | 2.630 | 6.320 | 13893 |
| 170 | 2.621 | 6.505 | 14447 |
| 180 | 2.612 | 6.692 | 14975 |
| 190 | 2.605 | 6.882 | 15478 |
| 200 | 2.598 | 7.074 | 15959 |

a) The deperturbed Dunham Coefficients of ref. [21] were used to generate RKR points up to v' = 31, $G_{v'}$ = 3548 cm$^{-1}$ (see table 4.3)

Figure 4.8

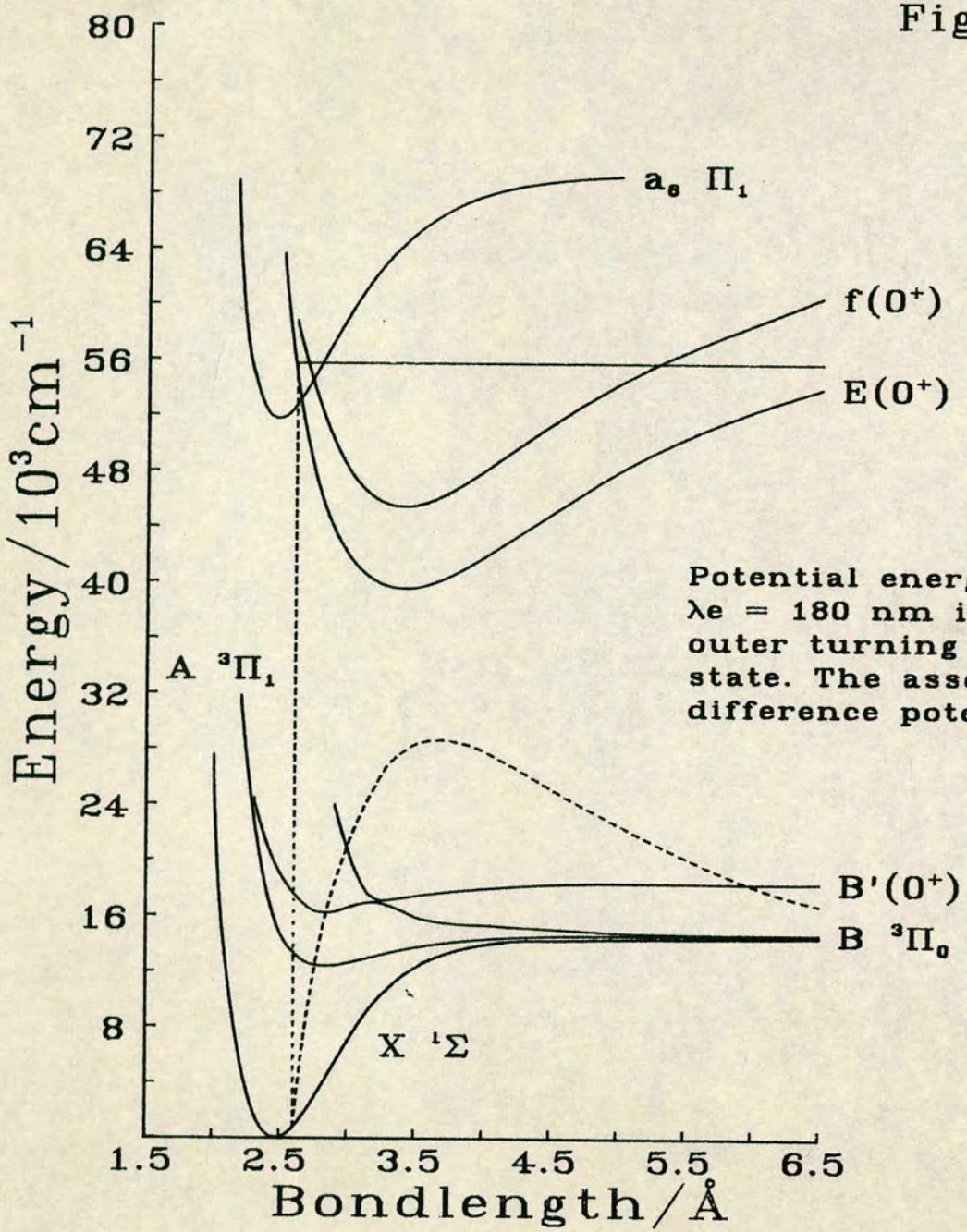


Potential energy curves of IBr. $\lambda e$ = 180 nm is shown from the outer turning point of the ground state. The associated Mulliken difference potential is also shown.

regions of the $X(^1\Sigma^+)$. A ground state potential that accounts for the observed dispersed fluorescence is presented (up to 97% of De). The extrapolation of the E state RKR turning points [21] is well characterised by the Rittner function and probably accurate to within $\pm 30$ $cm^{-1}$.

A rather broadly peaked transition moment function was needed to attenuate both limbs of the Mulliken difference potential and reproduce the intensity decay to the blue of the rainbow. This has proven to be a common feature of fluorescence from high vibronic states where the electron configuration (or valence bond character) can change rapidly, especially near an avoided crossing.

Another feature of such McLennan type systems is anomalous intensity in a spectral region where one would predict the second ion-pair state of $(0^+)$ symmetry, the f state, to produce a rainbow in fluorescence to the ground state. The f state belongs to the second ion-pair cluster dissociating to the $^3P_0$ cation. The exact nature of the population mechanism is still, unfortunately, unclear.

Fluorescence excitation spectra were simultaneously recorded with the absorption spectra, and indicate strong coupling between most of the Rydberg states and near resonant ion-pair vibrational levels of appropriate symmetry; the non-resonant ion-pair levels (as noted above) fluoresce strongly. There is also evidence for the strong predissociation of several Rydberg levels and this may be indirectly responsible for the collapse of the ion-pair fluorescence from the $E(0^+)$ state.

The similarities between the absorption and fluorescence excitation spectra of IBr and ICl make it clear that very similar processes are at work in both and any analysis of one molecule must be equally applicable to the other. Further work involving single isotope high resolution ($\Delta\lambda < 0.005$ nm) absorption/fluorescence excitation studies are obviously required to fully understand the low resolution spectra presented in this chapter. In addition, work at varying pressures of IBr also needs to be performed.

## References


1. R.J. Donovan and D. Husain, Trans. Farad. Soc., 64 2325 (1968) and refs. therein
2. R.J. Donovan and Robertson, Spec. Lttrs., 5 , 361 (1972)
3. M.A. MacDonald, J.P.T. Wilkinson, C. Fotakis, M. Martin and R.J. Donovan, Chem. Phys. Letts., 99, 250 (1983)
4. M.A. MacDonald, R.J. Donovan and M.C. Gower, Chem. Phys. letts, 97 72 (1983)
5. K.P. Lawley, D. Austin, R.J. Donovan and A.J. Yencha, submitted to Chem. Phys. (1987)
6. J.B. Tellinghuisen, Canad. J. Phys. 62 1933 (1984)
7. E. Kerr, M.A. MacDonald, R.J. Donovan, J.P.T. Wilkinson, D. Shaw and I. Munro, J. Photochem., 31, 149 (1985)
8. M.A. MacDonald, Ph.D. Thesis, University of Edinburgh, pp 37-43 (1984)
9. P. Venkateswarlu, Canad. J. Phys., 47, 2525 (1969)
10. R.J. Donovan, B.V. O'Grady, K. Shobatake and A. Hiraya, Chem. Phys. Letts., 122, 612 (1985)
11. W. Demtroder, Springer Series in Chem. Phys., 5 Laser Spec., p222 (1982)
12. M.I.T. Wavelength Tables, Wiley & Sons Inc., New York
13. J.P.T. Wilkinson, M.A. MacDonald and R.J. Donovan, J. Photochem., 35, 123 (1986)
14. A. Cordes and H. Sponer, Z. Physik, 79, 170 (1932)
15. P. Venkateswarlu, Canad. J. Phys., 53, 812 (1975)
16. R.S. Mulliken, Phys. Rev. 46, 549 (1934)
17. A. Yencha, R.J. Donovan, A. Hopkirk and D. Shaw, submitted to J. Phys Chem (1987)
18. R.J. Donovan and N. Nishi, Chem. Phys. Lttrs., 117, 286 (1985)
19. R.S. Mulliken, J. Chem. Phys., 55, 288 (1971)
20. J.C.D. Brand, U.D. Deshpande, A.R. Hoy, S.M. Jaywant and E.J. Woods, J. Mol. Spectrosc., 99, 339 (1983)
21. J.C.D. Brand, A.R. Hoy and A.C. Risbud, J. Mol. Spectrosc., 113, 47 (1985)
22. E.M. Weinstock and A. Preston, J. Mol. Spectrosc., 70, 188 (1978); see also M.A.A. Clyne and M.C. Heaven, J. Chem. Soc. Faraday II, 76, 49 (1980)
23. J.N. Wilson and R.M. Curtis, J. Phys. Chem., 74, 187 (1970)
24. J.C.D. Brand and A.R. Hoy, Chem. Phys., 109, 109 (1986)
25. T.Y. Chang, Rev. Mod. Phys., 39, 911 (1967)
26. J.C. Brand and A.R. Hoy, J. Mol. Spectrosc. 114, 197 (1985)
27. M. Saute, B. Bussery and M. Aubert-Frecon, Mol. Phys., 51, 1459 (1986)
28. F. Martin, S. Churassy, R. Bacis, R.W. Field and J. Verges, J. Chem. Phys., 79, 3725 (1983)
29. A.E. Douglas and A.R. Hoy, Canad. J. Phys., 53, 1965 (1975)
30. K.P. Huber and G. Herzberg, Molecular Structure and Molecular spectra, Vol. 4. Constants of diatomic molecules , Van Nostrand (1979)
31. G.W. King, I.M. Littlewood and J.R. Robins, Chem. Phys., 62, 359 (1981)
32. M. Child, Mol. Phys., 32, 1495 (1976)
33. M. Diegelmann, K. Hohla, F. Rebentrost and K.L. Kompa, J. Chem. Phys., 76, 1233 (1982)
34. J.C.D. Brand, D.R. Dhatt, A.R. Hoy and D.C. Tse, J. Mol. Spectrosc., 119, 398 (1986)
35. B.K. Clark and I.M. Littlewood, Chem. Phys. 107, 97 (1986)
36. K.P. Lawley, M.A. MacDonald and R.J. Donovan, Chem. Phys. Lttrs, 92, 322 (1982)

# CHAPTER 5
# IODINE MONOCHLORIDE

## 5.1 Introduction

The $E(0^+)$ and $f(0^+)$ ion-pair states of ICl have been studied with two-laser polarisation spectroscopy by Brand and Hoy [1-3] . Reliable RKR turning points exist up to v'=30 for the E state and v'=14 for the f state. In this chapter we reliably extend these potentials up to v'=115 and v'=66 for the E and f states respectively. A similar Optical-Optical Double Resonance (OODR) technique to references [1-4] was used but a novel analytical approach was adopted, independent of high resolution rotational observations and their inherent problems.

The ion-pair states were accessed by a two photon stepwise excitation via the intermediate $B^3\Pi_{0+}$ valence state (see figure 5.11). Whilst the first photon (the 'pump' laser) remained fixed, the second photon (the 'probe' laser) was scanned over a wide range of vibrational levels in the ion-pair states. Resonances in the probe laser scan were measured by the fluorescence excitation of the characteristically strong ion-pair → ground state fluorescent systems (see references [5-7] and below). The resolution of the pump laser easily distinguished between the two isotopic pairs constituting the natural mix i.e. $I^{35}Cl$ : $I^{37}Cl$ in ratio 3:1. And the resolution of the probe laser was sufficient to separate the P and R contributions for each vibrational transition. An example of the fluorescence excitation spectra for the $f(0^+)$: v'=55 and 56 levels is shown in figure 5.6. Absolute term values for a range of rovibrational levels of both states were measured to a high precision, in some cases up to ±0.3 $cm^{-1}$ (tables 5.2 and 5.3). At several of these levels the fluorescence monitored in excitation was also dispersed to give complete oscillatory continua. These range from the bound-bound blue origin up to the common long wavelength rainbow corresponding to transitions to the Mulliken difference potential maximum (figures 5.7-10). Successful simulation of these dispersed fluorescence spectra and the reproduction of the rovibrational term values measured in fluorescence excitation, fixes the potentials up to $T_e(E)$ + 14000 $cm^{-1}$ and $T_e(f)$ + 9600 $cm^{-1}$. These potentials are felt to be as reliable as the higher turning points of an RKR analysis.

Also reported in this chapter is the absorption spectrum of ICl using synchrotron radiation between 125 nm and 195 nm, see figure 5.1. It has the characteristic appearance of several sharp Rydberg vibrational progressions

superimposed on a broad partially resolved ion-pair absorption system. The absorption spectra of ICl has previously been reported by Venkateswarlu [8] and Bibinov [9], here we report additional, extensive relative cross section data with fluorescence excitation spectra collected simultaneously in the near UV. We will be concerned mainly with the ion-pair absorption system around 165nm. This state will later be identified as the aforesaid $E(0^+)$ [1] state of the first ion-pair cluster correlating with $I^+(^3P_2)$ + $Cl^-(^1S_0)$. Although of a much lower resolution than the OODR experiment, synchrotron spectra did yield partially resolved vibrational structure (figures 5.2 and 5.3), from which average local vibrational spacings could be extracted (typically $\delta(\Delta G_v)=\pm 5$ $cm^{-1}$). Franck-Condon arguments suggest that the single photon absorption will access higher vibrational levels than the OODR stepwise excitation through the $B^3\Pi_{0+}$ intermediate. This is confirmed by fitting a potential to the observed synchrotron average vibrational spacings which suggest $170 < v' < 310$ in the 160 nm - 176 nm range.

Excitation across the ion-pair absorption band resulted in highly structured oscillatory continuum emission in the near UV analogous to that observed from the lower levels excited in the OODR experiments (figures 5.4 and 5.5). The range of internuclear separation probed by all the analysed dispersed fluorescence spectra (OODR and synchrotron) was 2.58 Å to 5.17 Å in the E state and 2.64 Å to 4.67 Å in the f state. These correspond to well characterised regions of the ground state [10] but extend beyond the known portions of the $E(0^+)$ and $f(0^+)$ states [1,2]. Previous studies [7,5] have shown that a unique fit can be obtained if either the upper or lower states is well defined over most of the vibrational displacement responsible for the emission.

Chronologically the OODR work was done much later than that on the synchrotron, and for that reason is presented after the analysis of the synchrotron work even though it is of a much higher quality (although of a more limited range). The iterative nature of the analysis lent itself to this approach , the results of the synchrotron analysis provided a good starting point to the accurate fitting of the OODR work.

## 5.2 Experimental

### 5.2.1 The SRS

The absorption, wide-band fluorescence excitation studies, and some of the dispersed fluorescence work ($\lambda_e$ = 162.3 & 176 nm), were all performed using the synchrotron radiation source (SRS) at the SERC Daresbury Laboratory. The experimental details are well documented elsewhere [11,12], however, some of the salient features are discussed in section 3.2.1. Although the SRS is a tunable radiation source in the VUV, the relatively low intensity of the monochromated output limits its use to either low resolution work or to regions of strong absorption.

Absorption and fluorescence excitation spectra were collected simultaneously. Corrections for changes in synchrotron light intensity and the spectral response of the Seya excitation monochromator have been incorporated into figure 5.1. This allowed similar corrections to be estimated for figures 5.2 and 5.3 for which background runs were not available. The Seya excitation monochromator was initially calibrated by setting the wavelength indicator to zero at the maximum of zero order light. Further calibration checks were made across the Schumann-Runge bands of $O_2$ , and final accuracy was confirmed by comparison with the known Rydberg absorptions of ICl between 150 and 195 nm [8]. The output of the excitation monochromator was focused by a $CaF_2$ lens with a transmission cut-off at roughly 128 nm.

The combined response function for the dispersion monochromator and photomultiplier was flat, to within 10%, over the region 300-450 nm and thus corrections to the observed spectra are unnecessary. The dispersed fluorescence was calibrated against known emission lines from atomic iodine produced by excitation of $I_2$ at short wavelengths [13].

Great care was taken when changing gases because of halogen adsorption to the aluminium cell walls. In particular with $Br_2$ which was very persistent even after flushing, e.g. figure 5.2 has evidence of BrCl contamination.

### 5.2.2 Optical-Optical Double Resonance

Two dye lasers were employed, simultaneously pumped by a single excimer laser (Lambda Physik EMG201 MSC) operating on the 308 nm XeCl line (pulse duration 20 ns). The first dye laser (Lambda Physik FL3002E) selectively pumped a single rovibronic level (v'=1;J'=24) of the $B^3\Pi_{0+}$ state of the $I^{35}Cl$ isotopic combination ($\Delta\lambda$=0.01 $cm^{-1}$). The second dye laser (Lambda Physik FL2002) was used to pump molecules, excited by the first photon, from the $B^3\Pi_{0+}$ state to the $E(0^+)$ and $f(0^+)$ ion-pair states (see figure 5.11).

Samples of $ICl/Cl_2$ (1 Torr/1 Torr) mixtures were contained in a simple glass cell, fitted with Spectrosil quartz windows which were attached with fluorocarbon wax. Fluorescence was collected and imaged onto the entrance slit of a Jobin-Yvon HRS2 (f/7, 0.6m) monochromator using a 5 cm (f/1.5) focal length condenser lens and 15 cm focal length field lens. The dispersed emission at the exit slit was monitored using a Hamamatsu R928 photomultiplier, the output of which was fed to a Stanford Research systems SR250 gated integrator. During fluorescence excitation scans the pump dye laser was computer controlled by an IBM PC-XT. A fluorescence window of roughly 4 nm was monitored using an R166 photomultiplier centred at the short wavelength extremum of the ion-pair → ground state transition. This corresponds to relatively intense bound-bound fluorescence. The fluorescence excitation scans were calibrated against known molecular iodine emission [14] and an iron hollow cathode lamp [15]. This determined the total energy input to within typically ±0.8 $cm^{-1}$ and often ±0.3 $cm^{-1}$ , dependant on the spectral order of the probe laser and which of the aforesaid calibration sources was used. The dispersed fluorescence could be conveniently calibrated against the probe laser line which always lay embedded within the ion-pair → X system. Unfortunately no photomultiplier or monochromator grating response curves were available and the displayed spectra, figures 5.7-10, remain uncorrected; this has consequences when discussing the transition moment function (section 5.4.2).

## 5.3 Observations

### 5.3.1 The VUV absorption Spectrum

The single photon absorption spectrum of ICl between 128 nm ($CaF_2$ cut-off) and 195 nm is shown in figure 5.1. A pressure ratio of 2:1 of $Cl_2$/ICl ensured that equilibrium was established with negligible $I_2$ present. Since no trace of the strong $I_2$ Rydberg absorption below 175 nm [13,14] was detected, we can be sure that the weaker ion-pair absorption >170 nm will also be negligible. Furthermore, $Cl_2$ does not show any structured absorption above 145 nm [16]. Consequently all observed structure between 145 and 195 nm may be confidently attributed to ICl.

Within this region ICl exhibits two types of structure: (i) An underlying , extensive, partially resolved band system between roughly 157 nm and 180 nm; (ii) Three sharp intense systems with a local vibrational spacing of roughly 390 $cm^{-1}$ under a Gaussian envelope. The similarities with the analogous IBr spectrum (figure 4.1) are striking.

Structure of type (i) is characteristic of absorption to high on the inner wall of a broad ion-pair state (see table 5.1 and figure 5.12). It is known that $\Delta\Omega$ = 0 transitions are favoured in absorption from the ground state [17,18], making the $E(0^+)$ and $f(0^+)$ states strong candidates. In addition, the absence of any analogous absorption to the red suggests that, as in $Br_2$ (section 3.3.1) and IBr (section 4.3.1), we are accessing the first ion-pair cluster: we therefore assign the ion pair state as the $E(0^+)$ state.

The large increase in bond length of the ion-pair states produces a dense and extended rotational contour leading to extensive overlap of one band with another and medium to high resolution is needed to resolvé individual rovibronic transitions. However only two isotopic combinations are present i.e. $I^{35}Cl$ and $I^{37}Cl$ in ratio 3:1. With one combination dominating the natural isotopic mix, we can expect less problems with 'washing-in' encountered with IBr (chapter 4) and $Br_2$ (chapter 3). In fact, at medium resolution ($\Delta\lambda$ = 0.3 nm) ion-pair vibrational structure was detected between 159.5 nm and 164 nm; see figure 5.2 and tables 5.5 and 5.4. This spectrum is unfortunately contaminated with BrCl (see section 5.2.1) and the peaks marked by a '*' correspond to Rydberg transitions of BrCl [19]. There are two reasons for assigning the

Table 5.1

Spectroscopic constants for valence and ion-pair states of ICl

| State | $J_{Cl}$ [a)] | $J_I$ | $T_e/cm^{-1}$ | $\omega_e/cm^{-1}$ | $\omega_e x_e/cm^{-1}$ | $r_e/\AA$ | $T_\infty/cm^{-1}$ | Ref. |
|---|---|---|---|---|---|---|---|---|
| G (1) | 0 | 1 | 45552.8 | 184.8 | 0.674 | 3.23 | 79847 | 4 |
| f ($0^+$) | 0 | 0 | 44923.8 | 184.4 | 0.771 | 3.26 | 79208 | **3** |
| β (1) | 0 | 2 | 39103.7 | 170.3 | 0.468 | 3.293 | 72757 | 1, **2** |
| D'(2) | 0 | 2 | 39061.8 | 173.6 | 0.557 | 3.350 | 72757 | 1 |
| E ($0^+$) | 0 | 2 | 39059.5 | 165.6 | 0.289 | 3.255 | 72757 | 1, 2, **3**, **4** |
| B ($^3\pi_{0^+}$) | 3/2 | 1/2 | 17375.6 | 204.3 | 2.49 | 2.666 | 17558 | 26 |
| A ($^3\pi_1$) | 3/2 | 3/2 | 13742.9 | 211.0 | 2.12 | 2.685 | 17558 | 30 |
| A'($^3\pi_2$) | 3/2 | 3/2 | 12682.0 | 224.6 | 1.88 | 2.665 | 17558 | 31 |
| X ($^1\Sigma^+$) | 3/2 | 3/2 | 0 | 384.3 | 1.49 | 2.321 | 17558 | 10 |

a) The J states of the atomic or ionic products that correlate diabatically with the molecular state are given

Figure 5.1

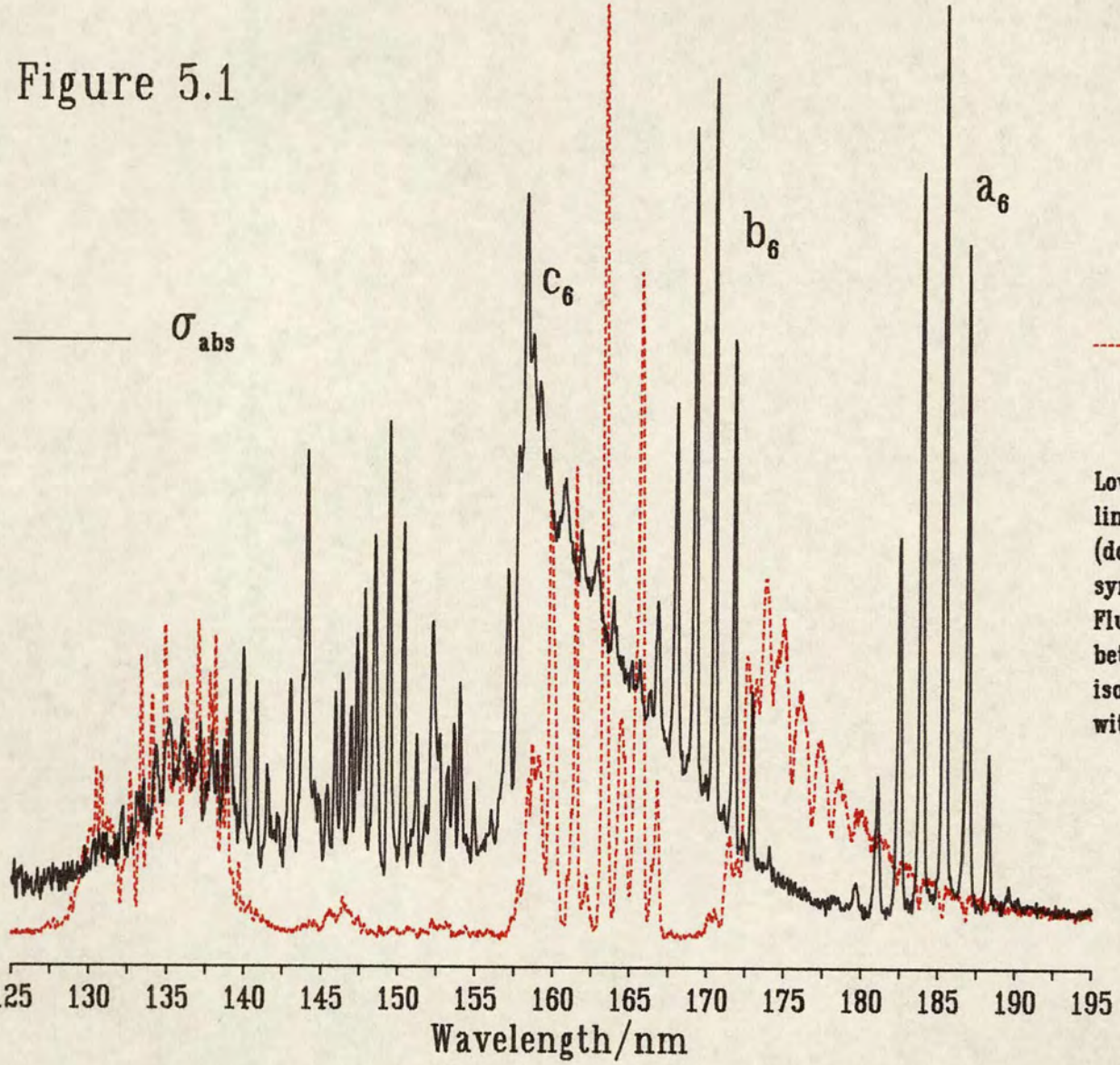


Low resolution absorption (solid line) and fluorescence excitation (dotted line) spectra of ICl using synchrotron radiation ($\Delta\lambda$=0.1nm). Fluorescence excitation collected between 270 & 480nm. A natural isotopic mix of ICl/$Cl_2$ in ratio 1:2 with $P_m$=134mTorr was used.

Figure 5.2

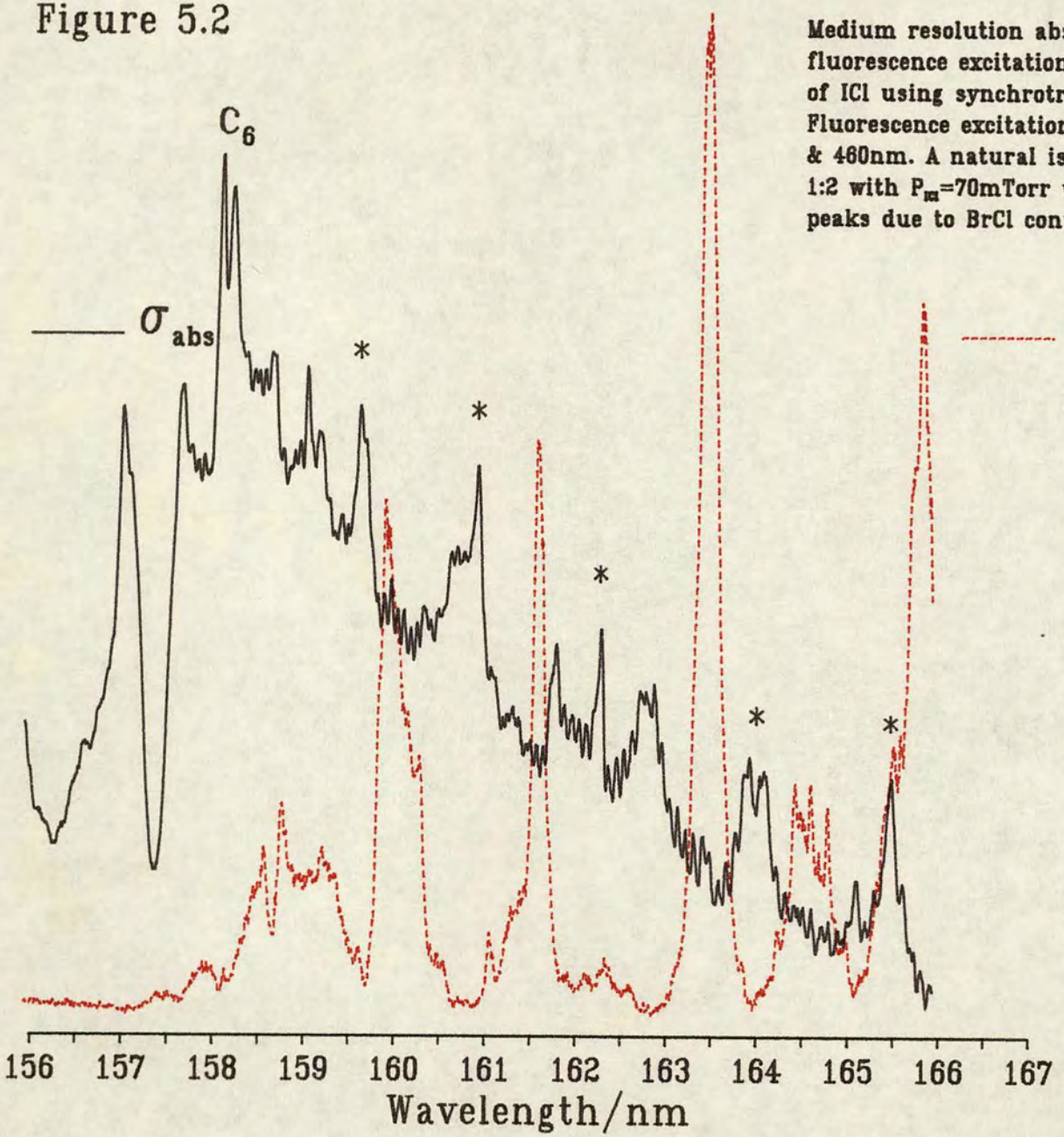


Medium resolution absorption (solid line) and fluorescence excitation (dotted line) spectra of ICl using synchrotron radiation ($\Delta\lambda$=0.03nm). Fluorescence excitation collected between 320 & 460nm. A natural isotopic mix of $ICl/Cl_2$ in ratio 1:2 with $P_{tot}$=70mTorr was used.( * indicate peaks due to BrCl contamination.)

closely spaced vibrational structure to an ion-pair state of ICl and not BrCl: (a) Typical Rydberg absorption is usually an order of magnitude more intense than underlying ion-pair absorption. Any BrCl ion-pair structure in this region would be much less pronounced than the vibrational structure partially resolved in figure 5.2; (b) More importantly, we believe no BrCl ion-pair absorption exists at these wavelengths [19]. In order to extract a meaningful local vibrational spacing, a quadratic, equation 5.1, was fitted to the two groups of vibrational levels:

$$E_{v+n} = E_v + a_1 n + a_2 n^2 \qquad (5.1)$$

For the group at ca 160 nm, with $0<n<5$;

$E_v = 62402\ cm^{-1}$ (=160.25 nm)
$a_1 = 30.0\ cm^{-1}$
$a_2 = -0.042\ cm^{-1}$
$\sigma = 5.0\ cm^{-1}$ (= std.dev.)

This suggests an average local vibrational spacing of 28 $cm^{-1}$ . For the group between 161.8 nm and 163.8 nm, with $0<n<22$;

$E_v = 61069\ cm^{-1}$ (=162.31 nm)
$a_1 = 34.1\ cm^{-1}$
$a_2 = -0.091\ cm^{-1}$
$\sigma = 4.6\ cm^{-1}$ (= std.dev.)

suggesting an average local vibrational spacing of 32 $cm^{-1}$ . In both cases $\sigma$ is rather large, this could be for three reasons: (i) evidence of perturbations; (ii) need for a cubic term; (iii) experimental error. The ratio of $a_1/a_2$ is large indicating probably no need for a cubic term. The biggest contribution to $\sigma$ is most likely poor resolution although if this was drastically improved no doubt we would uncover evidence of the widespread vibronic coupling that exist high in the ion-pair states. In section 5.4.1 we assign v = 316 of $I^{35}Cl$ for the peaks at ca 160 nm and v = 273 of $I^{35}Cl$ for the peaks between 161.8 nm 163.8 nm assuming Boltzmann rotational populations in the ground state.

The wider spaced structures are transitions to low lying ($v' < 6$) levels of Rydberg states and have been extensively analysed and assigned by Venkateswarlu using a 10.7 m spectrograph and photographic plates [8]. Our results are in complete accord and we identify the three strong Rydberg series above 155 nm as:

180 - 188 nm $(^2\Pi_{3/2})6s\sigma,\ \Pi_1 : a_6$
167 - 174 nm $(^2\Pi_{1/2})6s\sigma,\ \Pi_1 : b_6$

157 - 159 nm $(^2\Pi_{3/2})6p\sigma,\ \Pi_1 : c_6$

There is also complex Rydberg type structure overlying the ion-pair absorption between the $b_6$ and $c_6$ Rydberg systems i.e. between 159 and 167 nm. These peaks in absorption have a correlation with troughs in fluorescence excitation suggesting a strong ion-pair/Rydberg interaction where the Rydberg is either strongly predissociated or fluoresces in the VUV.

The Rydberg absorptions analysed by Venkateswarlu [8] provided a useful calibration check on the methods described in section 5.2.1.

### 5.3.2 The SRS Fluorescence Excitation Spectrum

The synchrotron fluorescence spectrum with all light between 270 and 480 nm collected, is shown in figure 5.1. We concentrate our discussion on the region involving the ion-pair state between roughly 158 and 195 nm. Two factors make the Rydberg states invisible in fluorescence excitation collected in the near UV; (i) many such states are predissociated (c.f. the $a_6$ state of IBr [20]); (ii) the most intense emission would be to bound regions of the ground state and lie in the VUV.

The broad peak between 170 and 190 nm will be shown in section 5.4.2 to come from the $E(0^+)$ ion-pair state and is punctuated by sharp dips with characteristic Rydberg spacing (figure 5.3). Individual ion-pair vibrational levels are clearly visible between 174.5 and 177 nm, although in absorption they appear to be weak in comparison with the noise level to register. As in section 5.3.1, in order to extract a meaningful local vibrational spacing , a quadratic (equation 5.1) was fitted to the observed levels (Table 5.6). In this case the fitted parameters, with $0 < n < 14$, were:

$E_v = 56557\ cm^{-1}$ (=176.81 nm)
$a_1 = 53.9\ cm^{-1}$
$a_2 = 0.009\ cm^{-1}$
$\sigma = 4.4\ cm^{-1}$ (= std.dev.)

Again $\sigma$ is large, and $a_2$ is in fact positive although very small. We feel this, as in section 5.3.1, is mostly due to the large errors incurred measuring the peak positions. The above parameters suggest an average local spacing of 54 $cm^{-1}$. In section 5.4.1 we assign v = 171 for $I^{35}Cl$ assuming normal Boltzmann rotational populations in the ground state.

Figure 5.3

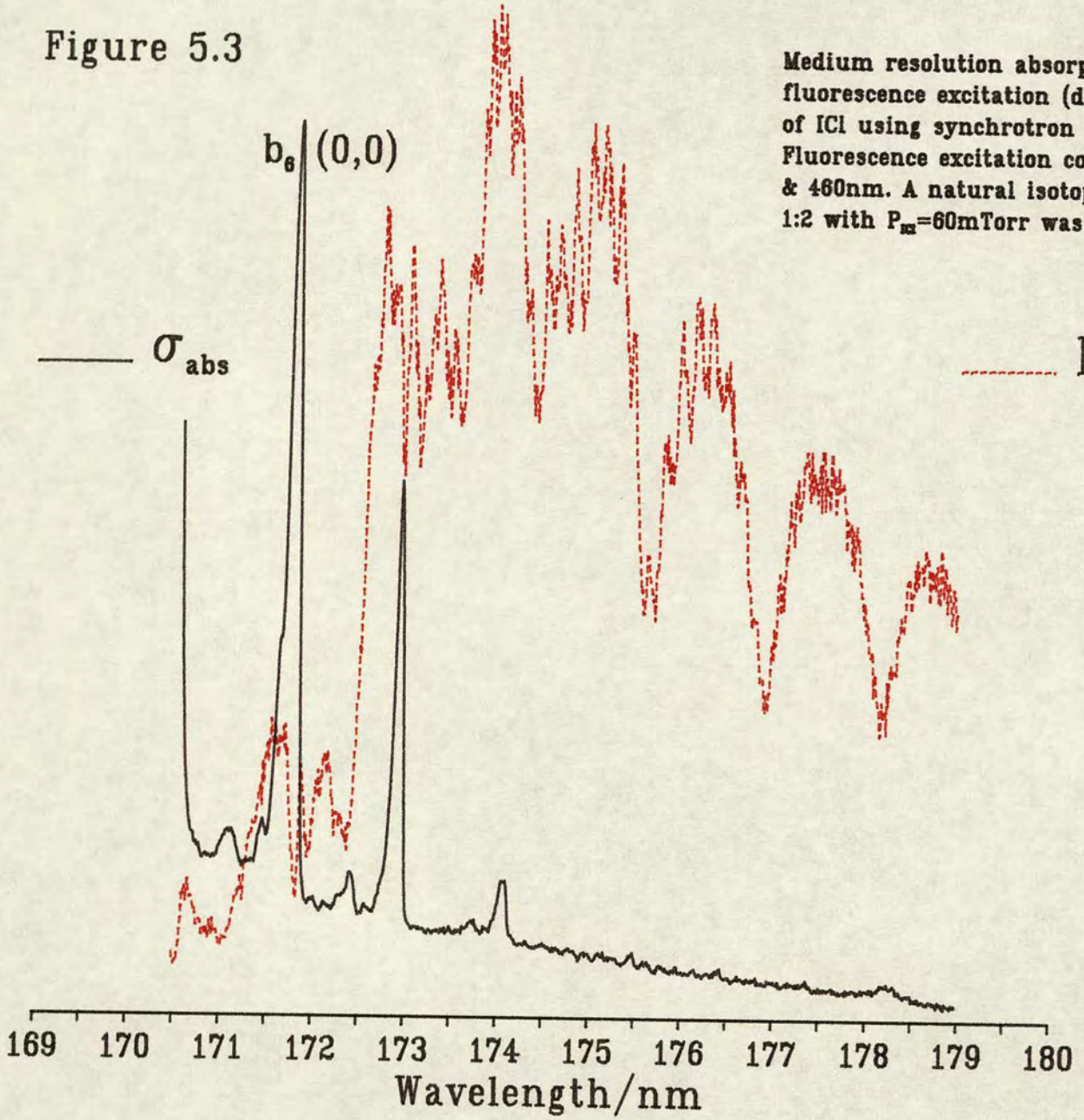


**Medium resolution absorption (solid line) and fluorescence excitation (dotted line) spectra of ICl using synchrotron radiation ($\Delta\lambda$=0.01nm). Fluorescence excitation collected between 320 & 460nm. A natural isotopic mix of ICl/$Cl_2$ in ratio 1:2 with $P_m$=60mTorr was used.**

The small dips observed between 181 and 190 nm (figure 5.1) reflect the strength of the corresponding $a_6$ Rydberg absorption and exhibit a pressure dependence [11]. They are clearly due to strong Rydberg absorption i.e. they are a reversal effect due to the optical density of the sample. In contrast the troughs between 181 and 174 nm exhibit a Rydberg type vibrational spacing but have no absorption counterparts. These are obviously evidence of ion-pair/Rydberg coupling. At 172.3 nm, the ion-pair fluorescence collapses, despite the continued rise in ion-pair absorption, and there follows a total lack of UV fluorescence between 167.5 and 170 nm. Eventually this gives way to a resonance structure with a characteristic Rydberg spacing with strong correlation of troughs in fluorescence to peaks in absorption. It is not the aim of this thesis to carry out a detailed analysis of the Rydberg/ion-pair coupling regions, nor their predissociations, but only the relatively unperturbed portions of the ion-pair contributions to the spectra. For further reading on the former subjects see reference [21].

### 5.3.3 SRS Dispersed Fluorescence Spectra

Low resolution dispersed fluorescence spectra were recorded at 162.3 and 176 nm using synchrotron radiation (figures 5.4 and 5.5). Comparison of figure 5.5 with the analogous emission of $I_2$ [7,22,23] and $Br_2$ (section 4.3.3), suggests three oscillatory continuum systems.

Two systems (> 450 nm) are associated with repulsive lower states and the third system (< 450 nm) involves transitions to bound and unbound regions of the ground state. The latter is the most intense system with a red extremum or rainbow at 410 nm extending, presumably beyond air cut-off, down to the excitation wavelength. The position of the rainbow appears invariant with excitation wavelength, and both high and low frequency structure are present, paralleling the McLennan bands of $I_2$ [7,24]. Being the shortest wavelength feature of its type in fluorescence and knowing that $\Delta\Omega=0$ transitions are strongly favoured in absorption, the $E(0^+)$ and $f(0^+)$ ion-pair states are strong candidates. However, if absorption were to the f state the f → X system would, from the difference in term values, lie approximately 5000 $cm^{-1}$ to the blue of the observed position. In addition, the red extremum of the f → A or B systems would also lie roughly 4000 $cm^{-1}$ to the blue (see figure 5.12). We thus identify the strong system originating at 410 nm as the $E(0^+)$ → X transition, the

Figure 5.4

Dispersed fluorescence of ICl excited by synchrotron radiation at 162.3nm ($\Delta\lambda$=4.5nm). A natural isotopic mix of ICl/$Cl_2$ in ratio 1:1.4 with $P_{ICl}$=246mTorr was used.(FWHM=8nm).

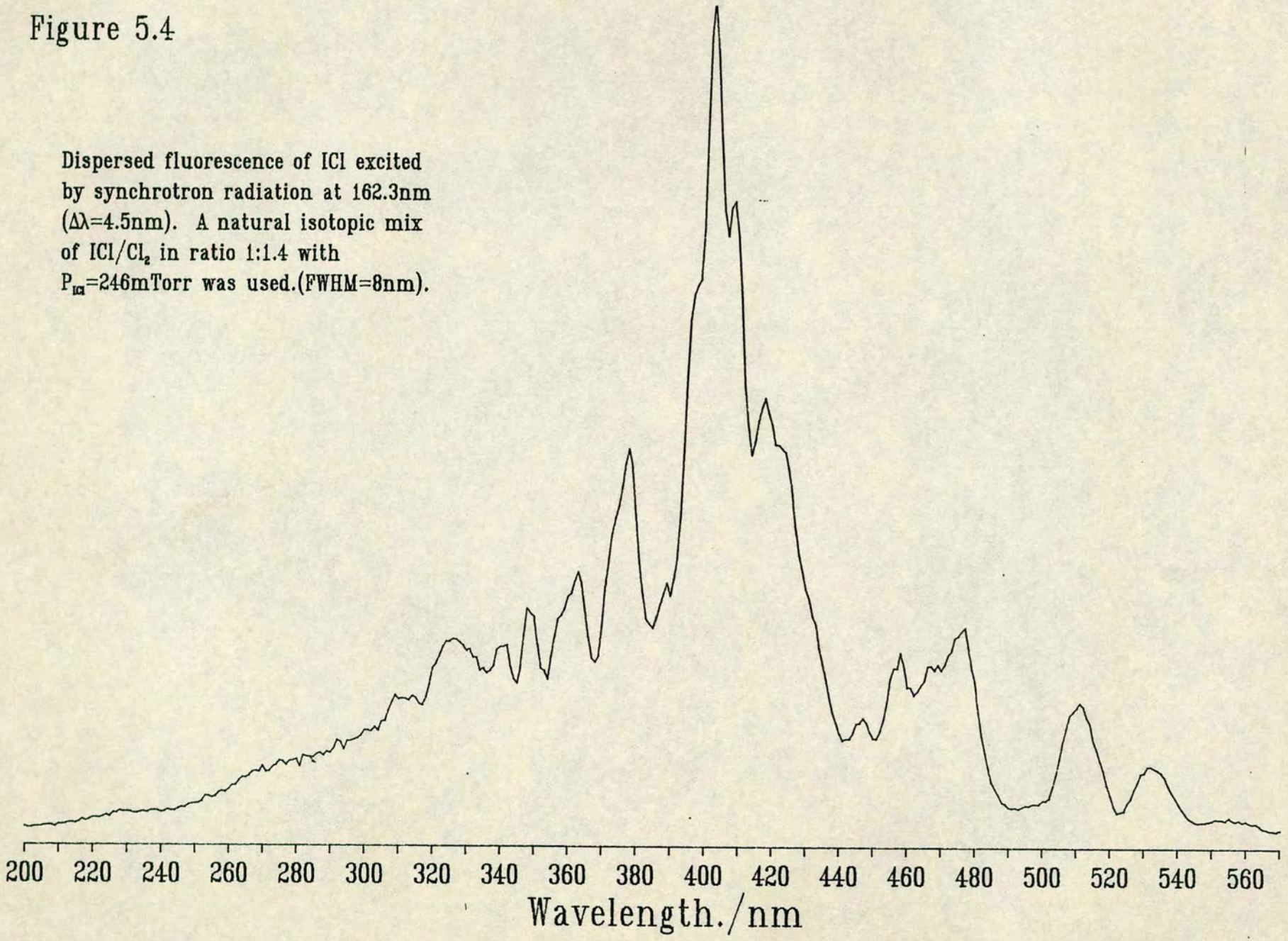

Figure 5.5

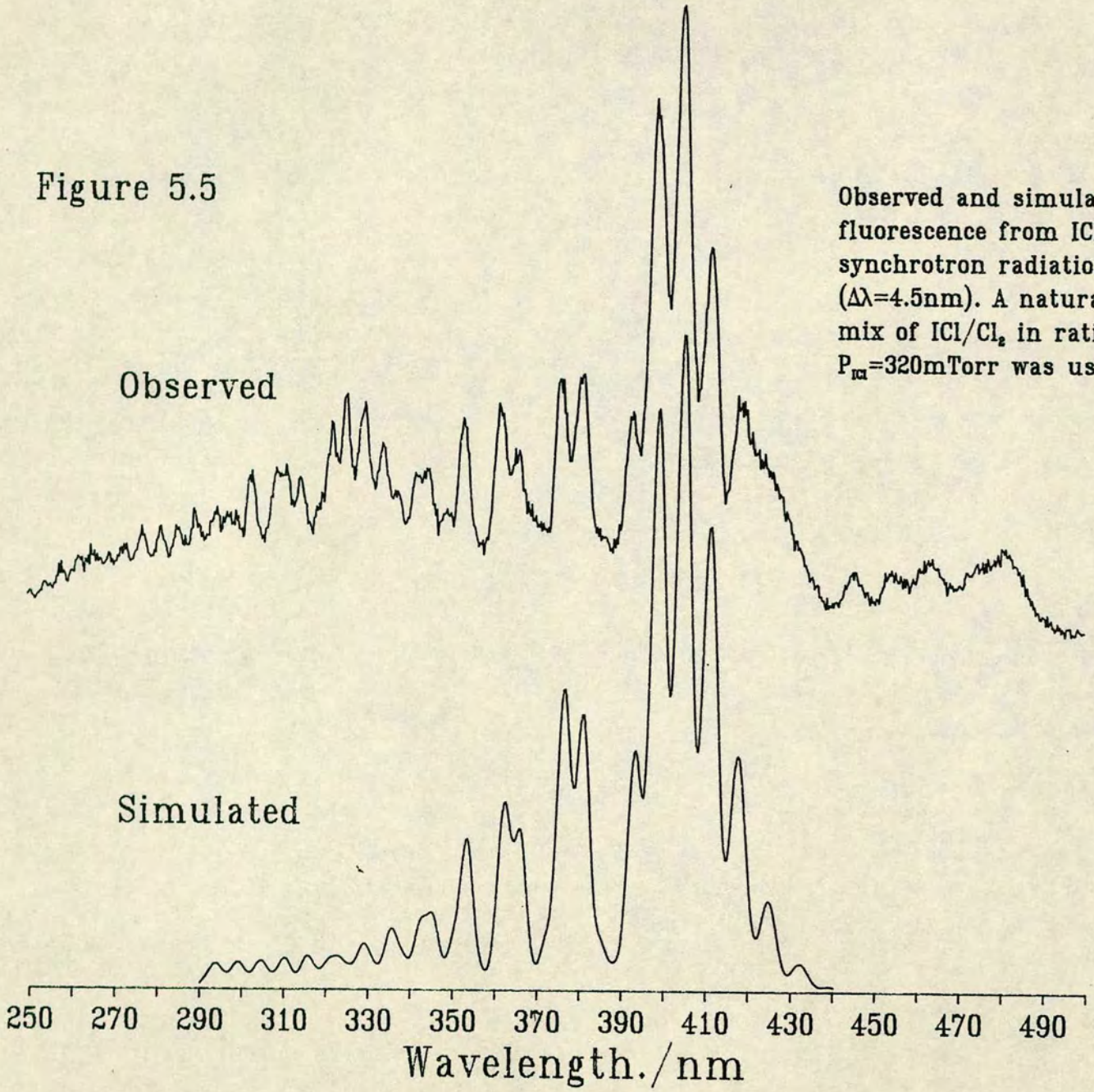


Observed and simulated dispersed fluorescence from ICl excited by synchrotron radiation at 176nm ($\Delta\lambda$=4.5nm). A natural isotopic mix of ICl/$Cl_2$ in ratio 1:2 with $P_{tot}$=320mTorr was used.(FWHM=1.5nm).

direct analogy of the McLennan system i.e. $I_2(D \rightarrow X)$.

Fluorescence spectra involving wide band width excitation typical of the weak (although tunable) synchrotron radiation, present resolution limitations. Compounding this as with $Br_2$ (section 3.3.3) and IBr (section 4.3.3), the use of a natural isotopic mix i.e. $I^{35}Cl$ : $I^{37}Cl$ in ratio 3:1, also imposes a physical constraint. Any high frequency structure will be degraded by a shifting and overlapping of spectra emitted from different isotopic pairs which are coincidently absorbing. The simulations support this; substitution of isotopic pairs resulted in a phase shift of the fine structure slightly reducing the effective resolution (c.f. figure 3.11 for $Br_2$). This effect however, was not as severe as in $Br_2$ or IBr due to the dominance of one isotopic combination i.e. $I^{35}Cl$. The greatest limitation on resolution proved to be the very wide band width excitation mentioned above.

Both $E \rightarrow X$ spectra excited at 162.3nm (figure 5.4) and 176 nm (figure 5.5) exhibit anomalous underlying structure around 325 nm, this cannot be accounted for by pure E state fluorescence. Analogous features have been seen with $I_2$ [7,25] , $Br_2$ (section 3.3.3) and IBr (section 4.3.3). It appears slightly more intense, in comparison with the $E \rightarrow X$ rainbow, in figure 5.5 than in figure 5.4, although its position seems to be maintained. There is also evidence of a pressure dependence [21]. We suggest this emission is the red extremum or rainbow of the $f \rightarrow X$ system, the f state being the next highest ion-pair state of $(0^+)$ symmetry. Population may be direct, by collisional transfer or by both. $\Delta T_e$ of the E and f states predict the observed rainbow separations to within 2.5 nm ( 200 $cm^{-1}$).

The second and third systems to the red of figure 5.4 also present structured continua. Their iodine and bromine counterparts suggest that these transitions will involve repulsive lower states and be of a 'single' frequency type. No analysis of these systems will be presented here, we merely note their possible contributions underlying the main $E \rightarrow X$ system.

### 5.3.4 OODR Fluorescence Excitation

The excitation scheme used to access the ion-pair states is shown in figure 5.11. The $B^3\Pi_{0+}$ state in the adiabatic limit undergoes an avoided crossing at roughly R = 3.25 Å with a repulsive continuum state [26]. Consequently it is

only stable up to v = 3 resulting in very poor Franck-Condon factors between the X and the B states. This is compensated by two $\Delta\Omega = 0$ transitions being used to reach the $E(0^+)$ and $f(0^+)$ states ($\Delta\Omega = 0$ transitions are nearly always more favourable than $\Delta\Omega = 1$). The pump laser coincidently excited the $I^{35}Cl$ B(v'=1;J'=24) ← X(v"=2;J"=25) and B(v'=1;J'=32) ← X(v"=2;J"=31) transitions, these lines were identified using constants for the X state by Brand and Hoy [10] and for the B state by Hansen et al [26]. An example of the subsequent fluorescence excitation spectrum on scanning the probe laser is shown in figure 5.6. The extracted term values for a range of rovibrational levels of both E and f states are listed in tables 5.2 and 5.3 respectively.

For the E state the above scheme was used up to v'=100, beyond this the FC factors from B(v"=1) became too small. Above E(v'=100) the B(v'=2;J'=11) ← X(v"=2;J"=12) pump line was used (see last three entries in table 5.2). Two factors limited observations at E(v'>120) ; (i) the bound-bound blue origin of the ion-pair to ground state transition, where the fluorescence was collected, gradually enters the VUV; (ii) falling off of the FC factors.

Nearly all the term values and vibrational spacings were successfully reproduced (column 4 of tables 5.2 and 5.3). Only v' = 96 of the E state seems out of step with the rest of the simulation, this result was rechecked and found to still lie significantly outwith the experimental error. We can only assume there is a rovibrational interaction between this level and the rovibrational level of another electronic state. Furthermore since we are still well below any known Rydberg levels (figure 5.12), another ion-pair state is the most likely candidate. This type of rovibrational perturbation has previously been observed for the $E(0^+)$ state coupling with another close lying (within 50 $cm^{-1}$ )member of the lowest ion-pair cluster, the $\beta(1)$ state [27]. Found between $0 < v_E < 7$, these perturbations involved typically several $cm^{-1}$ s, which is somewhat larger than our predicted 0.9 $cm^{-1}$ . This may be because only at very low v values does one get good overlap between vibrational wavefunctions.

### 5.3.5 OODR Dispersed Fluorescence

Dispersed fluorescence was collected from two levels of both the $E(0^+)$ and $f(0^+)$ ion-pair states. The high resolution of the pump and probe lasers allowed a single rovibrational level of the dominant isotopic combination $I^{35}Cl$ to be isolated. Figures 5.7 and 5.8 show dispersed fluorescence from E(v'=53;J'=23)

Figure 5.6

A section of the high resolution fluorescence excitation spectrum of ICl using the OODR technique (sect. 5.2.2). Fluorescence was collected from a 4nm window centered on the bound–bound blue origin of the f–>X fluorescence. The B(v'=1;J'=24 & 32) levels of $I^{35}Cl$ were selectively pumped. ($\Delta\lambda$'pump'=0.1cm$^{-1}$).

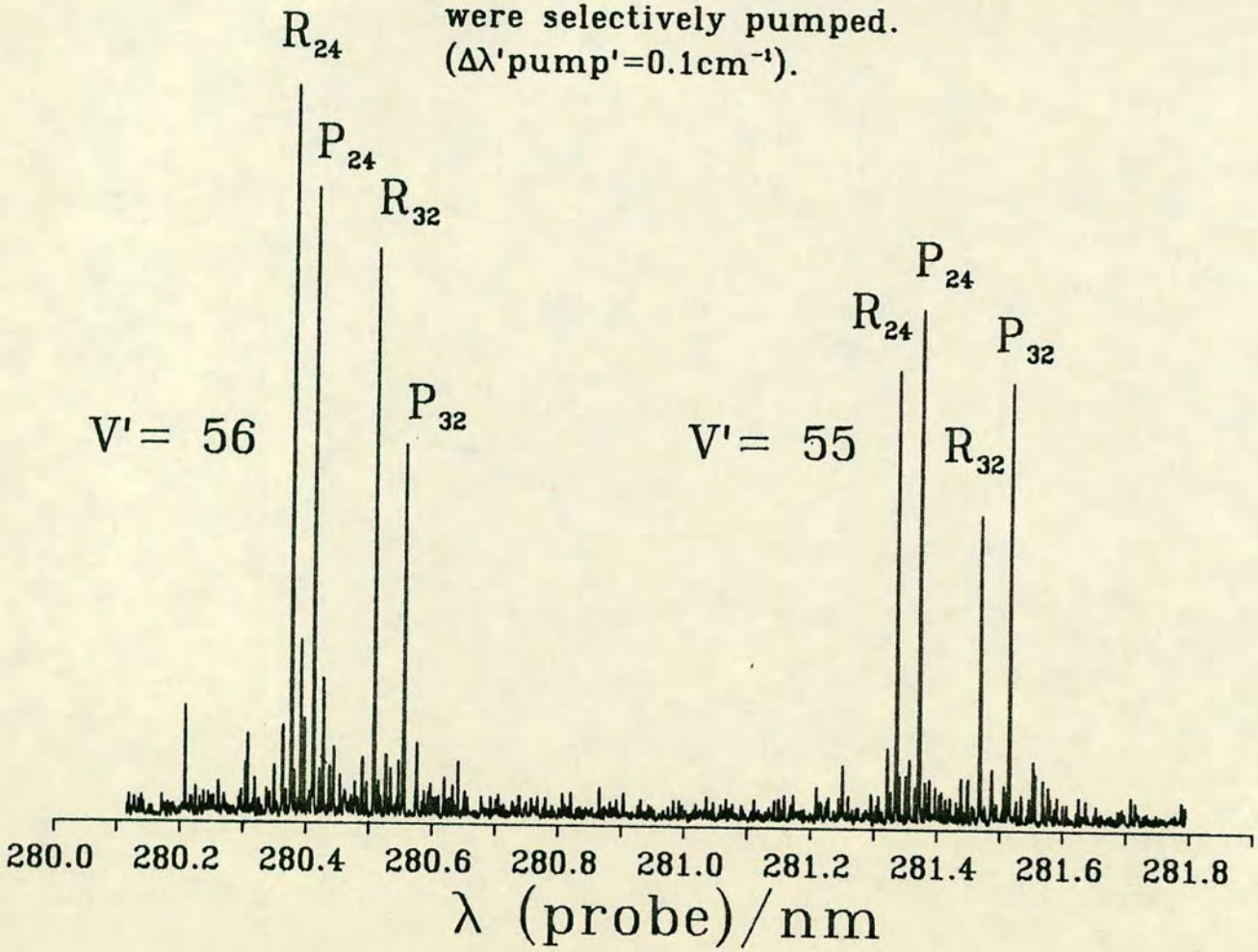

Table 5.2

Observed and calculated rovibrational term values for the $E(0^+)$ state of $I^{35}Cl$

| J' | v' | $G_v$(obs)[a] /cm$^{-1}$ | $G_v$(calc) /cm$^{-1}$ | $\Delta G_v$(obs) /cm$^{-1}$ | $\Delta G_v$(calc) /cm$^{-1}$ |
|---|---|---|---|---|---|
| 23 | 47 | 7026.7 | 7026.4 | | |
| 23 | 48 | 7153.4 | 7153.3 | 126.7 | 126.9 |
| 23 | 54 | 7897.4 | 7897.6 | - | - |
| 23 | 55 | 8018.6 | 8018.8 | 121.2 | 121.3 |
| 23 | 56 | 8139.1 | 8139.3 | 120.5 | 120.5 |
| 23 | 74 | 10177.9 | 10177.7 | - | - |
| 23 | 75 | 10283.9 | 10283.8 | 106.0 | 106.1 |
| 23 | 76 | 10389.1 | 10389.2 | 105.2 | 105.4 |
| 23 | 77 | 10493.7 | 10493.9 | 104.6 | 104.7 |
| 23 | 83 | 11106.8 | 11106.6 | - | - |
| 23 | 84 | 11206.4 | 11206.3 | 99.6 | 99.7 |
| 23 | 85 | 11305.7 | 11305.2 | 99.3 | 99.0 |
| 23 | 86 | 11403.8 | 11403.6 | 98.1 | 98.3 |
| 23 | 87 | 11501.8 | 11501.3 | 98.0 | 97.7 |
| 23 | 96 | 12356.1 | 12354.5 | - | - |
| 23 | 97 | 12447.1 | 12446.5 | 91.0 | 91.9 |
| 23 | 98 | 12538.5 | 12537.8 | 91.4 | 91.4 |
| 10 | 114 | 13897.1 | 13904.1 | - | - |
| 10 | 115 | 13978.6 | 13985.6 | 81.5 | 81.7 |
| 10 | 116 | 14059.3 | 14066.5 | 80.7 | 80.9 |

[a] relative to minimum of E state potential

$\delta G_{47-56} \simeq +/- 2$ cm$^{-1}$

$\delta G_{74-77} \simeq +/- 0.8$ cm$^{-1}$

$\delta G_{83-87} \simeq +/- 0.3$ cm$^{-1}$

$\delta G_{96-116} \simeq +/- 0.8$ cm$^{-1}$

Table 5.3

Observed and calculated rovibrational term values for the $f(0^+)$ state of $I^{35}Cl$

| J' | v' | $G_v$(obs)[a] /cm$^{-1}$ | $G_v$(calc) /cm$^{-1}$ | $\Delta G_v$(obs) /cm$^{-1}$ | $\Delta G_v$(calc) /cm$^{-1}$ |
|---|---|---|---|---|---|
| 23 | 6 | 1197.7 | 1198.2 | | |
| 23 | 7 | 1371.5 | 1372.2 | 173.8 | 174.0 |
| 23 | 11 | 2052.5 | 2054.7 | - | - |
| 23 | 12 | 2219.8 | 2222.1 | 167.3 | 167.4 |
| 23 | 24 | 4134.4 | 4134.6 | - | - |
| 23 | 25 | 4285.7 | 4286.3 | 151.3 | 151.5 |
| 23 | 26 | 4436.1 | 4436.3 | 150.4 | 150.3 |
| 23 | 34 | 5597.9 | 5598.0 | - | - |
| 23 | 35 | 5738.4 | 5738.4 | 140.5 | 140.4 |
| 23 | 36 | 5877.8 | 5877.8 | 139.4 | 139.4 |
| 23 | 54 | 8223.5 | 8223.5 | - | - |
| 23 | 55 | 8345.0 | 8345.1 | 121.5 | 121.7 |
| 23 | 56 | 8465.4 | 8465.9 | 120.4 | 120.7 |
| 23 | 64 | 9398.8 | 9399.3 | - | - |
| 23 | 65 | 9511.5 | 9512.0 | 112.7 | 112.7 |
| 23 | 66 | 9624.0 | 9624.0 | 112.5 | 111.9 |

[a] relative to the minimum of the f state potential

Figure 5.7

Simulated and observed dispersed fluorescence of $I^{35}Cl$, E(v'=53;J'=23)->X, excited by OODR. A natural isotopic mix of $ICL/Cl_2$ in ratio 1:2 with $P_m$=1 Torr was used.(FWHM=0.5nm).

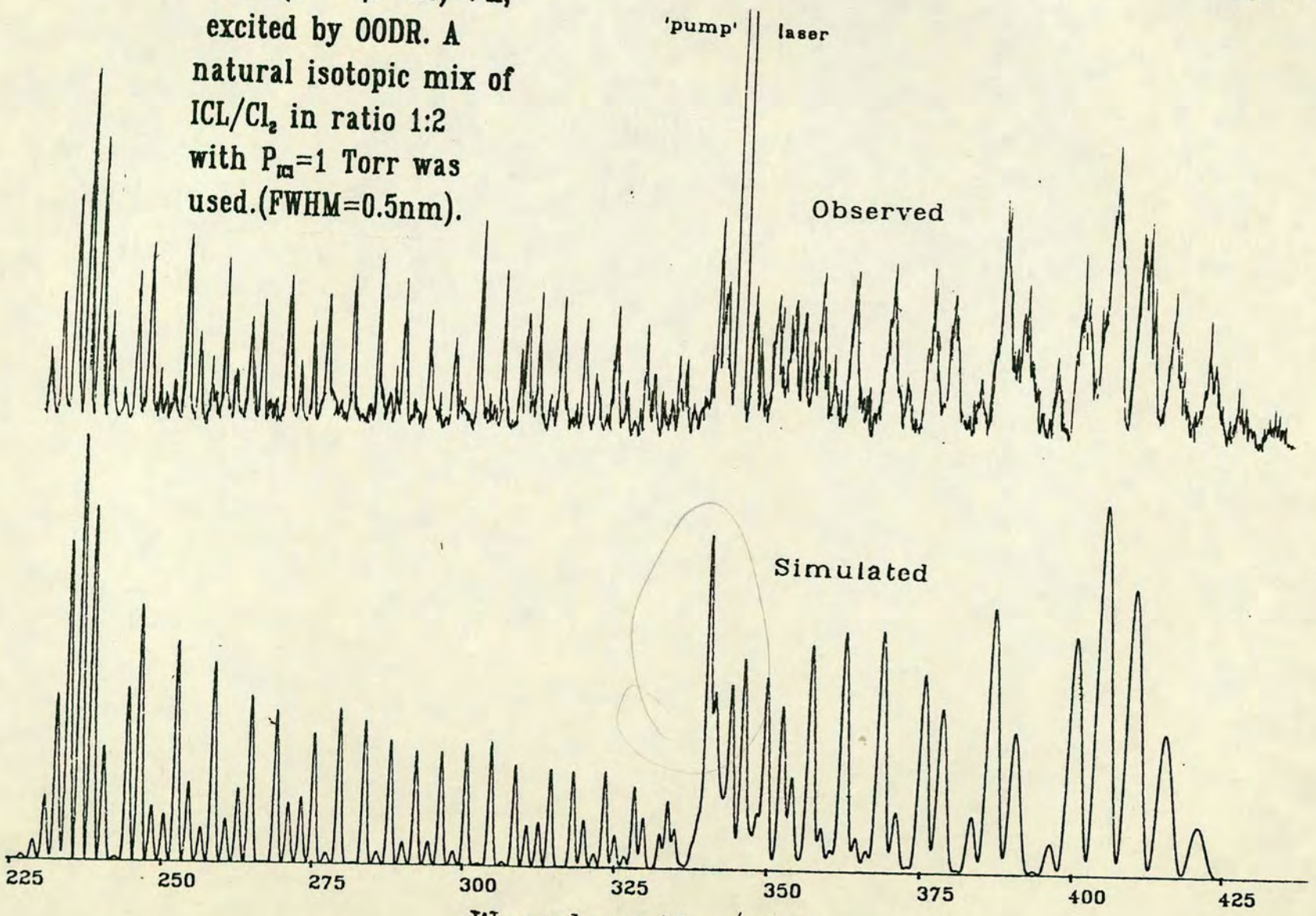

Figure 5.8

Simulated and observed dispersed fluorescence of $I^{35}Cl$, E(v'=76;J'=23)->X, excited by OODR. A natural isotopic mix of $ICL/Cl_2$ in ratio 1:2 with $P_{tot}$=1 Torr was used.(FWHM=0.75nm).

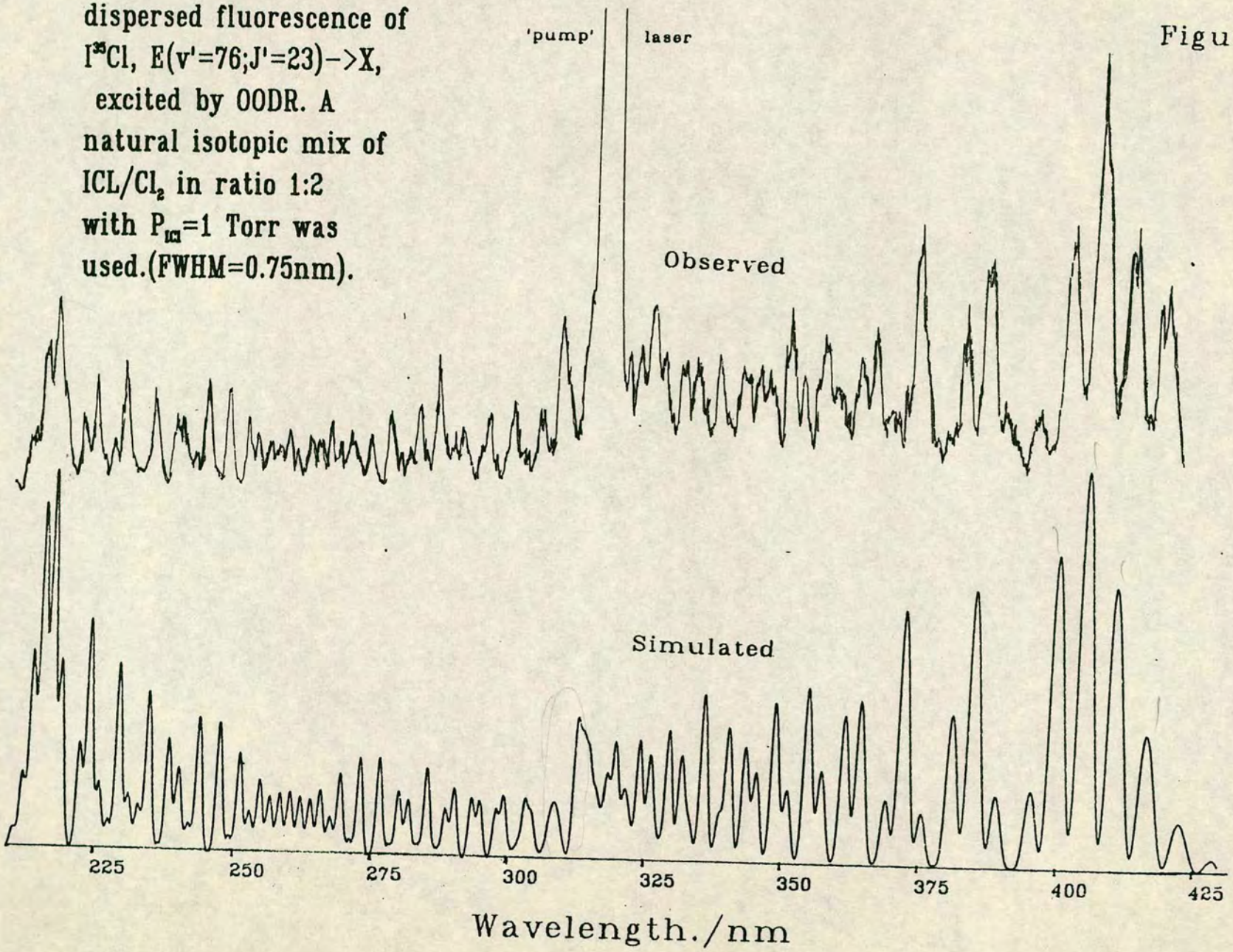

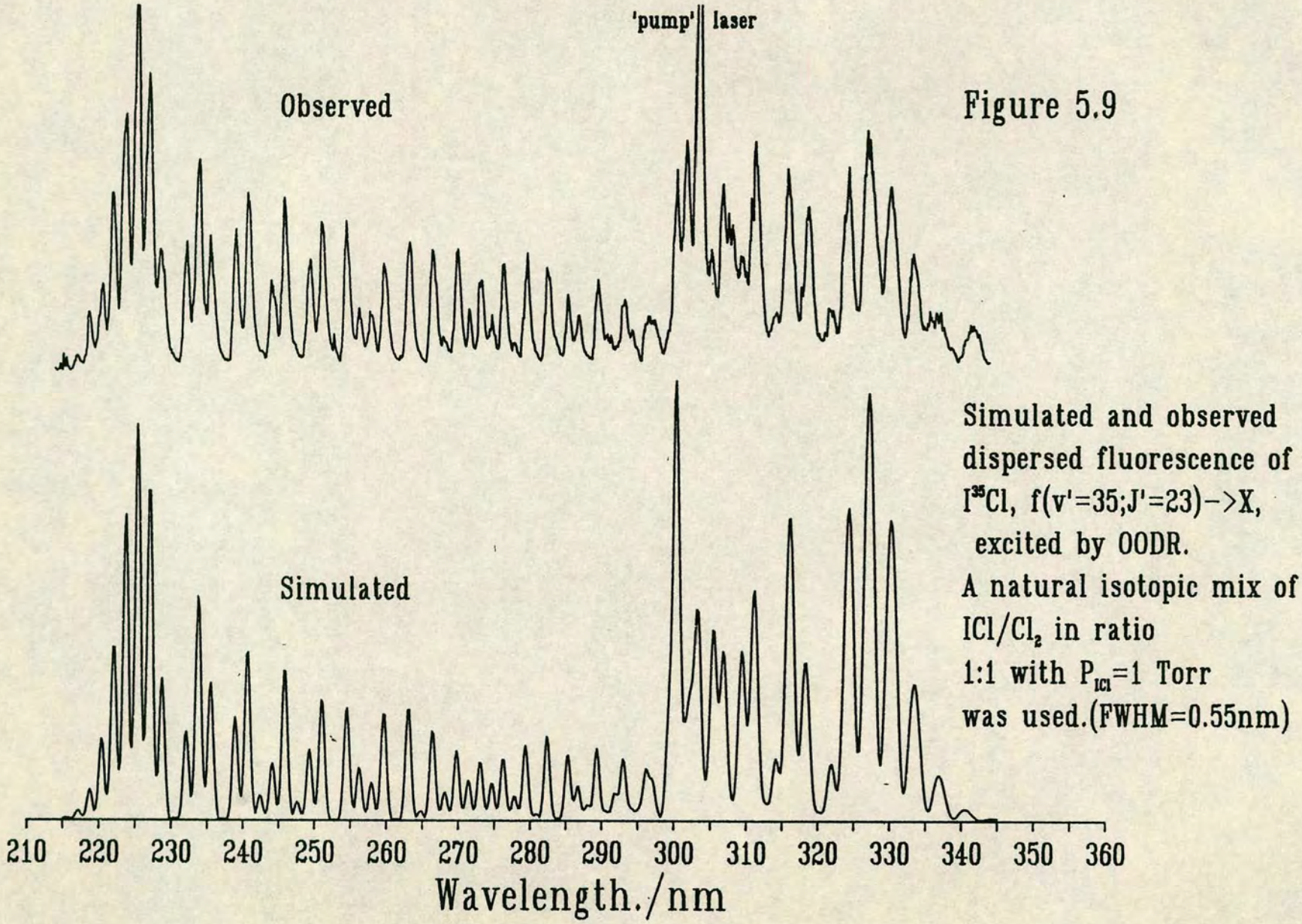


Figure 5.9

Simulated and observed dispersed fluorescence of $I^{35}Cl$, f(v'=35;J'=23)->X, excited by OODR. A natural isotopic mix of $ICl/Cl_2$ in ratio 1:1 with $P_{ICl}$=1 Torr was used.(FWHM=0.55nm)

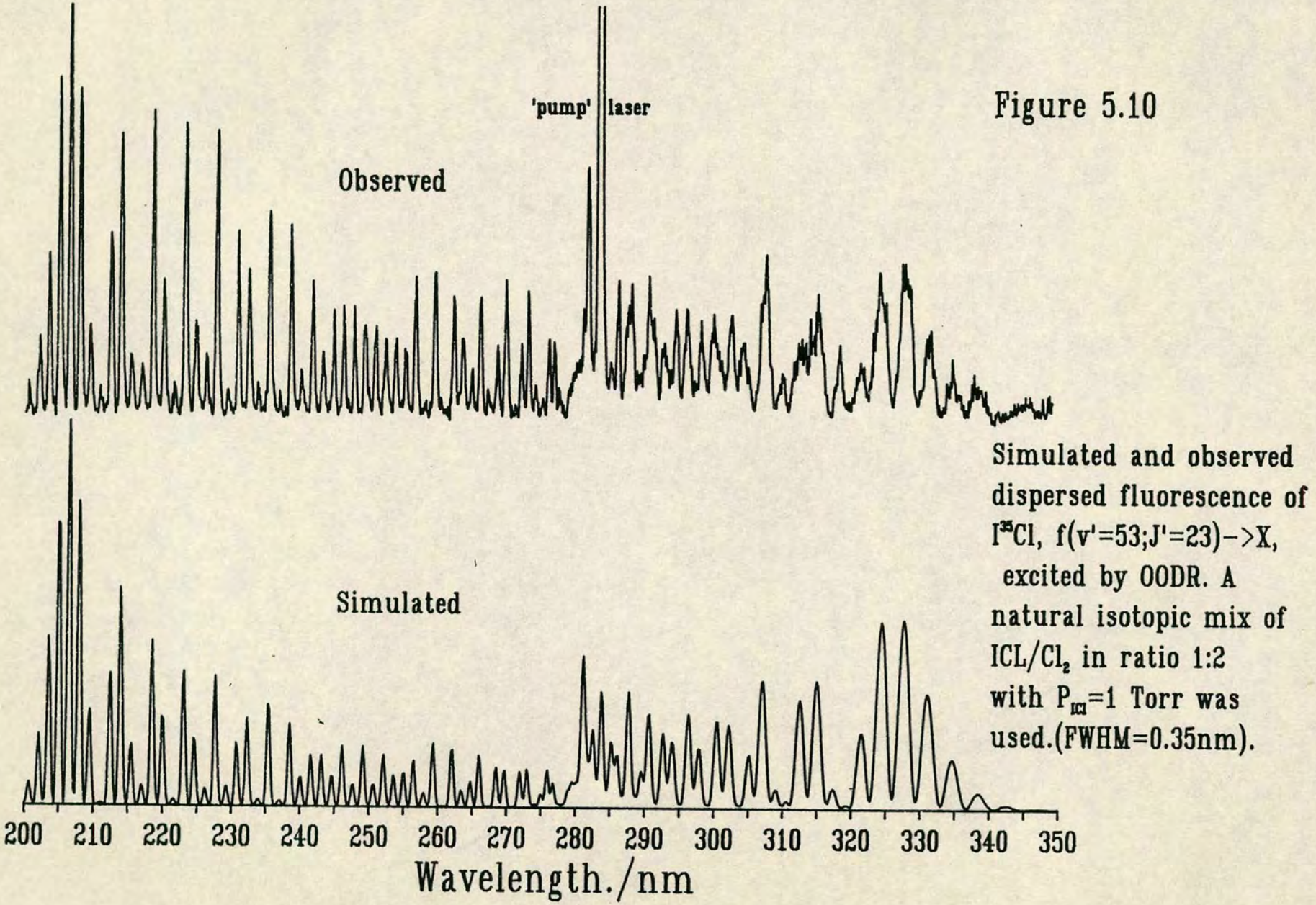


Figure 5.10

Simulated and observed dispersed fluorescence of $I^{35}Cl$, f(v'=53;J'=23)->X, excited by OODR. A natural isotopic mix of $ICL/Cl_2$ in ratio 1:2 with $P_{tot}$=1 Torr was used.(FWHM=0.35nm).

and E(v'=76;J'=23) respectively of $I^{35}Cl$. Similarly figures 5.9 and 5.10 show dispersed fluorescence from f(v'=35;J'=23) and f(v'=53;J'=23) respectively of $I^{35}Cl$. All spectra were recorded in their entirety, lying at sufficiently low v' levels that their blue origins, corresponding to bound-bound transitions to deep within the ground state, lie just above air cut-off.

The bound-free regions are of 'double frequency' type, indicating a maximum in the Mulliken difference potential. The rainbow position at roughly 410 nm, has remained unchanged from the synchrotron work. The bound-bound/bound-free boundary is marked by the characteristic step down of intensity from the red. To the blue of this the bound-bound regions reflect the upper state wavefunctions sampled by the bound levels of the ground state. Since the input energy is accurately known and a reliable RKR analysis of the ground state available [10], it was possible to identify the ground state vibrational levels responsible for each of the bound-bound resonances. It was established that the most intense peak in the first oscillation of the intensity envelope at the blue extremum corresponded to v" = 11,9,17 and 12 in figures 5.7-10 respectively. This represents transitions from internuclear separations very close to the maximum of the first oscillation of the upper state wavefunction. Subsequent oscillations in the bound-bound low frequency envelope also reflect the upper state wavefunction and thus provide a very sensitive probe of the position of the upper state inner wall (section 5.4).

Unfortunately , to date, no reliable combined instrument response curve is available. Figures 5.7-10 are uncorrected spectra, and great care must be taken when comparing relative intensities of widely spaced features.

Calibration was conveniently provided by the pump laser which always lay embedded within the ion-pair → X state system ,near the bound-bound/bound-free boundary ( n.b. B(v=1) lies at 17700 $cm^{-1}$, just above the dissociation energy of the ground state).

## 5.4 Detailed Analysis

### 5.4.1 The Observed Vibrational Spacings 159-177 nm.

We established in sections 5.3.1 and 5.3.2 that the state responsible for the narrow vibrational spacing in absorption and fluorescence excitation between 159 and 177 nm is most likely the $E(0^+)$ state (see tables 5.4-6 and figures 5.2 and 5.3). An RKR analysis based on the first 31 vibrational levels exists for the $E(0^+)$ state [1] covering turning points from 2.753 Å to 4.182 Å and up to 15% of De. $T_e$ is firmly located at 39059.5 $cm^{-1}$ . In order to reproduce any local vibrational spacings, or simulate dispersed fluorescence , an extensive upper state must be constructed to support the amplitude of the highest vibrational state accessed.

A divided differences table of the attractive limb of the RKR points reveals that the point of inflection has not yet been reached, we are therefore unable to use a modified Rittner analytical function immediately (equation 5.2) n.b. for an $I^+$ ion in the $^3P_{2,0}$ state the anion-quadrupole interaction energy should be positive.

$$V_E(R) = T_\infty - C6/r^6 - C4/R^4 + C3/R^3 - e^2/4\pi\varepsilon_0 R \quad : R>4.5\ \text{Å} \tag{5.2}$$

The extrapolation from 4.182 Å to beyond the point of inflection (~4.5Å) was based on a successful simulation of figures 5.5 and 5.8, the difference potential involved spanned roughly 2.6 Å to 5.2 Å (section 5.4.2). The coefficients C4, C6 and C3 were then adjusted so that equation 5.2 was continuous in value and gradient with the extrapolated potential, beyond the point of inflection. A satisfactory potential was obtained with C6 = 7.5 x $10^5$ $cm^{-1}Å^6$, C4 = 6.8 x $10^5$ $cm^{-1}Å^4$ and C3 = 3.13 x $10^4$ $cm^{-1}Å^3$. The value of C4 is roughly 45% greater than that suggested by equation 5.3.

$$C4 = e^2/4\pi\varepsilon_0 \cdot \tfrac{1}{2}(\alpha_- + \alpha_+) = 4.7144 \times 10^5 cm^{-1}Å^4 \tag{5.3}$$

$$C6 = 3/2.\alpha_+\alpha_-\omega_+\omega_-/(\omega_+ + \omega_-) = 6.0951 \times 10^5 Å^6 \tag{5.4}$$

Similarly C6 is roughly 13% greater than suggested by equation 5.4. We feel , as in sections 3.4.1 and 4.4, if these are indeed the asymptotic values of these coefficients i.e. there is no contribution from higher terms in the R range over which V(R) was fitted, that this reflects an underestimation of the anion polarisability of reference [28] on extrapolation to the gas phase. Care should

Table 5.4

E state ion-pair vibrational structure in synchrotron absorption (c.f. figure 5.2) ca. 160 nm

| pk index n | $\lambda$(obs)/nm | $\nu$(obs)/cm$^{-1}$ | $\Delta G_v$(obs)/cm$^{-1}$ |
|---|---|---|---|
| 5 | 159.89 | 62541 | |
| 4 | 159.96 | 62514 | 27 |
| 3 | 160.03 | 62488 | 26 |
| 2 | 160.10 | 62460 | 28 |
| 1 | 160.17 | 62432 | 28 |
| 0 | 160.25 | 62401 | 31 |

Table 5.5

E state ion-pair vibrational structure in synchrotron absorption (c.f. figure 5.2) ca. 162 nm

| pk index n | $\lambda$obs/nm | $\nu$obs/cm$^{-1}$ | $\Delta G_v$(obs)/cm$^{-1}$ |
|---|---|---|---|
| 22 | 161.87 | 61777 | |
| 21 | 161.95 | 61746 | 31 |
| 20 | 162.04 | 61712 | 34 |
| 19 | 162.11 | 61685 | 27 |
| - - - | - - - | - - - | - - - |
| 16 | 162.35 | 61594 | |
| 15 | 162.45 | 61556 | 38 |
| 14 | 162.53 | 61526 | 30 |
| 13 | 162.62 | 61492 | 34 |
| 12 | 162.70 | 61462 | 30 |
| 11 | 162.78 | 61431 | 31 |
| 10 | 162.86 | 61401 | 30 |
| 9 | 162.95 | 61367 | 34 |
| 8 | 163.03 | 61337 | 30 |
| 7 | 163.12 | 61303 | 34 |
| 6 | 163.21 | 61270 | 33 |
| 5 | 163.29 | 61240 | 30 |
| 4 | 163.34 | 61221 | 19 |
| 3 | 163.48 | 61168 | 53 |
| 2 | 163.58 | 61131 | 37 |
| 1 | 163.66 | 61101 | 30 |
| 0 | 163.76 | 61064 | 37 |

Table 5.6

E state ion-pair vibrational structure in synchrotron fluorescence excitation (c.f. figure 5.3) between 174.5 nm and 177 nm

| pk index n | $\lambda$obs/nm | $\nu$ obs/cm$^{-1}$ | $\Delta G_v$(obs)/cm$^{-1}$ |
|---|---|---|---|
| 14 | 174.49 | 57310 | |
| 13 | 174.64 | 57261 | 49 |
| 12 | 174.81 | 57205 | 56 |
| 11 | 174.99 | 57146 | 59 |
| 10 | 175.12 | 57104 | 42 |
| 9 | 175.31 | 57042 | 62 |
| 8 | 175.45 | 56996 | 46 |
| 7 | 175.63 | 56938 | 58 |
| 6 | 175.80 | 56883 | 55 |
| 5 | 175.99 | 56821 | 62 |
| 4 | 176.16 | 56767 | 54 |
| 3 | 176.31 | 56718 | 49 |
| 2 | 176.49 | 56660 | 58 |
| 1 | 176.44 | 56612 | 48 |
| 0 | 176.79 | 56564 | 48 |

be exercised however when discussing the physical significance of these values, in relation to the Coulomb term they are very small and consequently highly correlated. What is important is that their magnitudes and sign should be realistic so that the smallness of the contributions of the non-Coulomb terms at R > 4.5 Å means that the outer branch of the E state potential is constrained to roughly ±30 $cm^{-1}$ by the RKR points and the Coulomb limb.

The inner limb presents more of a problem. If it is constructed by fitting a functional form like equation 5.5 to the first two RKR points on the inner branch, the potential rises so steeply that the maximum in absorption from the ground state would be seen at roughly 155 nm.

$$V_E(R) = D_e + A + C10/R^{10} : R<2.753 \text{ Å} \qquad (5.5)$$

Furthermore, the vibrational spacing predicted by this potential is consistently too high compared with those observed. It is clear that the potential must be widened, but, within the constraints mentioned above, the outer branch cannot be lowered sufficiently to produce the observed spacing. Consequently we must relax the inner wall. To do this we adopted a more flexible spline potential rather than a functional form. Sixty-two knot points were provided by the RKR analysis and 10 points at R > 4.2 Å by the attractive limb as described above, a further 8 points described the inner wall. The inward shift of the inner wall needed to reproduce the local vibrational spacings resulted in a very soft repulsive limb; unlike $Br_2$ a point of inflection was not needed (figure 5.12 and table 5.7). This potential also suggests a maximum in absorption at roughly 160 nm, consistent with figure 5.1. We were unable to 'tune' the spacing at $G_v$ = 56557 $cm^{-1}$ exactly to 54 $cm^{-1}$ because this would have destroyed the fitting of the high frequency structure simulated in figure 5.5 (section 5.4.2), it is however well within experimental error.

Identification of the absolute vibrational quantum number , v', was based on assuming a Boltzmann distribution of initial rotational states in v" = 0 of the ground state. As discussed in section 2.3, the extended rotational contour of a typical halogen/interhalogen Rydberg to ion-pair vibrational transition at room temperature , will peak at roughly $J"_{max}/2.0$ (c.f. equation 2.13). This allowed an estimate of the rotational contributions to the peaks listed in tables 5.2-4. By comparing the observed term values with those calculated for J'=15 ($J"_{max}$=30), the vibrational quantum numbers listed in column 3 of table 5.7

Table 5.7

Comparison of observed and calculated average vibrational spacings for high in the E state of $I^{35}Cl$

| Ev/cm$^{-1}$ | $\overline{\Delta G_v(obs)}$ [a] | V'(calc.) [b] | $\overline{\Delta G_v(calc)}$/cm$^{-1}$ |
|---|---|---|---|
| 62402 | 28 | 316 | 27.6 |
| 61069 | 32 | 273 | 32.3 |
| 56557 | 54 | 171 | 55.2 |

a) +/- 3 cm$^{-1}$

b) ± 1 cm$^{-1}$

were calculated.

It may be the case that such 'soft' repulsive inner walls are characteristic of the ion-pair pair potentials and that our definition of normality based on equation 5.5 is unjustified. We are at present investigating an 'extended' RKR technique whereby the rovibrational constants are pushed beyond the range of levels actually observed in an attempt to assess what a normal ion-pair inner wall resembles. Under this new criteria the $E(0^+)$ state of ICl may appear normal and the $Br_2$ $D(0_u^+)$ state (below its point of inflection) may be anomalous. Alternatively, a homogeneous interaction with next highest $\Omega = 0$ ion-pair state, the $f(0^+)$, is not inconsistent with the bending away from the functional form of equation 5.5 described above. This behaviour has previously been observed for $I_2$ by Brand and Hoy [27]. Either way it appears that the $E(0^+)$ state intersects the $\Pi_{0+}$ component of the $b_6$ Rydberg state i.e. the potentials are best described in the diabatic approximation. This is consistent with Kerr's [21] interpretation of the fluorescence excitation and absorption spectra shown in figures 5.1-3 and briefly discussed in sections 5.3.1-2.

### 5.4.2 The Dispersed Fluorescence

The ground state has been analysed by Brand and Hoy [10], RKR turning points are given up to v"=73 and $G_v$ = 17504.84 $cm^{-1}$ (i.e. 97% of $D_e$) spanning 1.932 Å to 5.426 Å. The inner, repulsive wall, was extended by fitting an exponential, $Ae^{-bR}$, to the first two RKR points. The outer attractive limb was extended using the asymptotic expansion:

$$V_x(R) = D_e - C6/R^6 - C8/R^8 : R>5.4 \text{ Å} \qquad (5.6)$$

C6 and C8 were 1.06 x $10^6 cm^{-1}Å^6$ and 8.06 x $10^6 cm^{-1}Å^8$ respectively [29]. Since the E state RKR turning points extend from 2.753 Å to 4.182 Å, the region around the difference potential maximum, and hence the simulation of the rainbow regions of figures 5.5,5.7 and 5.8, are dependent solely on the relative phase of the upper and lower state wavefunctions (see figure 5.12). Assuming the inner wall of the ground state is unperturbed and the attractive limb of the E state is as described in the preceding section, our only adjustable in 'tuning' the simulated high frequency structure in the rainbow region is the position of the E state inner wall (see section 2.4.3). This movement has a cyclic effect on the high frequency structure with periodicity of approximately 0.3 Å, we choose the closest 'in-phase' inner limb consistent with the observed vibrational

spacing (section 5.4.1). This is why the calculated vibrational spacing around 176 nm ($G_v$=56557 $cm^{-1}$) is not exactly the same as the observed, although still well within experimental error (table 5.7).

Regarding the simulation shown in figure 5.5, the relatively large synchrotron excitation band width ($\Delta\lambda$=4.5 nm) was assumed to have a Gaussian profile and was combined with the fluorescence excitation profile around 176 nm. This gave a realistic description of the upper state vibrational population which effectively ranged from v'=163 to 180 with 173 as the most populated level. Both isotopic combinations, appropriately weighted, were also included and the final output slit convoluted with the estimated resolution of the fluorescence monochromator (FWHM=1.5 nm). Comparison of the observed and simulated spectra is very favourable, although there appears to be some filling in of the coarse, low frequency structure. This may be because of an under estimation of the resolution in excitation or dispersion, although the high frequency peak-to-valley ratio has been successfully reproduced , making this explanation unlikely. Alternatively, it may be due to weaker underlying systems either running in from the red or from the f($0^+$) state. Population of the f state may be by a vibronic coupling or the simultaneous excitation of both the E and f states. Asymmetry in $\mu_{12}(R)$ is not responsible (see below). The range of R probed by the simulation of figure 5.5 was 2.9 to 4.7 Å.

The spectra in figures 5.7 and 5.8, corresponding to fluorescence from E(v'=53;J'=23) and E(v'=76;J'=23) respectively, show transitions from a wider range of internuclear separations e.g. 2.58 to 5.15 Å in figure 5.8. As the ground state of ICl is still well characterised throughout this range [10], simulation of these spectra yielded further reliable information about the E state. Successful fitting of the bound-free structure allowed the attractive limb of the E state to be extrapolated well beyond its point of inflection and parameterised accurately by equation 5.2 (see section 5.4.1). Similarly, reproducing the intensity envelope of the bound-bound resonances at the blue origin accurately fixes the inner turning point of the upper state wave function, we estimate to within ± 0.005 Å.

An RKR analysis of the f state was performed using the constants of Brand and Hoy [2]. The calculated turning points are included in table 5.9, they range up to v' = 14 and $G_{v'}$ = 2522.6 $cm^{-1}$ spanning 2.892 to 3.815 Å. $T_e$ is firmly

located at 44923.8 $cm^{-1}$ . In a similar fashion to figure 5.7 and 5.8 for the E state, figure 5.9 and 5.10, corresponding to fluorescence from f(v'=35;J'=23) and f(v'=53;J'=23) respectively, were simulated. This allowed the RKR turning points to be reliably extended up the inner wall. However, v'=53 is still relatively low and did not allow the outer limb to be extended much beyond its point of inflection ; thus no reliable Rittner parameterisation was possible.

All the observed fluorescence spectra show a marked fall off in intensity to the blue of the rainbow. this could only be accounted for by the transition moment function, $\mu_{12}(R)$, being broadly peaked just to the large R side of the minimum of the E or f states i.e. around 3.4 Å. The observed decay envelope could only be reproduced if both interfering branches of the difference potential are attenuated; a step or tanh like function was not sufficient. A simple Gaussian (equation 5.7) successfully reproduced the ratio of the first few peak intensities around the rainbow of figure 5.5.

$$\mu_{12}(R) = A.\exp(-3/2(R - 3.4)^2) : 2.9<R<4.7\ Å \qquad (5.7)$$

The more extensive spectra of figures 5.7–10 needed a more flexible approach. The transition moments were described by 21 equally spaced knot points spanning the the probed range of R (see figure 5.11). The optimum functions still peaked around R = 3.4 Å and as expected on theoretical grounds, decay monotonically to large R. They are however no longer symmetrical, sharply falling off at small R, this was necessary to attenuate the strong bound–bound resonances originating near the inner turning point of the upper state wave function. However this asymmetry was not sufficient to account for the filling–in of the low frequency minima exhibited in figure 5.5, (see above).

A close comparison of the observed and simulated spectra of figures 5.7–10 reveals that the intensity distributions are not exactly reproduced. Since no instrument response curve was available, these spectra remain uncorrected, and only the simulation of the broad intensity features was attempted. An exact match , and an accurate transition dipole function, awaits further experimental work, and carries a high priority. Despite this, the synchrotron dispersed fluorescence response curve was known to be flat to within 10%, (section 5.2.1), thus $\mu_{12}(R)$ over the range of R spanned by the v'=173 fluorescence (i.e. 2.9–4.7 Å) must be reliable. Essentially the same $\mu_{12}(R)$ functions, except with the wings extended, were used for the OODR dispersed

Figure 5.11

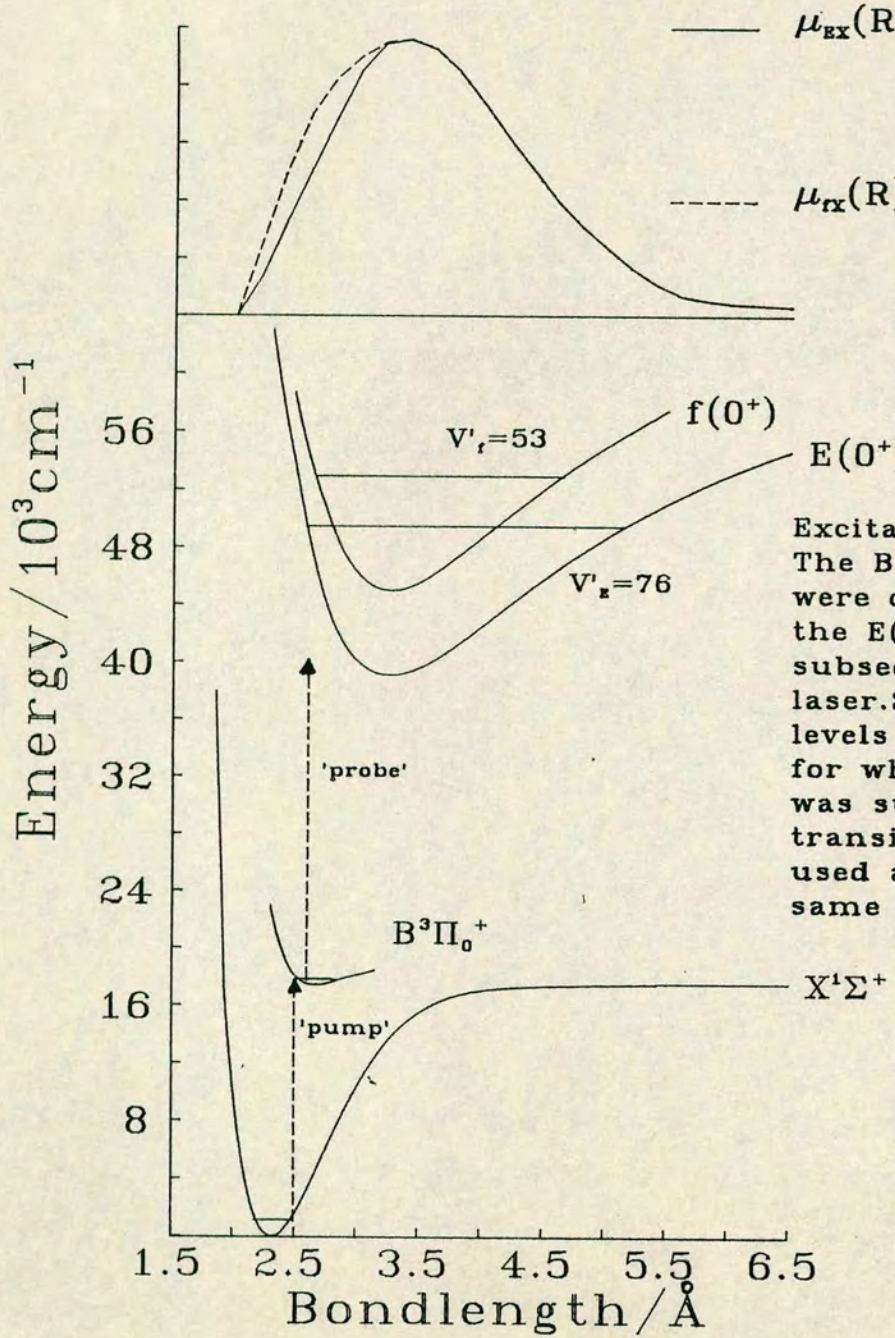


Excitation scheme for the OODR work. The B(v'=1;J'=24&32) levels of $I^{35}Cl$ were coincidently pumped, and the $E(0^+)$ & $f(0^+)$ states subsequently scanned by the probe laser. Shown are the two highest levels in each ion-pair state for which dispersed fluorescence was succesfully analysed; the transition moment functions used are also shown on the same scale above.

fluorescence spectra, and the bound-free portions were reproduced satisfactorily, without any detector response correction. This shows that the detector response of the OODR experiment was pretty flat in the relevant spectral region, although presumably falling off slightly in the wings ( the dispersion grating was blazed at roughly 300 nm).

### 5.4.3 Absolute Term Values

In addition to the average vibrational spacings observed with the synchrotron radiation, more accurate absolute rovibrational term values were obtained using the OODR techniques described in section 5.2.2 (tables 5.2 and 5.3). These observations were made after the synchrotron work and in the last month of writing this thesis, consequently we present their analysis after section 5.4.1. The potentials as described in the preceding two sections, predicted the positions of these observations to within 5 $cm^{-1}$, but this was outwith the experimental error (± 0.8 $cm^{-1}$). In order to reproduce these absolute term values and yet remain consistent with all the work described above, in particular the simulation of figures 5.7-10, we had to adjust the knot points of the attractive limbs of both states. The changes required were typically ±20 $cm^{-1}$ , and in the E state could easily be accounted for by minor adjustments of the non-Coulomb terms of equation 5.2. Indeed , it is reassuring that equation 5.2 predicted the attractive limb so accurately considering the fashion in which the highly correlated C3, C4 and C6 parameters were derived.

Tables 5.2 and 5.3 list the observed and calculated term values of both E and f states for the dominant isotopic combination $I^{35}Cl$. The calculated values were based on the 'pseudo' turning points listed in tables 5.8 and 5.9. The polynomial fitting of the synchrotron vibrational spacings also contributes to table 5.8 for the E state (v'>171). We thus establish that the absolute numbering of the levels accessed by the synchrotron work belongs to the same progression as those from the OODR work.

Table 5.8

Pseudo-RKR points for the $E(0^+)$ state of $I^{35}Cl$

| $v^{a)}$ | $G_v/cm^{-1}$ | $R_{min}/\AA$ | $R_{max}/\AA$ |
|---|---|---|---|
| 40 | 6088.2 | 2.702 | 4.396 |
| 50 | 7379.0 | 2.662 | 4.604 |
| 60 | 8589.1 | 2.629 | 4.812 |
| 70 | 9722.6 | 2.600 | 5.021 |
| 80 | 10781.4 | 2.574 | 5.234 |
| 90 | 11769.7 | 2.550 | 5.450 |
| 100 | 12698.6 | 2.527 | 5.665 |
| 110 | 13568.7 | 2.507 | 5.888 |
| 120 | 14380.9 | 2.489 | 6.120 |
| 130 | 15139.3 | 2.473 | 6.359 |
| 140 | 15849.4 | 2.459 | 6.602 |
| 150 | 16517.0 | 2.445 | 6.848 |
| 160 | 17145.9 | 2.433 | 7.098 |
| 170 | 17739.2 | 2.421 | 7.351 |
| 180 | 18299.4 | 2.410 | 7.609 |
| 190 | 18829.0 | 2.399 | 7.872 |
| 200 | 19330.3 | 2.389 | 8.139 |
| 210 | 19805.2 | 2.379 | 8.410 |
| 220 | 20255.8 | 2.370 | 8.685 |
| 230 | 20683.7 | 2.362 | 8.965 |
| 240 | 21090.6 | 2.354 | 9.249 |
| 250 | 21477.8 | 2.346 | 9.537 |
| 260 | 21846.8 | 2.339 | 9.829 |
| 270 | 22198.7 | 2.332 | 10.125 |
| 280 | 22534.7 | 2.326 | 10.426 |
| 290 | 22855.6 | 2.320 | 10.731 |
| 300 | 23162.5 | 2.314 | 11.040 |
| 310 | 23456.0 | 2.309 | 11.354 |
| 320 | 23737.1 | 2.305 | 11.672 |

a) RKR analysis of Brand et al. [1] stops at v = 31

Table 5.9

Pseudo-RKR points for the f (0+) state of $I^{35}Cl$

| $v^{a)}$ | $G_v/cm^{-1}$ | $R_{min}/Å$ | $R_{max}/Å$ |
|---|---|---|---|
| 0 | 92.0 | 3.183 | 3.347 |
| 1 | 274.9 | 3.129 | 3.413 |
| 2 | 456.2 | 3.093 | 3.461 |
| 3 | 636.1 | 3.065 | 3.502 |
| 4 | 814.5 | 3.040 | 3.538 |
| 5 | 991.5 | 3.020 | 3.572 |
| 6 | 1167.0 | 3.001 | 3.605 |
| 7 | 1341.2 | 2.984 | 3.634 |
| 8 | 1513.9 | 2.969 | 3.663 |
| 9 | 1685.4 | 2.954 | 3.690 |
| 10 | 1855.4 | 2.940 | 3.717 |
| 11 | 2024.2 | 2.927 | 3.743 |
| 12 | 2191.7 | 2.915 | 3.768 |
| 13 | 2357.9 | 2.904 | 3.792 |
| 14 | 2522.9 | 2.893 | 3.817 |
| 15 | 2686.7 | 2.882 | 3.841 |
| 20 | 3487.1 | 2.839 | 3.958 |
| 25 | 4257.4 | 2.803 | 4.071 |
| 30 | 4998.0 | 2.770 | 4.180 |
| 35 | 5711.0 | 2.741 | 4.286 |
| 40 | 6398.3 | 2.713 | 4.388 |
| 45 | 7061.6 | 2.687 | 4.490 |
| 50 | 7701.9 | 2.662 | 4.590 |
| 55 | 8319.7 | 2.640 | 4.691 |
| 60 | 8914.8 | 2.619 | 4.794 |
| 65 | 9487.7 | 2.600 | 4.898 |

a) RKR analysis based on constants of Brand and Hoy [3] stops at v = 14

Figure 5.12

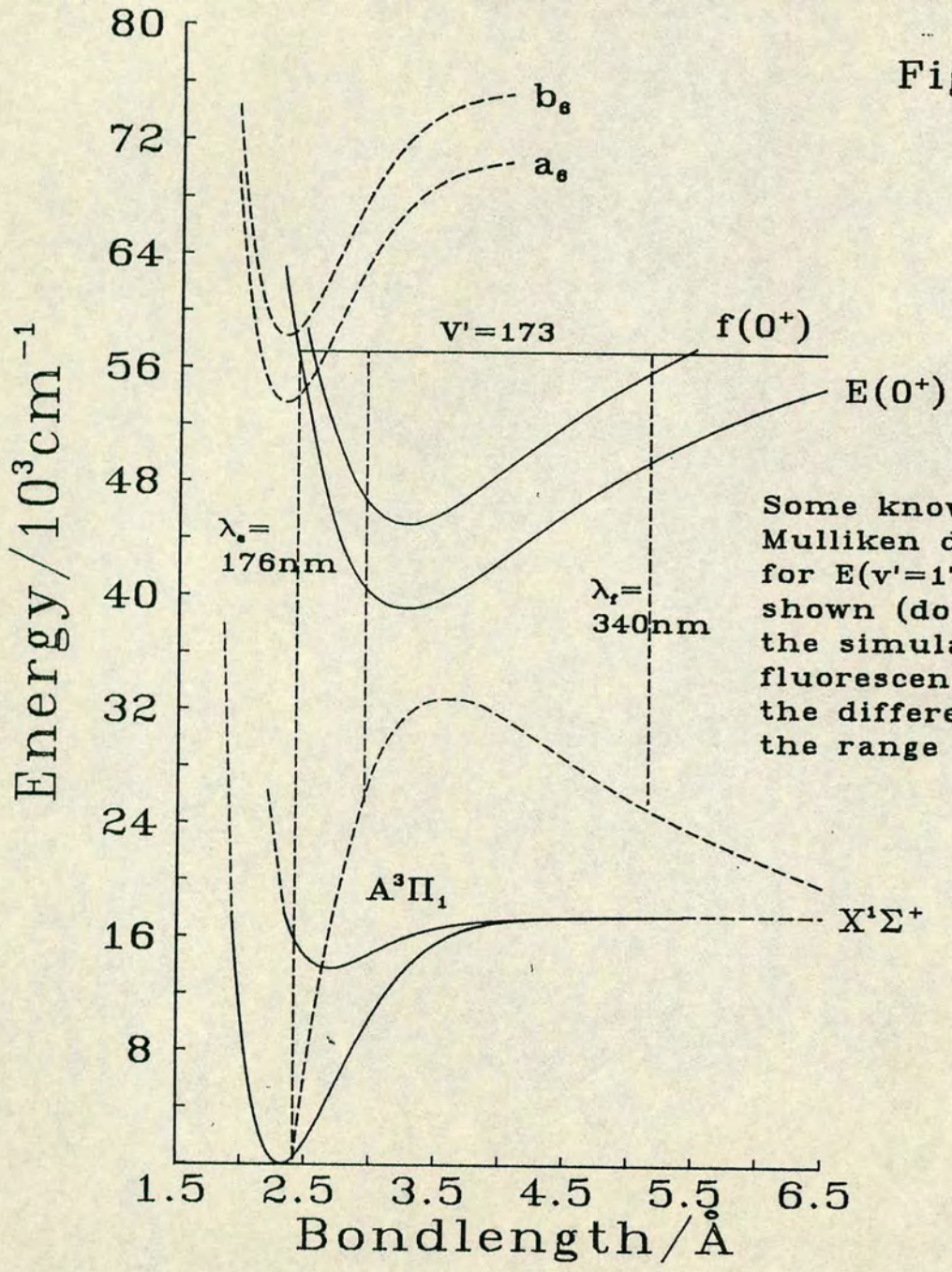


Some known states of ICl. The Mulliken difference potential for E(v'=173) -> X is also shown (dotted). The extent of the simulated dispersed fluorescence (fig.5.5) fixes the difference potential over the range indicated.

## 5.5 Discussion

The $E(0^+)$ ion-pair state is identified as the state responsible for the quasi-continuous absorption underlying the sharp Rydberg resonances between 157.5 and 190nm. Absorption across this range results in fluorescence between 410 and 300 nm . The lower state involved is identified as the ground state. The same fluorescence system was also observed from lower rovibrational levels, E(v'=53&76;J'=23), following a two photon excitation via the $B^3\Pi_{0+}$(v=1;J=24) intermediate state. We present for the first time , the dispersed and simulated fluorescence spectra in their entirety i.e. from the rainbow at 410 nm to the bound-bound resonances at roughly 220 nm. The information contained in these 'McLennan' type systems fixes the difference potential between 2.6 and 5.2 Å, corresponding to known regions of the ground state and unknown of the E state. Fitting of the bound-bound structure proved particularly sensitive to the position of the upper state inner wall, fixing the wavefunction inner turning point to within ±0.005 Å up to $T_e(E)$ + 10400 $cm^{-1}$.

Similar complete dispersed fluorescence spectra were also observed from f(v'=53;J'=23) and f(v'=35;J'=23), $f(0^+)$ being the next highest ion-pair pair state with $\Omega$ = 0. Successful simulation of these spectra located the difference potential between 2.6 and 4.6 Å. Again the accurate fitting of the bound-bound blue origin gave a reliable inner wall , ±0.005 Å, for the f state up to $T_e(f)$ + 8000 $cm^{-1}$ . Outer extrapolation of the E state RKR turning points [1], was initially characterised by the Rittner coefficients C1, C3 and C6, and found to be surprisingly accurate (see below). The f state ,on the other hand was not probed far enough beyond its point of inflection on the attractive limb and thus no Rittner parameterisation was attempted.

In addition to dispersed fluorescence, the OODR experiment yielded accurate (± 0.8 $cm^{-1}$) rovibrational term values between v'=47 and v'=98 for the E state and v'=6 and v'=66 for the f state. The proposed potentials , tables 5.8 and 5.9, account for these observations well within experimental error. In the case of the E state this potential deviated only slightly (± 20 $cm^{-1}$) from the Rittner parameterisation used in the dispersed fluorescence simulations , lending confidence to this approach in areas where accurate term values are not available e.g. chapters 3 and 4.

Partially resolved vibrational structure of the E state was observed with

synchrotron radiation, and was established as part of the same vibrational progression observed in OODR, but with $171 < v' < 316$.

The final E state potential had a rather 'soft', under present criteria, inner wall, although it remained monotonic in first and second derivatives. Further work is under way to define a typical ion pair inner wall, it may be that the E state as described above is 'normal' and our previous standard, equation 5.5, is too hard. No point of inflection, as in $Br_2$, or double minima, as in $Cl_2$ , was required in the range $T_e(E)+4700\ cm^{-1}$ (last of the RKR turning points) to $T_e(E)+23850\ cm^{-1}$ (last of the synchrotron data). This is despite a Rydberg state of appropriate symmetry, the $\Pi_{0+}$ component of the $b_6$ series [8] , almost certainly intersecting the ion-pair inner wall within this range. We conclude that the potential of the E state is best represented in the diabatic approximation. This is in accord with Kerr's [21] discussions of the synchrotron absorption and fluorescence excitation.

A rather broadly peaked asymmetric transition moment function was needed to reproduce the profile of the dispersed fluorescence of both states. This has proved to be a common feature of fluorescence from high vibronic states where the configuration (or valence bond character) can change rapidly, especially near regions of strong coupling. The synchrotron fluorescence excitation spectrum has abundant evidence of this strong coupling between most of the Rydberg states and near resonant ion-pair vibrational levels of appropriate symmetry. The non-resonant ion-pair levels fluoresce strongly, and it is these relatively unperturbed regions of the molecule that we were concerned with in this chapter.

## References


1. D. Bussieres and A.R. Hoy, Canad. J. Phys., 62, 1941 (1984)
2. J.C.D. Brand, V.D. Deshpande, A.R. Hoy and S.M. Jaywant, J. Mol. Spectrosc., 100, 416 (1983)
3. J.C.D. Brand, A.R. Hoy and S.M. Jaywant, J. Mol. Spectrosc., 106, 388 (1984)
4. J.C.D. Brand, U.D. Deshpande, A.R. Hoy and E.J. Woods, Canad. J. Chem., 61, 846 (1983)
5. K.P. Lawley, D. Austin, J.B Tellinghuisen and R.J. Donovan, Mol. Phys., accepted for publication (1987)
6. M.A. MacDonald, R.J. Donovan and M.C. Gower, Chem. Phys. Lttrs., 97, 72 (1983)
7. J.B. Tellinghuisen, Canad. J. Phys., 62, 1933 (1984)
8. P. Venkateswarlu, Canad. J. Phys., 53, 812 (1975)
9. N.K. Bibinov and I.P. Vinogradov, Opt. Spektrosk., 59, 317 (1985)
10. J.C.D. Brand and A.R. Hoy, J. Mol. Spectrosc., 114, 197 (1985)
11. E. Kerr, M.A. MacDonald, R.J. Donovan and J.P.T. Wilkinson, J. Photochem., 31, 145 (1985)
12. M.A. MacDonald, Ph.D. Thesis, Edinburgh University, pp 37–40 (1984)
13. R.J. Donovan, B.V. O'Grady, K. Shobatake and A. Hiraya, Chem. Phys. Lttrs., 122, 612 (1985)
14. P. Venkateswarlu, Canad. J. Phys., 47, 2525 (1969)
15. M.I.T. Wavelength Tables, Wiley & Sons Inc., New York
16. L.C. Lee, M. Suto, and K.Y.Yang, J. Chem. Phys., 84, 5277 (1986)
17. B.K. Clark and I.M. Littlewood, Chem. Phys., 107, 97 (1986)
18. R.S Mulliken, Phys. Rev., 46, 549 (1934)
19. E.A Kerr, A.Yencha, A. Hopkirk and D. Shaw, unpublished data.
20. R.J. Donovan and N. Nishi, Chem. Phys. Lttrs., 117, 286 (1985)
21. E. Kerr, Ph.D. Thesis, Edinburgh University, to be submitted.
22. M. Martin, C. Fotakis, R.J. Donovan and M.J. Shaw, Nuovo Cimento, 63B, 300 (1981)
23. K.P. Lawley, M.A. MacDonald and R.J. Donovan, Chem. Phys. Lttrs., 92, 322 (1982)
24. M.J. Mulliken, J. Chem. Phys., 55, 288 (1971)
25. J.B. Tellinghuisen, Chem. Phys. Lttrs., 29 , 359 (1974)
26. S.G. Hansen, J.D. Thompson, R.A. Kennedy and B.J. Howard, J. Chem. Soc. Faraday Trans. II, 78, 1293 (1982)
27. J.C.D Brand and A.R. Hoy, Chem. Phys., 109, 109 (1986)
28. J.N. Wilson and R.M. Curtis, J. Phys. Chem., 74, 187 (1970)
29. M. Saute, B. Bussery, M. Aubert-Frecon, Mol. Phys., 51, 1459 (1986)
30. J.A. Coxon, R.M. Gordon and M.A. Wickramaaratchi, J. Mol. Spectrosc., 79, 363 (1980); J.A. Coxon and M.A. Wickramaaratchi, J. Mol. Spectrosc., 79, 380 (1980)
31. J.C.D. Brand, D. Brussieres and A.R. Hoy, J. Mol. Spectrosc., 113, 388 (1985)

# APPENDIX A
# NUMEROV-COOLEY IMP SUBROUTINE

The Numerov-Cooley method fo calculating unbound wavefunctions of the radial Schrödinger equation was discussed in section 2.1. Below is the appropriate IMP subroutine from the simulation programme, equations 2.4 and 2.6 are easily identified ( the latter pertains to normalisation of the unbound wavefunctions).

```
        %routine VECTORFR(%long %real %array %name VD,Y,%c
        %long %real %name E,AMPL, %integer %name N,LIM,TURN)
        %integer K0,K1,K2,K3,K4,K5
        %long %real EPS,F0,F1,F2
         %for K0 = 1,1,N %cycle
              Y(K0) = 0.0
         %repeat
         %for K1 = 2,1,N %cycle
          %if VD(K1+1)-E-2.0<=0.002 %c
          %and VD(K1)-E-2.0>=0.002 %then ->L10
         %repeat
L10:    Y(K1)=0.0
        Y(K1+1)=0.0
        Y(K1+2)=1.0@-04
         %for K3 = K1+3,1,LIM %cycle
              F0 = VD(K3)-E-2.0
              F1 = VD(K3-1)-E-2.0
              F2 = VD(K3-2)-E-2.0
              Y(K3) = (2*Y(K3-1)-Y(K3-2)+(F2*Y(K3-2)+%c
              10.0*F1*Y(K3-1))/12.0)/(1-F0/12.0)
         %repeat
         %for K5 = LIM+1,1,N %cycle
              F0 = VD(K5)-E-2.0
              F1 = VD(K5-1)-E-2.0
              F2 = VD(K5-2)-E-2.0
              Y(K5) = (2*Y(K5-1)-Y(K5-2)+(F2*Y(K5-2)+%c
              10.0*F1*Y(K5-1))/12.0)/(1-F0/12.0)
               %if Y(K5-2)**2<Y(K5-1)**2 %and%c
               Y(K5)**2<Y(K5-1)**2 %and %c
               K5>TURN+1500 %then ->L20
         %repeat
L20:      AMPL = Y(K5-1)*(MOD((E-VD(K5-1)+2.0)%c
           /(E-VD(N)+2.0)))**0.25
       %end
!
!
!
   %end
%end %of %program
```

# APPENDIX B
# FIGURE REPRODUCTION

For the benefit of those wishing to extend, or become involved further, with the work presented in this thesis, all the appropriate programmes,input, output and data files have been ARCHIVED on the ERCC main frame EMAS-C under the userid:EDCH05, the process password is available from Dr K.P. Lawley of the University of Edinburgh. Three 'groups', BR2., IBR. and ICL. contain all the coding relevant to each molecule. Within each group there are four types of files:

1. AACAT contains a catalogue of all the group members required to create a particular plot number (see below). An AACAT exists for all three groups and is the first member identified when the group is ANALYSED.
2. PLOTxyz are the EASYGRAPH graphic menus (see ERCC advisory) required to reproduce the figures as presented in this thesis. xyz is a three digit identity 'plot number' (see below).
3. molxyz indicates the group (mol) and the plot number (xyz) of the RCO plot file which when listed on a plotting device produces the thesis figures. The code linking the thesis figures to these plot numbers is given below.
4. General files containing data,input,output and non-specific programmes.

Thus to create figure 5.1, we must follow four steps:

- Consult the code list (below) to find relevant plotnumber i.e. fig. 5.1 corresponds to ICL001.
- Look in ICL.AACAT under ICL001 to identify all the appropriate type 4 files.
- ICL.PLOT001 is the EASYGRAPH menu which may be edited as desired.
- ICL.ICL001 is the RCO graphics file ready to list on a plotting device.

In this way, with a little experience, hopefully all the analysis in this thesis will be made accessible and extended as more experimental work is performed.

All the main programmes for simulation etc. can be found in an additional archived group SIMULATES. on the same process.

Figure codes

| | |
|---|---|
| 3.1 | BR2002 |
| 3.2 | BR2003 |
| 3.3 | BR2004 |
| 3.4 | BR2005 |
| 3.5 | BR2015 |
| 3.6 | BR2016 |
| 3.7 | BR2017 |
| 3.8 | BR2006 |
| 3.9 | ------ |
| 3.10 | BR2009 |
| 3.11 | BR2012 |
| 3.12 | BR2011 |
| 3.13 | BR2010 |
| 3.14 | BR2007 |
| 3.15 | BR2008 |
| 3.16 | BR2014 |
| 3.17 | BR2013 |
| 3.18 | ----- |
| | |
| 4.1 | IBR005 |
| 4.2 | IBR006 |
| 4.3 | IBR012 |
| 4.4 | IBR016 |
| 4.5 | IBR009 |
| 4.6 | IBR010 |
| 4.7 | IBR011 |
| 4.8 | IBR013 |
| | |
| 5.1 | ICL001 |
| 5.2 | ICL002 |
| 5.3 | ICL003 |
| 5.4 | ICL013 |
| 5.5 | ICL006 |
| 5.6 | ICL012 |
| 5.7 | ICL005 |
| 5.8 | ICL008 |
| 5.9 | ICL011 |
| 5.10 | ICL010 |
| 5.11 | ICL014 |
| 5.12 | ICL007 |

# APPENDIX C
# LECTURES ATTENDED

In accordance with the regulations of the University of Edinburgh, the Department of Chemistry, the following lectures and lecture courses were attended during the past three years:

- Emas Users Course
- Non-Linear Least Mean Squares Methods
- R.K.R Theory
- Signal Processing
- Numerical Methods
- Quantum Chemistry
- Molecular Electronics
- Scottish Quantum Chemistry Group Meetings

  * Edinburgh University (1984)
  * Dundee University (1985)
  * Strathclyde University (1986)
  * Edinburgh University (1987)

In addition all the regular departmental seminars and research group meetings were attended.

Conferences Attended

XIIth International Symposium on Molecular Beams, 13-17th July (1987).

Publications

'VUV Absorption and Fluorescence Excitation Spectra of $Br_2$', D.I. Austin, R.J. Donovan, A. Hopkirk, K.P. Lawley, D. Shaw and A. Yencha, Chemical Physics 118 91, (1987)